Coversheet for "Likely weakening of the Florida Current during the past century revealed by sea-level observations"

Christopher G. Piecuch[1,†]

[1]*Department of Physical Oceanography, Woods Hole Oceanographic Institution, Woods Hole, Massachusetts, USA*

This paper is a non-peer reviewed preprint submitted to Earth and Space Science Open Archive (ESSOAr). The paper has been resubmitted and under review a second round of reviews at Nature Communications.

† cpiecuch@whoi.edu

Likely weakening of the Florida Current during the past century revealed by sea-level observations

Christopher G. Piecuch[1]

[1] *Woods Hole Oceanographic Institution, Woods Hole, Massachusetts, USA*

The Florida Current marks the beginning of the Gulf Stream at Florida Straits, and plays an important role in climate. Nearly continuous measurements of Florida Current transport are available at 27°N since 1982. These data are too short for assessing possible multidecadal or centennial trends. Here I reconstruct Florida Current transport during 1909–2018 using probabilistic methods and principles of ocean physics applied to the available transport data and longer coastal sea-level records. Florida Current transport likely declined steadily during the past century. Transport since 1982 has likely been weaker on average than during 1909–1981. The weakest decadal-mean transport in the last 110 y likely took place in the past two decades. Results corroborate hypotheses that the deep branch of the overturning circulation declined over the recent past, and support relationships observed in climate models between the overturning and surface western boundary current transports at multidecadal and longer timescales.

Swiftly flowing north through the narrow, shallow Florida Straits, the Florida Current marks the headwaters of the Gulf Stream[1–4] (Figure 1). Together with the weaker Antilles Current[5–8], the Florida Current forms the major western boundary current in the subtropical North Atlantic Ocean at 27°N, providing closure to the wind-driven interior gyre circulation[9–11], and acting as a vital

limb of the Atlantic meridional overturning circulation[12]. Due to its transport of heat and other tracers, the Florida Current plays an important role in climate[13–15].

The integrated volume transport of the Florida Current, hereafter Florida Current transport, has been monitored nearly continuously at 27°N since 1982 through abandoned submarine telephone cables between West Palm Beach and Grand Bahama Island[1–4] (Figure 1). Before then, observations were made occasionally as part of short hydrographic cruises or brief field campaigns, each measuring a different component of the current at a distinct location. Earlier observations[16,17] only measured near-surface transports, missing any transports at depth. Later full-depth transport measurements[18–22] were made variously between Florida and Havana, Cay Sal Bank, the Cat Cays, or Bimini, which captured the flow through Yucatán Channel, but omitted transports through Nicholas, Santaren, or Northwest Providence Channels, all of which contribute to the transport at 27°N (Figure 1). Such disparities make it difficult to produce a stable instrumental estimate of Florida Current transport through time. Without such a coherent, longterm estimate, it has been unclear whether the Florida Current has undergone multidecadal- or longer-timescale change. Meinen et al.[3] concluded that the extant data, "provide no evidence for a longterm trend in the Florida Current transport," during 1964–2009. However, it remains unclear whether a trend would emerge in a longer, more complete transport history.

Questions of possible longterm changes in the Florida Current bear on hypotheses that the Atlantic meridional overturning circulation has weakened or is weakening. Proxy indicators, including surface and subsurface ocean temperatures at subpolar latitudes and sortable silts from

sediment cores off Cape Hatteras, suggest that the deep return flow of the meridional overturning circulation weakened either continuously during the twentieth century or earlier near the end of the Little Ice Age[23–27]. However, the proxies and their relation to the overturning are uncertain, so it is unclear how robust these suggestions are. Climate models simulate that weakening of the deep branch of the overturning circulation on multidecadal and longer timescales is balanced, in the sense of mass conservation, by weakening of the surface western boundary current[28–31]. Indeed, in paleoceanographic studies, changes in Florida Current transport have often been interpreted in terms of changes in the deep branch of the overturning circulation on centennial and millennial timescales[32]. Thus, a determination of whether the Florida Current transport changed during the past century, and by how much, based on instrumental observations would serve as a test of model simulations and proxy-based hypotheses regarding the deep branch of the overturning circulation, as well as inform paleoceanographic studies.

Previous authors argued that sea level from coastal tide gauges is informative of changes in Florida Current transport[17,18,33–37]. These arguments are based on geostrophic balance: at periods $\gtrsim 1$ day, the northward flow through Florida Straits imparts an eastward acceleration due to the Coriolis force that is counteracted by a pressure gradient across the Florida Straits, which manifests as a sea-level difference that can be observed by tide gauges on opposite sides of the Florida Current. However, circulation inferences based on tide gauges need to be made cautiously. Tide gauges measure the distance between the sea surface and Earth's crust at the coast. They capture not only the large-scale geostrophic circulation, but can also be impacted by remotely driven coastal-trapped waves and currents; local forcing and frictional dynamics over the conti-

nental shelf; changes in the gravity field, rotation vector, and viscoelastic deformation of the solid Earth; and other isostatic geophysical and oceanographic processes[38–40]. Tide-gauge data are also heterogeneously distributed in space and time. Long, continuous records are available at some southeastern USA and Caribbean sites far afield of the submarine cable at 27°N, but extant tide-gauge records close to the cable's endpoints near West Palm Beach and Grand Bahama are short, incomplete, and largely not overlapping[41] (Supplementary Figures 1, 2).

To overcome these challenges, I use Bayesian data analysis[42–44] to estimate annual Florida Current transport at 27°N during the past 110 y (see Methods). The estimate uses 1,390 y of annual coastal sea level from 46 tide gauges[41] along the southeastern USA and Caribbean during 1909–2018 and 36 y of annual Florida Current transports from cable measurements[1–4] over 1982–2018 (Figures 1, 2; Supplementary Figures 1, 2). Sea level is represented as a process with spatial correlation and temporal memory. The Florida Current transport is related to the difference in sea level across Florida Straits through geostrophy, but account is taken of non-oceanographic and ageostrophic effects on sea level and transport. The data are modeled as corrupt, imperfect versions of the processes. Bayes' rule is used to invert the model equations, and solutions are generated using numerical methods. The model equations are coupled, so that information is shared across space, time, and processes, which allows data gaps to be filled and unobserved processes to be estimated. The solution is fully probabilistic, and comprises thousands of ensemble members, each an equally likely history of transport that is consistent with the data and model equations. This allows subtle spatiotemporal statistics to be calculated, for example, the probability density function of the magnitude or timing of the minimum or maximum decadally averaged transport value

during the study period (Methods). Residual analyses and synthetic data experiments demonstrate the appropriateness of the algorithm and show that it accurately infers the quantities of interest given the data (Methods).

Weakening of the Florida Current

The probabilistic reconstruction of Florida Current transport is summarized in Figure 2. The 110-y mean transport is 32.6 ± 1.4 Sv (Supplementary Figure 3a; $1\ \mathrm{Sv} \equiv 10^6\ \mathrm{m^3\ s^{-1}}$). Unless otherwise indicated, $\pm$ values represent the median plus and minus twice the standard deviation inferred by the Bayesian model, which roughly corresponds to the 95% posterior credible interval. The average transport since 1982, when transport has been continuously monitored, is 31.8 ± 0.1 Sv. This value is likely weaker (probability $P = 0.86$) than the average transport during 1909–1981 (32.9 ± 2.1 Sv) before continuous monitoring of the Florida Current (Supplementary Figure 3a). Estimated uncertainties since 1982 are relatively small, and mostly reflect instrumental errors on the cable data, which strongly constrain the posterior solutions of the transport process. Before 1982, cable data are unavailable at $27°$N, and the inference is largely constrained by the tide-gauge records, which have a more uncertain relationship to transport and become sparser earlier in time, resulting in comparatively larger errors that grow into the past.

Superimposed on the time-mean are interannual-to-decadal fluctuations in transport (Figure 2). The standard deviation of annual transports is 1.3 Sv (posterior median estimate). A -3.3 ± 1.1 Sv weakening from 1997–1998 to 1999–2000, when there was a gap in cable data

and low transports were observed upstream in Yucatán Channel[45], was followed by a 2.5 ± 1.1 Sv strengthening between 1999–2000 and 2001–2002 (Supplementary Figure 3c). Decadal-average transports during 1922–1932 (33.6 ± 2.8 Sv) and 1956–1966 (33.0 ± 1.7 Sv) were likely ($P \geq 0.79$) higher than the longterm 110-y mean transport, whereas decadal-mean transports over 1946–1956 (32.2 ± 2.0 Sv) and 1986–1996 (31.7 ± 0.2 Sv) were likely lower than the longterm mean (Supplementary Figure 3d). Wavelet coherence analysis reveals that transport fluctuations can be related to major modes of surface climate variation (Supplementary Figure 4). Transport is probably ($P > 0.68$) coherent with the North Atlantic Oscillation[46] over 2–8-y periods centered between the late 1970s and early 2000s, consistent with past studies of the cable data[2,47]. Coherence is also evident at 2–4-y periods around 1960, and 8-y periods between the late 1930s and early 1950s, which have not been reported previously, and possibly result from changes in forcing by wind-stress curl over the subtropics and mediated by planetary Rossby waves[47]. Transport is also likely ($P > 0.68$) coherent with Atlantic Multidecadal Variability[48] at 2–16-y periods centered on the mid 1990s and 16-y periods from the late 1940s to early 2000s. Weaker coherence earlier in time could reflect nonstationary relationships between transport and climate or the growth of transport uncertainties into the past.

Weakening of the Florida Current transport is apparent on longer timescales. The centennial trend during 1909–2018 is -1.7 ± 3.7 Sv century^{-1}, which overlaps zero, but implies that the trend is likely negative ($P = 0.82$; Supplementary Figure 3b). The inference of a longterm weakening is qualitatively insensitive to the choice of time period. Computing changes between all pairs of non-overlapping decadal averages, I find that transport likely ($P > 0.68$) declined from one decade

to another 65% of the time (i.e., 65% of pixels in Figure 3 are blue and not stippled). Considering only changes over > 50-y intervals, I find that the percentage of periods showing a likely decline increases to 92% (Figure 3). For example, it is very likely ($P = 0.90$) that transport weakened from 1920–1930 (-2.1 ± 2.9 Sv) and from 1960–1970 (-1.4 ± 1.6 Sv) to the present more than expected from a stationary red-noise process. Indeed, if transport was stationary, extrema would be uniformly likely to occur at any point on a given time interval, whereas in the presence of a longterm decline, the maximum transport would be more likely to happen closer to the beginning, and the minimum transport closer to the end of the interval. Consistent with the latter case, the minimum decadal-average transport (31.1 ± 1.0 Sv) likely started sometime after 2002 ($P = 0.74$), whereas the maximum decadal average (34.1 ± 2.5 Sv) probably ended before 1936 ($P = 0.70$; Figure 4a). The timing of these extrema cannot be explained in terms of fluctuations about a stationary mean: after removing the longterm trend (Supplementary Figure 3b), I find it unlikely that the minimum transport started after 2002 ($P = 0.18$), and chances are lower that the maximum ended before 1936 ($P = 0.38$; Figure 4b).

Relation Between Florida Current Transport and Sea-Level Difference Across Florida Straits

In addition to transport, the Bayesian algorithm also estimates the regression coefficient between transport and sea-level difference across Florida Straits (see Methods). This estimated change in transport per unit change in sea-level difference is 0.21 ± 0.11 Sv cm^{-1} (Supplementary Figure 5a). I use geostrophy to interpret this value in terms of an effective depth characterizing the vertical scale over which velocity variations decay in amplitude from the surface to the bottom in Florida

Straits[49,50]. Following Little et al.[50], I multiply by the ratio of Coriolis parameter over gravity (6.7×10^{-6} s m^{-1} at 27°N) to obtain an effective depth of 144 ± 74 m. This estimate is roughly consistent with the vertical structure of northward currents observed by shipboard acoustic doppler current profiler aboard the research vessel Walton Smith during 70 cruises across Florida Straits at 27°N over 2001–2018. At the longitude of the core of the current, the average meridional velocity over all cruises decays almost linearly in the vertical from ~ 1.2 m s^{-1} near the surface to ~ 0.9 m s^{-1} and ~ 0.6 m s^{-1} at 200- and 400-m depth, respectively (Figure 5a). Computing standard deviations in meridional velocities across cruises, I find that the decay in flow-variation amplitude with depth takes a more exponential form, decreasing rapidly from ~ 0.6 m s^{-1} near the surface to ~ 0.3 m s^{-1} and ~ 0.2 m s^{-1} at 200- and 400-m depth, respectively (Figure 5b). Similar vertical structures of mean and variable meridional currents were reported from earlier observations made during 1982–1984 as part of the Subtropical Atlantic Climate Studies Program[51].

In designing the Bayesian algorithm, I assumed that the regression coefficient between sea level and transport is time invariant (see Methods). To test if this assumption is reasonable, I analyze sea level and transport simulated by an ocean circulation model[52] over 1871–2010 in the time and frequency domains. Performing admittance and coherence analyses[53], I determine that modeled sea-level differences across Florida Straits and Florida Current transports are coherent over all accessible timescales, and that the admittance (or transfer function) amplitude is relatively insensitive to frequency band, such that the change in transport per unit change in sea-level difference is similar at interannual and multidecadal timescales (Supplementary Figure 6). I also perform correlation and regression analyses on the simulated sea-level differences and transports

using a sliding 20-y time window. Correlation and regression coefficients are relatively robust to the choice of time period, such that values for any 20-y epoch are within about 20% and 5%, respectively, of the average value over all 20-y epochs over 1871–2010 (Supplementary Figure 7). These results show that the link between transport and sea-level difference in this ocean model is not strongly dependent on time period or frequency band, which suggests that my assumption of a constant-in-time regression coefficient between the two variables is justifiable. The Bayesian algorithm also successfully infers the correct regression-coefficient value in a synthetic data experiment based on this ocean circulation model (Methods; Supplementary Figures 6, 7), which means that the algorithm correctly estimates the relationship between sea level and transport given the available (gappy, noisy) data.

Distinguishing Dynamic and Static Trends in the Sea-Level Difference Across Florida Straits

The meaningfulness of the transport estimate hinges on the Bayesian algorithm's ability to identify and distinguish dynamic from static components of the sea-level difference across the Florida Straits, given the available data. Here "dynamic" indicates ocean dynamic sea level, which is the local sea-surface height relative to the geoid and corrected for the inverted-barometer effect, whereas "static" refers to relative sea-level changes unrelated to ocean circulation, including global-mean sea-level changes, the inverted-barometer effect, and sea-level changes arising from changes in Earth's gravity, rotation, and viscoelastic solid-Earth deformation[54]. The posterior solution for the 110-y trend in sea-level difference across the Florida Straits, between Grand Bahama minus West Palm Beach, is -0.2 ± 1.0 mm y^{-1} (Supplementary Figure 5b). This trend results from the com-

peting influences of a dynamic trend in sea-level difference of -0.9 ± 2.2 mm y^{-1} and a static trend of 0.7 ± 2.3 mm y^{-1} (Supplementary Figure 5b), which I interpret respectively as differential trends in sea-surface height and vertical land motion across Florida Straits.

Several lines of independent evidence corroborate these inferences, and support my interpretation in terms of sea-surface height and vertical land motion. The Global Positioning System (GPS) provides instrumental observations of vertical land motion. Version 6b of the dataset from Université de la Rochelle[55] gives continuous GPS records from three locations in southeastern Florida and two Bahamas locations (Supplementary Figure 8; Supplementary Table 1). I compute the average vertical velocity for the two Bahamas sites, and do the same for the three sites in southeastern Florida. Taking the difference between the two averages, I find that sea level is statically rising 1.0 ± 1.3 mm y^{-1} faster in the Bahamas than on southeastern Florida due to differential land subsidence. Here the $\pm$ value is the best estimate plus and minus twice the estimated standard error, assuming that the standard errors provided with the GPS data are independent (Supplementary Table 1). This rate of sea-level rise agrees with the static trend in the sea-level difference across Florida Straits inferred by the Bayesian model.

Proxy sea-level reconstructions are informative of background rates of change unrelated to ocean dynamics. I consider recent standardized compilations of Holocene sea-level index points from the Caribbean and southeastern USA derived from coral reefs, mangrove peats, and other indicators[56,57]. To estimate present-day rates of background change unrelated to circulation and climate, I only consider locations in the databases that have at least three sea-level index points

with best-estimate ages between 2,000 and 150 y before present. This criterion is satisfied by two southeastern Florida sites and one Bahamas site (Supplementary Figure 8; Supplementary Table 2). Taking the difference between the linear trend fit to the index points from the Bahamas site and the average of the trends fit to the data at the two southeastern Florida locations, I estimate that sea level rose 0.6 ± 0.6 mm y^{-1} more rapidly in the Bahamas relative to southeastern Florida in the pre-industrial Common Era (Supplementary Table 2). Here the $\pm$ value is the best estimate plus and minus twice the standard error from ordinary least squares applied to the best estimates of proxy age and sea level, assuming white-noise residuals. Interpreted in terms of vertical land motion, this sea-level trend difference from proxy data suggests that the difference in rates of vertical land motion between the Bahamas and southeastern Florida observed by GPS is, at least partly, due to background geological processes (e.g., glacial isostatic adjustment).

Modern radar altimeters have observed sea-surface height over nearly the global ocean since 1993. Once adjusted for static effects, altimeter data can be interpreted in terms of surface currents and ocean dynamics. I consider along-track sea-surface height from the Centre for Topography of the Oceans and the Hydrosphere[58] at the altimeter data points closest to Settlement Point on Grand Bahama Island and Virginia Key in southeastern Florida (Supplementary Figure 8). Differencing the two altimetric time series and fitting a linear trend, I determine that the rate of change in sea-surface-height difference across Florida Straits during 1993–2017 was -2.2 ± 3.0 mm y^{-1} (Supplementary Figure 9). Here $\pm$ is the best estimate plus and minus twice the estimated standard error based on simulations with synthetic time series, with the same Fourier amplitude as the data but random phase, to account for autocorrelation in the residuals[59,60] (see Supplementary

225 Information). This altimetric trend, while covering a relatively short interval, basically agrees in
226 sign and magnitude with the dynamic trend in sea-level difference across Florida Straits from the
227 Bayesian model. Note that, while closer to the western end point of the submarine cable than
228 Virginia Key, the West Palm Beach tide gauge is not considered. Due to the geometry of the
229 satellite tracks, the closest altimeter point to West Palm Beach is about 50 km offshore, east of the
230 current core, and does not reflect western boundary sea level (Figure 5; Supplementary Figure 8).

231 **Relation to Large-Scale North Atlantic Ocean Circulation**

232 Assuming there were no changes in Bering Strait throughflow, or evaporation and precipitation
233 over the basin, mass conservation demands that weakening of the Florida Current transport must
234 be balanced by equal and opposite changes in transports by other components of the circulation
235 at $27°$N. This mass-conservation requirement can be met by weakening of the southward-flowing
236 interior gyre, strengthening of the northward Antilles Current, weakening of the southward deep
237 return flow of the overturning, or some combination thereof.

238 To consider possible changes in wind-driven interior gyre transports, I compute geostrophic
239 Sverdrup streamfunction[9] using wind-stress curl from two reanalyses for the twentieth century[61,62].
240 I find a mean southward transport of between -21 and -25 Sv at $27°$N for 1900–2010 (Figure 6a).
241 This agrees with historical and modern estimates of the mean interior geostrophic gyre transport
242 at $27°$N from gridded wind products[5,11,63–65] and hydrographic observations[66] for different time
243 periods, which range from -16 to -27 Sv. However, the two reanalyses give conflicting estimates

of longterm trends in Sverdrup transport (Figure 6b; Supplementary Figure 10). For 1900–2010, one reanalysis[61] gives a weaker northward trend (1.9 ± 2.0 Sv century^{-1}), while the other[62] produces a stronger southward trend (-4.2 ± 1.3 Sv century^{-1}) at 27°N (Figure 6b). Here $\pm$ is the best estimate plus and minus twice the standard error based on synthetic data simulations to account for residual autocorrelation[59,60] (Supplementary Information). Discrepancies in Sverdrup transport trends are apparent broadly over the subtropics. One reanalysis[62] produces significant negative trends suggesting spin-up of the gyre, while the other[61] shows significant positive trends indicating gyre spin-down over 1900–2010 (Figure 6b). Such discrepancies are evident more generally at multidecadal and centennial periods. Considering all periods starting between 1900 and 1980 and ending in 2010, I consistently find significant trends in the residual difference in Sverdrup transport between reanalyses at 27°N (Supplementary Figure 10). These findings are unchanged if ageostrophic Ekman transports are also considered (Figure 6b; Supplementary Figure 10). Thus, while they do not paint a consistent portrait of whether the interior gyre strengthened or weakened over the past century, reanalyses suggest that longterm trends in gyre transports of several Sv century^{-1} are possible.

The Antilles Current is a subsurface western boundary current constrained to the upper slope east of Abaco at 26.5°N. Data from the RAPID array since 2004 show that the Antilles Current has a mean northward transport of between 1 and 6 Sv (refs.[6–8,66]). While weaker in a time-average sense, the Antilles Current transport is as variable as, if not more variable than, the Florida Current transport[7,8]. Variation in Antilles Current transport has been attributed to a combination of westward-propagating eddies and large-scale wind forcing associated with the Bermuda High[5,7].

Continuous measurements of Antilles Current transport during 1986–1991 and since 2004 (refs.[5,8]) are too short for diagnosing longterm trends. However, one can put bounds on stochastic trends based on the time-series properties of the available data. Performing simulations of a random stationary process, with the same integral timescale and variance as the observed Antilles Current transport over 2005–2015 (ref.[8]), I find that stochastic transport trends of ± 2.9 and ± 1.2 Sv century^{-1} are possible on 50- and 100-y timescales, respectively (Supplementary Information; Supplementary Figure 11). Here $\pm$ values are 95% confidence intervals determined from the simulations. These results imply that multidecadal and centennial trends in Antilles Current transport, on the same order of magnitude as the trends in Florida Current transport estimated here, cannot be ruled out.

Previous studies argued that the deep branch of the overturning circulation declined in the recent past[23–27]. These arguments were partly based on: (1.) strong correlation between overturning streamfunction and subpolar North Atlantic sea-surface temperature on multidecadal and longer timescales in climate models[23,24,67,68]; and (2.) observations[69,70] of a "warming hole" in the subpolar North Atlantic[23,24], where sea-surface temperature cooled by -0.6 ± 0.4 °C century^{-1} relative to the global average during 1909–2018 (Figures 7, 8). Here $\pm$ is the best estimate plus and minus twice the standard error accounting for residual autocorrelation[59,60] (Supplementary Information). However, it has been unclear what processes mediate links between the overturning and subpolar sea-surface temperature in models[71,72]. All else being equal, the trend in sea-surface temperature implies a trend in surface heat flux of 16 ± 11 W m^{-2} century^{-1} over the warming hole (Supplementary Information). If this heat was stored locally in the North Atlantic and Arctic

Ocean, from $27°$N to Bering Strait, it would manifest in an average temperature acceleration of 0.7 ± 0.5°C century^{-2} over the entire water column, or a full-depth warming of 0.4 ± 0.3°C during 1909–2018 (Supplementary Information). This is larger than published estimates of northern North Atlantic warming over the past century[73,74]. For example, the model-data synthesis of Gebbie and Huybers[73] suggests an average regional warming of ~ 0.1°C for 1910–2015 (Supplementary Figure 12). Thus, in addition to satisfying mass conservation, any circulation changes across $27°$N must also generate a heat transport divergence that, to leading order, balances the surface heat flux due to the declining subpolar sea-surface temperatures.

Knowing Florida Current transport and subpolar gyre sea-surface temperature, and requiring mass conservation at $27°$N and heat conservation across the North Atlantic and Arctic north of $27°$N, I estimate past changes in the deep branch of the overturning at $27°$N (see Supplementary Information for details and caveats). The estimate depends on the mean wind speed and sea-surface temperature over the warming hole as well as the vertical and horizontal temperature stratification at $27°$N (Supplementary Information). Making reasonable choices for these parameters, I estimate that the deep branch of the overturning slowed by 1.4 ± 1.8 Sv century^{-1} during 1909–2018 (Supplementary Figure 13a). Here $\pm$ is the best estimate plus and minus twice the standard error. More generally, for long periods starting before 1950 and ending in 2018, I find that best estimates of trends in the deep return flow are positive (northward) and more than one standard error from zero, whereas for shorter periods beginning more recently, errors are larger and trends are mostly indistinguishable from zero (Supplementary Figure 13a). This points to a probable decline in transport by the deep branch of the overturning circulation over the past 70–110 y, but reveals that any

trends in the deep return flow over shorter, more recent time periods cannot be detected from these principles and knowledge of the Florida Current transport and subpolar sea-surface temperature.

I also estimate past changes in the transport of the thermocline recirculation[75], defined as the sum of all interior upper-ocean circulations across $27°$N, including the Antilles Current and Sverdrup gyre (Supplementary Information). Given the weakening Florida Current transport and cooling subpolar sea-surface temperature, I estimate a thermocline recirculation trend of -0.3 ± 4.9 Sv century^{-1} for 1909–2018 (Supplementary Figure 13b). This value is more uncertain than the change estimated in the deep branch of the overturning circulation over the past century. The difference has to do with the dependence of ocean heat transport on temperature gradients. Vertical temperature gradients are much stronger than horizontal temperature gradients at $27°$N (Supplementary Figure 14). Thus, a change in the deep branch of the overturning leads to a larger heat transport than an equal change in the thermocline recirculation, given the weakening of the Florida Current. In consequence, there is a narrow window of transport histories of the deep return flow that, together with the cooling subpolar sea-surface temperature and weakening Florida Current transport, satisfy heat and mass conservation. There is a wider window of possibility for the thermocline recirculation that allows these constraints to be met. Indeed, thermocline recirculation trends computed for other time periods are similarly uncertain (Supplementary Figure 13b). This reveals that knowledge of past changes in the Florida Current and subpolar sea-surface temperature is relatively uninformative of the thermocline recirculation on long timescales.

Conclusions

Lack of knowledge regarding longterm changes in major ocean currents has been a key observational uncertainty related to climate change. I applied Bayesian data analysis[42–44] to observations from submarine cables and tide gauges to infer the changes in the Florida Current transport at 27°N during 1909–2018. I found that Florida Current transport probably declined steadily over the past century, such that transport since 1982 was likely weaker on average than it was during 1909–1981, and the weakest decadal-mean transport in the last 110 y probably took place in the past two decades. While past changes in the gyre circulation are uncertain, these results corroborate earlier hypotheses based on proxy indicators that the deep branch of the Atlantic meridional overturning circulation weakened continuously during the twentieth century[23–27]. These findings also support model simulations showing that changes in the deep return flow of the overturning circulation are nearly balanced by comparable changes in the surface western boundary current on multidecadal and longer timescales[28–32].

Future studies should build on this foundation. Uncertainties on this Florida Current transport estimate are large. More observations could be folded into a more general probabilistic framework to better constrain the transport over the past century. My goal was to quantify how informative tide-gauge sea-level data are of past changes in the Florida Current. However, I showed that the results were consistent with exploratory analyses of GPS data, sea-level index points, and satellite altimetry. These datasets could be assimilated by specifying additional equations in the Bayesian algorithm (e.g., following ref.[76]) to test whether Florida Current transports are better constrained

and uncertainties are reduced. There are also short records from the 1960s and 1970s of transport upstream in Florida Straits (e.g., at 26°N between Miami and Bimini[19–21]) that could be leveraged, provided that the uncertain flow through Northwest Providence Channel is taken into account. With a more tightly constrained estimate, it could be possible to identify the mechanisms responsible for past changes in Florida Current transport and the deep branch of the overturning circulation, and to determine whether the interior gyre strengthened or weakened.

Future studies should try to infer Florida Current transports earlier in time. Results here show that coastal sea-level data place valuable constraints on past changes in transport. Yet, the reconstruction was limited by the duration of the available tide-gauge records, which only go back about a century or so in this region[41]. Archival tidal data going back to the mid 1800s have been identified for several locations along the southeastern USA[77], which (if recovered and digitized) could allow for a longer reconstruction. New sea-level reconstructions derived from salt-marsh sediment along the Florida coast[78–80], with roughly decadal temporal resolution, might make it possible to reconstruct longer-term changes in Florida Current transport over the Common Era. Pseudoproxy experiments[81] will be informative to determine whether such a reconstruction is viable. If such a longterm reconstruction is possible, it would allow for a test of the hypothesis[13] based on oxygen isotope records from Dry Tortugas and Grand Bahama Bank that Florida Current transport strengthened by $\sim 10\%$ from the mid 1700s to the mid 1900s, at the same time that other proxy indicators suggest the deep branch of the overturning circulation was stable or in decline[23–27].

1. Larsen, J. C. Transport and heat flux of the Florida Current at 27°N derived from cross-stream voltages and profiling data: theory and observations, *Phil. Trans. R. Soc. A.*, **338**, 169–236 (1992).

2. Baringer, M. O., and J. C. Larsen. Sixteen years of Florida Current transport at 27°N, *Geophys. Res. Lett.*, **28**, 317–3182 (2001).

3. Meinen, C. S., M. O. Baringer, and R. F. Garcia. Florida Current transport variability: an analysis of annual and longer-period signals, *Deep-Sea Res.*, **57**, 835–846 (2010).

4. Garcia, R. F., and C. S. Meinen. Accuracy of Florida Current volume transport measurements at 27°N using multiple observational techniques, *J. Atmos. Ocean. Tech.*, **31**, 1169–1180 (2014).

5. Lee, T. N., W. E. Johns, R. J. Zantopp, and E. R. Fillenbaum. Moored observations of western boundary current variability and thermohaline ciruclation at 26.5°N in the subtropical North Atlantic, *J. Phys. Oceanogr.*, **26**, 962–983 (1996).

6. Johns, W. E., L. M. Beal, M. O. Baringer, J. R. Molina, S. A. Cunningham, T. Kanzow, and D. Rayner. Variability of shallow and deep western boundary currents off the Bahamas during 2004–05: results from the 26°N RAPID-MOC array, *J. Phys. Oceanogr.*, **38**, 605–623 (2008).

7. Frajka-Williams, E., W. E. Johns, C. S. Meinen, L. M. Beal, and S. A. Cunningham. Eddy impacts on the Florida Current, *Geophys. Res. Lett.*, **40**, 349–353 (2013).

8. Meinen, C. S., W. E. Johns, B. I. Moat, R. H. Smith, E. M. Johns, D. Rayner, E. Frajka-Williams, R. F. Garcia, and S. L. Garzoli. Structure and variability of the Antilles Current at $26.5°$N, *J. Geophys. Res.-Oceans*, **124**, 3700–3723 (2019).

9. Sverdrup, H. U. Wind-driven currents in a baroclinic ocean; with application to the Equatorial currents of the Eastern Pacific, *Proc. Natl. Acad. Sci. U.S.A.*, **33**, 318–326 (1947).

10. Stommel, H. The westward intensification of wind-driven ocean currents, *EOS T. Am. Geophys. Un.*, **29**, 202–206 (1948).

11. Schmitz, W. J., J. D. Thompson, and J. R. Luyten. The Sverdrup circulation for the Atlantic along $24°$N, *J. Geophys. Res.*, **97**(C5), 7251–7256 (1992).

12. McCarthy, G. D., D. A. Smeed, W. E. Johns, E. Frajka-Williams, B. I. Moat, D. Rayner, M. O. Baringer, C. S. Meinen, J. Collins, and H. L. Bryden. Measuring the Atlantic meridional overturning circulation at $26°$N, *Prog. Oceanogr.*, **130**, 91–111 (2015).

13. Lund, D. C., J. Lynch-Stieglitz, and W. B. Curry. Gulf Stream density structure and transport during the past millennium, *Nature*, **444**, 601–604 (2006).

14. Lynch-Stieglitz, J. The Atlantic meridional overturning circulation and abrupt climate change, *Annu. Rev. Mar. Sci.*, **9**, 83–104 (2017).

15. Palter, J. B. The role of the Gulf Stream in European climate, *Annu. Rev. Mar. Sci.*, **7**, 113–137 (2015).

16. Pillsbury, J. E. The Gulf Stream—a description of the methods employed in the investigation, and the results of the research, *Rept. Supt., US Coast Geod. Surv.*, **Appendix 10**, 461–620 (1890).

17. Hela, I. The fluctuations of the Florida Current, *B. Mar. Sci. Gulf Carib.*, **1**, 241–248 (1952).

18. Wunsch, C., D. V. Hansen, and B. D. Zetler. Fluctuations of the Florida Current inferred from sea level records, *Deep-Sea Res.*, **16**, 447–470 (1969).

19. Niiler, P. P., and W. S. Richardson. Seasonal variability of the Florida Current, *J. Mar. Res.*, **31**, 144–167 (1973).

20. Schmitz, W. J., and W. S. Richardson. On the transport of the Florida Current, *Deep-Sea Res.*, **15**, 679–693 (1968).

21. Brooks, I. H., and P. P. Niiler. Energetics of the Florida Current, *J. Mar. Res.*, **35**, 163–191 (1977).

22. Richardson, W., W. Schmitz, and P. Niiler. The velocity structure of the Florida Current from the Straits of Florida to Cape Fear, *Deep-Sea Res.*, **16**, 225–231 (1969).

23. Rahmstorf, S., J. E. Box, G. Feulner, M. E. Mann, A. Robinson, S. Rutherford, and E. J. Schaffernicht. Exceptional twentieth-century slowdown in Atlantic Ocean overturning circulation, *Nature Clim. Change*, **5**, 475–480 (2015).

24. Caesar, L., S. Rahmstorf, A. Robinson, G. Feulner, and V. Saba. Observed fingerprint of a weakening Atlantic Ocean overturning circulation, *Nature*, **556**, 191–196 (2018).

25. Thornalley, D. J. R., D. W. Oppo, P. Ortega, J. I. Robson, C. M. Brierley, R. Davis, I. R. Hall, P. Moffa-Sanchez, N. L. Rose, P. T. Spooner, I. Yashayaev, and L. D. Keigwin. Anomalously weak Labrador Sea convection and Atlantic overturning during the past 150 years, *Nature*, **556**, 227–230 (2018).

26. Thibodeau, B., C. Not, J. Hu, A. Schmittner, D. Noone, C. Tabor, J. Zhang, and Z. Liu. Last century warming over the Canadian Atlantic shelves linked to weak Atlantic meridional overturning circulation, *Geophys. Res. Lett.*, **45**, 12376–12385 (2018).

27. Moffa-Sánchez, P., E. Moreno-Chamarro, D. J. Reynolds, P. Ortega, L. Cunningham, D. Swingedouw, D. E. Amrhein, J. Halfar, L. Jonkers, J. H. Jungclaus, K. Perner, A. Wanamaker, and S. Yeager. Variability in the northern North Atlantic and Arctic Oceans across the last two millennia: a review, *Paleoceanogr. Paleocl.*, **34**, 1399–1436 (2019).

28. Thomas, M. D., A. M. de Boer, D. P. Stevens, and H. L. Johnson. Upper ocean manifestations of a reducing meridional overturning circulation, *Geophys. Res. Lett.*, **39**, L16609 (2012).

29. Beadling, R. L., J. L. Russell, R. J. Stouffer, and P. J. Goodman. Evaluation of subtropical North Atlantic Ocean circulation in CMIP5 models against the observational array at $26.5°$N and its changes under continued warming, *J. Clim.*, **31**, 9697–9718 (2018).

30. Gu, S., Z. Liu, and L. Wu. Time scale dependence of the meridional coherence of the Atlantic meridional overturning circulation, *J. Geophys. Res.-Oceans*, **125**, e2019JC015838 (2020).

31. Moreno-Chamarro, E., P. Ortega, F. González-Rouco, and M. Montoya. Assessing reconstruction techniques of the Atlantic Ocean circulation during the last millennium, *Clim. Dyn.*, **47**, 799–819 (2017).

32. Gu, S., Z. Liu, J. Lynch-Steiglitz, A. Jahn, J. Zhang, K. Lindsay, and L. Wu. Assessing the ability of zonal δ^{18}O contrast in benthic foraminifera to reconstruct deglacial evolution of Atlantic meridional overturning circulation, *Paleoceanogr. Paleocl.*, **34**, 800–812 (2019).

33. Maul, G. A., F. Chew, M. Bushnell, and D. A. Mayer. Sea level variation as an indicator of Florida Current volume transport: comparisons with direct measurements, *Science*, **227**, 304–307 (1985).

34. Park, J., and W. Sweet. Accelerated sea level rise and Florida Current transport, *Ocean Sci.*, **11**, 607–615 (2015).

35. Schott, F., and R. Zantopp. Florida Current: seasonal and interannual variability, *Science*, **227**(4684), 308–311 (1985)

36. Iselin, C. O. Preliminary report on long-period variations in the transport of the Gulf-Stream system, *Papers in physical oceanography and meteorology published by Massachusetts Institute of Technology and Woods Hole Oceanographic Institution*, **8**(1), 40 pp (1940).

37. Sturges, W., and B. G. Hong. Gulf Stream transport variability at periods of decades, *J. Phys. Oceanogr.*, **31**, 1304–1312.

38. Kopp, R. E., C. C. Hay, C. M. Little, and J. X. Mitrovica. Geographic variability of sea-level change, *Curr. Clim. Change Rep.*, **1**, 192–204 (2015).

458 39. Horton, B. P., R. E. Kopp, A. J. Garner, C. C. Hay, N. S. Khan, K. Roy, and T. A. Shaw.
459 Mapping sea-level change in time, space, and probability, *Annu. Rev. Environ. Resourc.*, **43**,
460 481–521 (2018).

461 40. Woodworth, P. L., A. Melet, M. Marcos, R. D. Ray, G. Wöppelmann, Y. N. Sasaki, M. Cirano,
462 A. Hibbert, J. M. Huthnance, S. Monserrat, and M. A. Merrifield. Forcing factors affecting sea
463 level changes at the coast, *Surv. Geophys.*, **40**, 1351–1397 (2019).

464 41. Holgate, S. J., A. Matthews, P. L. Woodworth, L. J. Rickards, M. E. Tamisiea, E. Bradshaw,
465 P. R. Foden, K. M. Gordon, S. Jevrejeva, and J. Pugh. New data systems and products at the
466 Permanent Service for Mean Sea Level, *J. Coastal Res.*, **29**, 3, 493–504 (2013).

467 42. Tingley, M. P., P. F. Craigmile, M. Haran, B. Li, E. Mannshardt, and B. Rajaratnam. Piecing
468 together the past: statistical insights into paleoclimatic reconstructions, *Quat. Sci. Rev.*, **35**,
469 1–22 (2012).

470 43. Ashe, E. L., N. Cahill, C. Hay, N. S. Khan, A. Kemp, S. E. Engelhart, B. P. Horton, A. C.
471 Parnell, and R. E. Kopp. Statistical modeling of rates and trends in Holocene relative sea level,
472 *Quat. Sci. Rev.*, **204**, 58–77 (2019).

473 44. Cressie, N., & C. K. Wikle. Statistics for spatio-temporal data, John Wiley & Sons, 588 pp
474 (2011).

475 45. Sheinbaum, J. J. Candela, A. Badan, and J. Ochoa. Flow structure and transport in the Yucatan
476 Channel, *Geophys. Res. Lett.*, **29**, 1040 (2002).

477 46. Jones, P. D., T. Jonsson, and D. Wheeler. Extension to the North Atlantic Oscillation using
478 early instrumental pressure observations from Gibraltar and South-West Iceland, *Int. J. Clima-*
479 *tol.*, **17**, 1433–1450 (1997).

480 47. DiNezio, P. N., L. J. Gramer, W. E. Johns, C. S. Meinen, and M. O. Baringer. Observed
481 interannual variability of the Florida Current: wind forcing and the North Atlantic Oscillation,
482 *J. Phys. Oceanogr.*, **39**, 721–736 (2009).

483 48. Enfield, D. B., A. M. Mestas-Nuñez, and P. J. Trimble. The Atlantic multidecadal oscillation
484 and its relation to rainfall and river flows in the continental U.S., *Geophys. Res. Lett.*, **28**, 2077–
485 2080 (2001)

486 49. Bingham, R. J., and C. W. Hughes. Signature of the Atlantic meridional overturning circulation
487 in sea level along the east coast of North America, *Geophys. Res. Lett.*, **36**, L02603 (2009).

488 50. Little, C. M., A. Hu, C. W. Hughes, G. D. McCarthy, C. G. Piecuch, R. M. Ponte, and M. D.
489 Thomas. The relationship between United States East Coast sea level and the Atlantic merid-
490 ional overturning circulation: a review, *J. Geophys. Res.-Oceans*, **124**, 6435–6458 (2019).

491 51. Leaman, K. D., R. L. Molinari, and P. S. Vertes. Structure and variability of the Florida Current
492 at 27°N: April 1982–July 1984, *J. Phys. Oceanogr.*, **17**, 565–583 (1987).

493 52. Giese, B. S., and S. Ray. El Ninõ variability in simple ocean data assimilation (SODA), 1871–
494 2008, *J. Geophys. Res.*, **116**, C02024 (2011).

495 53. Emery, R. E., and W. J. Thomson. Data analysis methods in physical oceanography, 3rd Edi-
496 tion, Elsevier, 728 pp (2014).

497 54. Gregory, J. M., S. M. Griffies, C. W. Hughes, J. A. Lowe, J. A. Church, I. Fukumori, N.
498 Gomez, R. E. Kopp, F. Landerer, G. Le Cozannet, R. M. Ponte, D. Stammer, M. E. Tamisiea,
499 and R. S. W. van de Wal. Concepts and terminology for sea level: mean, variability, and change,
500 both local and global, *Surv. Geophys.*, **40**, 1251–1289 (2019).

501 55. Santamaría-Gómez, A., M. Gravelle, S. Dangendorf, M. Marcos, G. Spada, and G.
502 Wöppelmann. Uncertainty of the 20th century sea-level rise due to vertical land motion errors,
503 *Earth Planet. Sci. Lett.*, **473**, 24–32 (2017).

504 56. Khan, N. S., E. Ashe, B. P. Horton, A. Dutton, R. E. Kopp, G. Brocard, S. E. Engelhart, D. F.
505 Hill, W. R. Peltier, C. H. Vane, and F. N. Scatena. Drivers of Holocene sea-level change in the
506 Caribbean, *Quat. Sci. Rev.*, **155**, 13–36 (2017).

507 57. Love, R., G. A. Milne, L. Tarasov, S. E. Engelhart, M. P. Hijma, K. Latychev, B. P. Horton,
508 and T. E. Törnqvist. The contribution of glacial isostatic adjustment to projections of sea-level
509 change along the Atlantic and Gulf coasts of North America, *Earth's Future*, **4**, 440–464 (2016).

510 58. Birol, F., N. Fuller, F. Lyard, M. Cancet, F. Niño, C. Delebecque, S. Fleury, F. Toublanc, A.
511 Melet, M. Saraceno, and F. Léger. Coastal applications from nadir altimetry: example of the
512 X-TRACK regional products, *Adv. Space Res.*, **59**, 936–953 (2017).

513 59. Theiler, J., S. Eubank, A. Longtin, B. Galdrikian, and J. D. Farmer. Testing for nonlinearity in
514 time series: the method of surrogate data, *Physica D*, **58**, 77–94 (1992).

515 60. Bos, M. S., S. D. P. Williams, I. B. Araújo, & L. Bastos. The effect of temporal correlated
516 noise on the sea level rate and acceleration uncertainty, *Geophys. J. Int.*, **196**, 1423–1430.

517 61. Compo, G. P., J. S. Whitaker, P. D. Sardeshmukh, N. Matsui, R. J. Allan, X. Yin, B. E. Gleason,
518 R. S. Vose, G. Rutledge, P. Bessemoulin, S. Brönnimann, M. Brunet, R. I. Crouthamel, A. N.
519 Grant, P. Y. Groisman, P. D. Johns, M. C. Kruk, A. C. Kruger, G. J. Marshall, M. Maugeri, H.
520 Y. Mok, Ø. Nordli, T. F. Ross, R. M. Trigo, X. L. Wang, S. D. Woodruff, and S. J. Worley. The
521 Twentieth Century Reanalysis Project, *Q. J. R. Meteorol. Soc.*, **37**, 1–28 (2011).

522 62. Poli, P., H. Hersbach, D. Tan, D. Dee, J.-N. Thépaut, A. Simmons, C. Peubey, P. Laloyaux,
523 T. Komori, P. Berrisford, R. Dragani, Y. Trémolet, E. Hólm, M. Bonavita, L. Isaksen, and M.
524 Fisher. ERA-20C: An atmospheric reanalysis of the twentieth century, *J. Clim.*, **29**, 4083–4097
525 (2016).

526 63. Leetmaa, A., and A. F. Bunker. Updated charts of the mean annual wind stress, convergences
527 in the Ekman layers, and Sverdrup transports in the North Atlantic, *J. Mar. Res.*, **36**, 311–322
528 (1978).

529 64. Böning, C. W., R. Döscher, and J.-J. Isemer. Monthly mean wind stress and Svedrup transports
530 in the North Atlantic: a comparison of the Hellerman-Rosenstein and Isemer-Hasse climatolo-
531 gies, *J. Phys. Oceanogr.*, **21**, 221–235 (1991).

532 65. Johns, W. E., T. L. Townsend, D. M. Fratatoni, and W. D. Wilson. On the Atlantic inflow to
533 the Caribbean Sea, *Deep-Sea Res.*, **49**, 211–243 (2002).

534 66. Smeed, D. A., S. A. Josey, C. Beaulieu, W. E. Johns, B. I. Moat, E. Frajka-Williams, D.
535 Rayner, C. S. Meinen, M. O. Baringer, H. L. Bryden, and G. D. McCarthy. The North Atlantic
536 Ocean is in a state of reduced overturning, *Geophys. Res. Lett.*, **45**, 1527–1533 (2018).

537 67. Drijfhout, S., G. J. van Oldenborgh, and A. Cimatoribus. Is a decline of AMOC causing the
538 warming hole above the North Atlantic in observed and modeled warming patterns?, *J. Clim.*,
539 **25**, 8373–8379 (2012).

540 68. Roberts, C. D., F. K. Garry, and L. C. Jackson. A multimodel study of sea surface temperature
541 and subsurface density fingerprints of the Atlantic meridional overturning circulation, *J. Clim.*,
542 **26**, 9155–9174 (2013).

543 69. Rayner, N. A., D. E. Parker, E. B. Horton, C. K. Folland, L. V. Alexander, D. P. Rowell, E. C.
544 Kent, and A. Kaplan. Global analyses of sea surface temperature, sea ice, and night marine air
545 temperature since the late nineteenth century, *J. Geophys. Res.*, **108**, 4407 (2003).

546 70. Kaplan, A., M. A. Cane, Y. Kushnir, A. C. Clement, M. Benno Blumenthal, and B. Ra-
547 jagopalan. Analyses of global sea surface temperature 1856–1991, *J. Geophys. Res.*, **103**,
548 18567–18589 (1998).

549 71. Lozier, M. S. Deconstructing the conveyor belt, *Science*, **328**, 1507–1511 (2010).

550 72. Buckley, M. W., and J. Marshall. Observations, inferences, and mechanisms of Atlantic merid-
551 ional overturning circulation variability: a review, *Rev. Geophys.*, **54**, 5–63 (2016).

552 73. Gebbie, G., and P. Huybers. The Little Ice Age and 20th-century deep Pacific cooling, *Science*,
553 **363**, 70–74 (2019).

554 74. Zanna, L., S. Khatiwala, J. M. Gregory, J. Ison, and P. Heimbach. Global reconstruction of
555 historical ocean heat transport and transport, *Proc. Natl. Acad. Sci. U.S.A.*, **116**(4), 1126–1131
556 (2019).

557 75. Kanzow, T., S. A. Cunningham, D. Rayner, J. J.-M. Hirschi, W. E. Johns, M. O. Baringer, H.
558 L. Bryden, L. M. Beal, C. S. Meinen, and J. Marotzke. Observed flow compensation associated
559 with the MOC at 26.5°N in the Atlantic, *Science*, **317**, 938–941 (2007).

560 76. Piecuch, C. G., P. Huybers, C. C. Hay, A. C. Kemp, C. M. Little, J. X. Mitrovica, R. M.
561 Ponte, and M. P. Tingley. Origin of spatial variation in US East Coast sea-level trends during
562 1900–2017, *Nature*, **564**, 400–404 (2018).

563 77. Talke, S. A., and D. A. Jay. Nineteenth century North American and Pacific tidal data: lost or
564 just forgotten? *J. Coastal. Res.*, **29**(6A), 118–127 (2013).

565 78. Kemp, A. C., C. E. Bernhardt, B. P. Horton, R. E. Kop, C. H. Vane, W. R. Peltier, A. D.
566 Hawkes, J. P. Donnelly, A. C. Parnell, and N. Cahill. Late Holocene sea- and land-level change
567 on the U.S. southeastern Atlantic coast, *Mar. Geol.*, **357**, 90–100 (2014).

568 79. Hawkes, A. D., A. C. Kemp, J. P. Donnelly, B. P. Horton, W. R. Peltier, N. Cahill, D. F. Hill,
569 E. Ashe, and C. R. Alexander. Relative sea-level change in northeastern Florida (USA) during
570 the last ~ 8.0 ka, *Quat. Sci. Rev.*, **142**, 90–101 (2016).

571 80. Gerlach, M. J., S. E. Engelhart, A. C. Kemp, R. P. Moyer, J. M. Smoak, C. E. Bernhardt, and
572 N. Cahill. Reconstructing Common Era relative sea-level change on the Gulf Coast of Florida,
573 *Mar. Geol.*, **390**, 254–269 (2017).

574 81. Smerdon, J. E. Climate models as a test bed for climate reconstruction methods: pseudoproxy
575 experiments, *WIREs Clim. Change*, **3**, 63–77 (2012).

576 82. Lumpkin, R., and G. C. Johnson. Global ocean surface velocities from drifters: mean, vari-
577 ance, El Niño-Southern Oscillation response, and seasonal cycle, *J. Geophys. Res.-Oceans*, **118**,
578 2992–3006 (2013).

579 **Supplementary Information** is linked to the online version of the paper at www.nature.com/ncomms.

580 **Acknowledgements** Funding came from NSF awards OCE-1558966 and OCE-1834739. I acknowledge
581 helpful conversations with M. Andres, L. Beal, S. Coats, S. Dangendorf, S. Elipot, T. Frederikse, N. Foukal,
582 G. Gawarkiewicz, G. Gebbie, B. Hamlington, J. Heiderich, A. Kemp, Y.-O. Kwon, F. Landerer, C. Little,
583 M. Thomas, and S. Wijffels. Comments from E. Ashe and two other anonymous reviewers are very much
584 appreciated and helped substantially improve the manuscript.

585 **Author Contributions** C.G.P. conceived the study, formulated the model framework, performed the anal-
586 yses, and wrote the manuscript.

587 **Competing Interests** The author declares that he has no competing financial interests.

588 **Correspondence** Correspondence and requests should be addressed to C.G.P. (cpiecuch@whoi.edu).

589 **Data Availability** The source data underlying Fig 2 are provided as a Source Data file. The tide-gauge data
590 and submarine cable data that support the main findings of this study are available from the Permanent Ser-
591 vice for Mean Sea Level (PSMSL; http://www.psmsl.org/) and the National Oceanic and Atmospheric Ad-
592 ministration Atlantic Oceanographic and Meteorological Laboratory (NOAA AOML; https://www.aoml.noaa.gov/),
593 respectively. Ancillary data sets, used for interpretation and not incorporated into the Bayesian model, and
594 their availabilities are as follows: Surface drifter data of surface current speeds shown in Figure 1a are avail-

able from NOAA AOML; Global Digital Elevation Model bathymetry shown in Figures 1b, 4 and Supplementary Figure 14 are available from NOAA National Geophysical Data Center (NGDC; https://www.ngdc.noaa.gov/); Cruise data from the research vessel Walton Smith shown in Figure 5 are available from NOAA AOML; Reanalysis wind-stress fields shown in Figure 6 and Supplementary Figure 10 are available from the Woods Hole Oceanographic Institution Community Storage Server (WHOI CCS; https://cmip5.whoi.edu); Gridded data sets of sea-surface temperature shown in Figures 7 and 8 are available from the UK Met Office Hadley Centre (https://www.metoffice.gov.uk/hadobs/) and NOAA Earth System Research Laboratory Physical Sciences Division (ESRL PSD; https://www.esrl.noaa.gov/psd/); Results from the model-data synthesis of Gebbie and Huybers[73] shown in Supplementary Figure 12 are available from the NOAA National Centers for Environmental Information (NOAA NCEI; https://data.nodc.noaa.gov/cgi-bin/iso?id=noaa-model-26611); Climatological ocean temperatures shown in Supplementary Figure 14 are from the World Ocean Atlas 2018 available from NOAA NCEI (https://www.nodc.noaa.gov/OC5/woa18/); Time series of climate indices shown in Supplementary Figure 4 are available from NOAA ESRL PSD; Global Positioning System data of vertical land motion rates shown in Supplementary Table 1 are available from Système d'Observation du Niveau des Eaux Littorales (SONEL; http://www.sonel.org/); Proxy relative sea-level index points shown in Supplementary Table 2 are taken from Khan et al.[56] and Love et al.[57]; Satellite-altimetric time series of sea-surface height shown in Supplementary Figure 9 are available from Centre of Topography of the Oceans and the Hydrosphere (CTOH; http://http://ctoh.legos.obs-mip.fr/); Model estimates of glacial isostatic adjustment rates used in the synthetic data experiments are available from PSMSL; Global-mean thermosteric sea level from the Community Climate System Model Version 4 used in the synthetic data experiments was downloaded from the WHOI CCS; Model solutions from the Simple Ocean Data Experiment (SODA) shown in Supplementary Figures 6, 7, 23 and used in the synthetic data experiments are available from the University of Hawaii Asia-Pacific Data-Research Center (http://apdrc.soest.hawaii.edu/).

Code Availability Statement The computer code used to run the Bayesian model and produce the results in this study, written in the MATLAB software environment, is available at the corresponding author's GitHub website (https://github.com/christopherpiecuch), along with the complete Bayesian model solution for all processes and parameters.

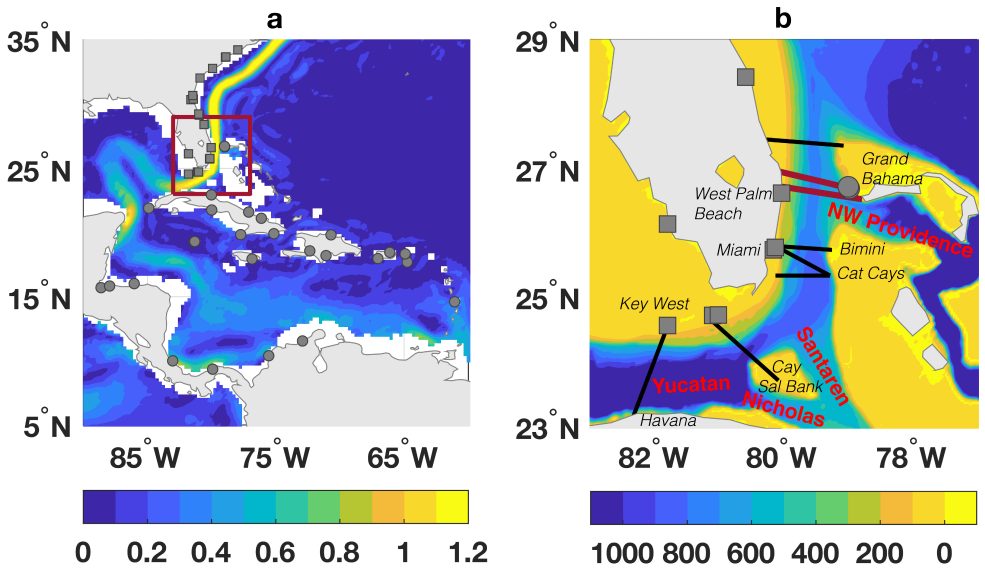

622

623 **Figure 1. Florida Current and study region. a,** Gray squares (circles) are locations of tide gauges
624 in the southeastern USA (Caribbean). Shading is mean ocean surface current speed (m s^{-1}) from
625 surface-drifter data[82]. Red box is area shown in (b). **b,** Details of Florida Straits. Shading is ocean
626 depth (m). Red bold (black oblique) font indicates ocean channels (land locations) mentioned in
627 the text. Thick red lines are locations of submarine cable measurements[1–4]. Thin black lines are
628 locations of *in situ* measurements from past studies[18–21].

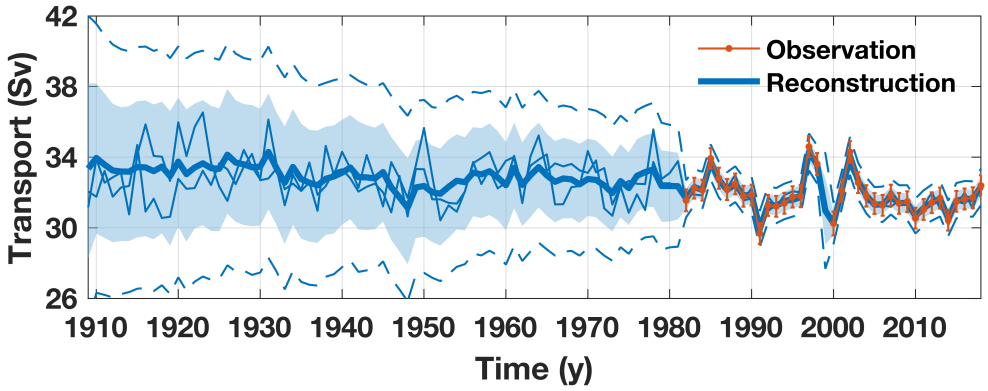

Figure 2. Florida Current transport. Blue shows posterior median (thick line), 95% pointwise (light shading) and pathwise (dash dot) credible intervals, along with two arbitrary, randomly selected ensemble members (thin lines) from the probabilistic Florida Current transport solution. Orange shows annual transport from raw submarine cable data plus and minus twice the standard error estimated following refs.[3,4].

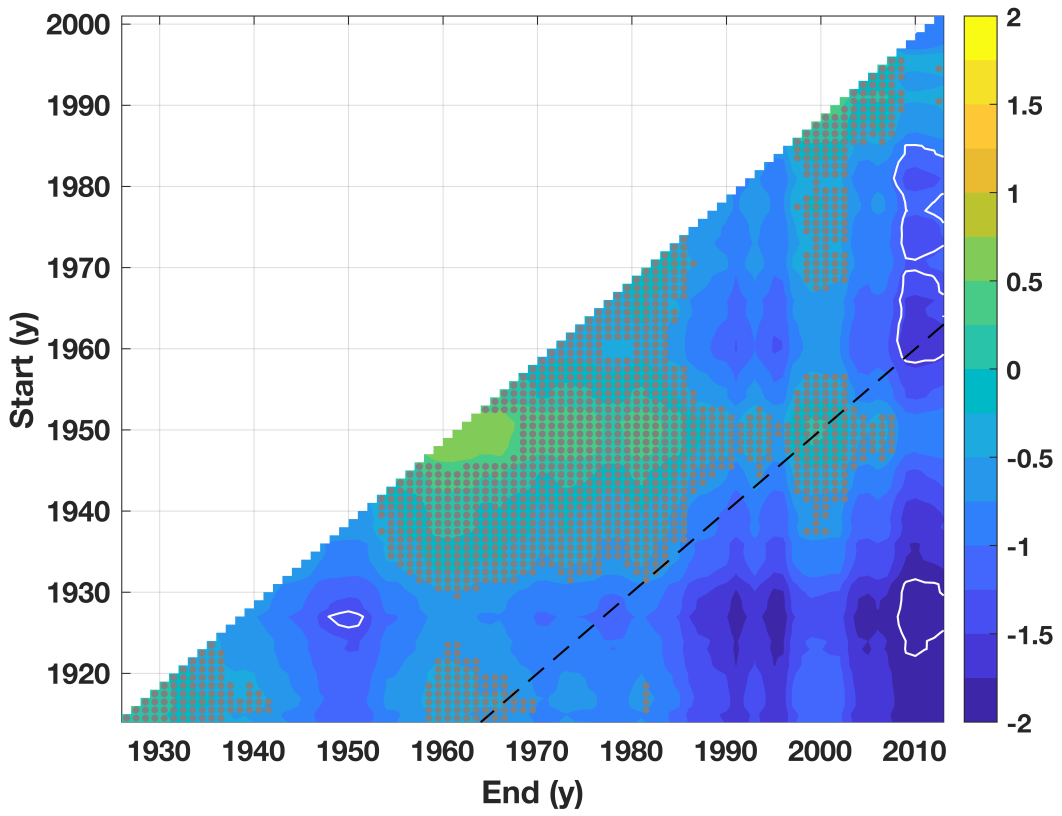

Figure 3. Weakening of Florida Current transport over different periods. Shading shows posterior median estimates of the change in decadal-average Florida Current transport between all pairs of decades (Sv). Negative values indicate that transport fell between the start and the end of the period. Stippling indicates that it is as likely as not ($0.33 < P < 0.67$) that transport rose or fell. White (black) contours encircle periods when it is very likely ($P > 0.90$) that transport weakened (strengthened) from the start to the end decade more than expected from a stationary red noise process; see Methods for discussion of significance calculations. Black dashes mark > 50-y periods (values below and to the right of the line correspond to periods with duration > 50 y).

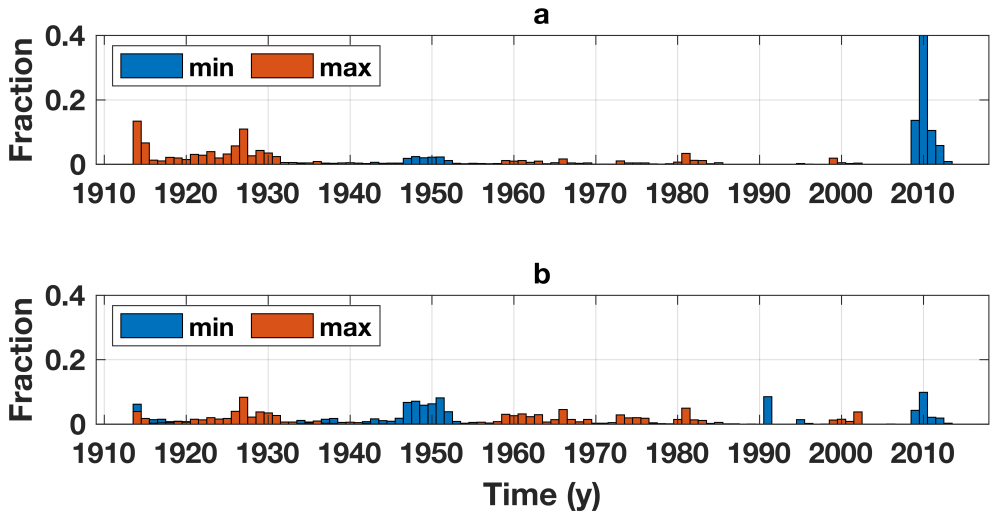

644

645 **Figure 4. Timing of Florida Current decadal transport extrema. a,** Histograms of modeled
646 probabilities that the minimum (blue) and maximum (orange) decadal average transport occurred
647 centered on a given year. **b,** As in (a) but histograms were calculated after removing the corre-
648 sponding longterm trend. See Methods for discussion of statistics and uncertainty measures.

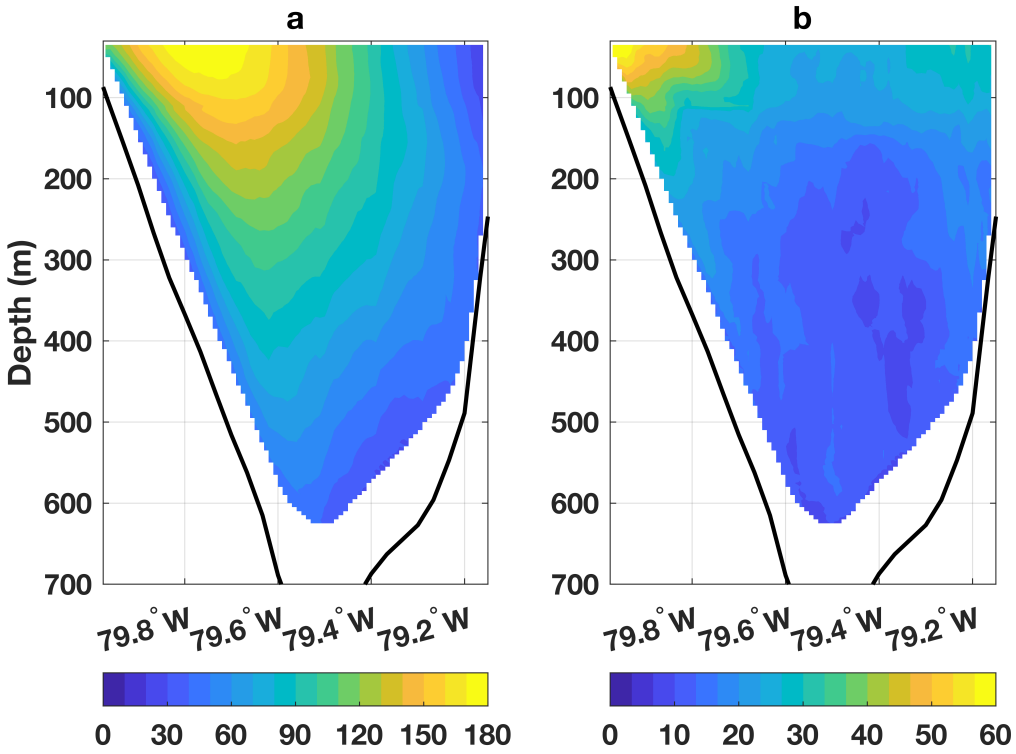

649

650 **Figure 5. Structure of the Florida Current within Florida Straits. a,** Mean northward velocities
651 (m s^{-1}) through Florida Straits from shipboard acoustic doppler current profiler data from 70
652 research cruises of the research vessel Walton Smith between 2001–2018. Values are computed by
653 interpolating all data between 26.9°N and 27.1°N from a given cruise onto a common grid using
654 a linear scattered data interpolant, and then averaging over all cruises. For a value to be shown
655 at a longitude and depth, data must have been available from at least 14 cruises. **b,** As in (a) but
656 showing the standard deviation in meridional velocities (m s^{-1}) across cruises. Black lines mark
657 the bathymetry.

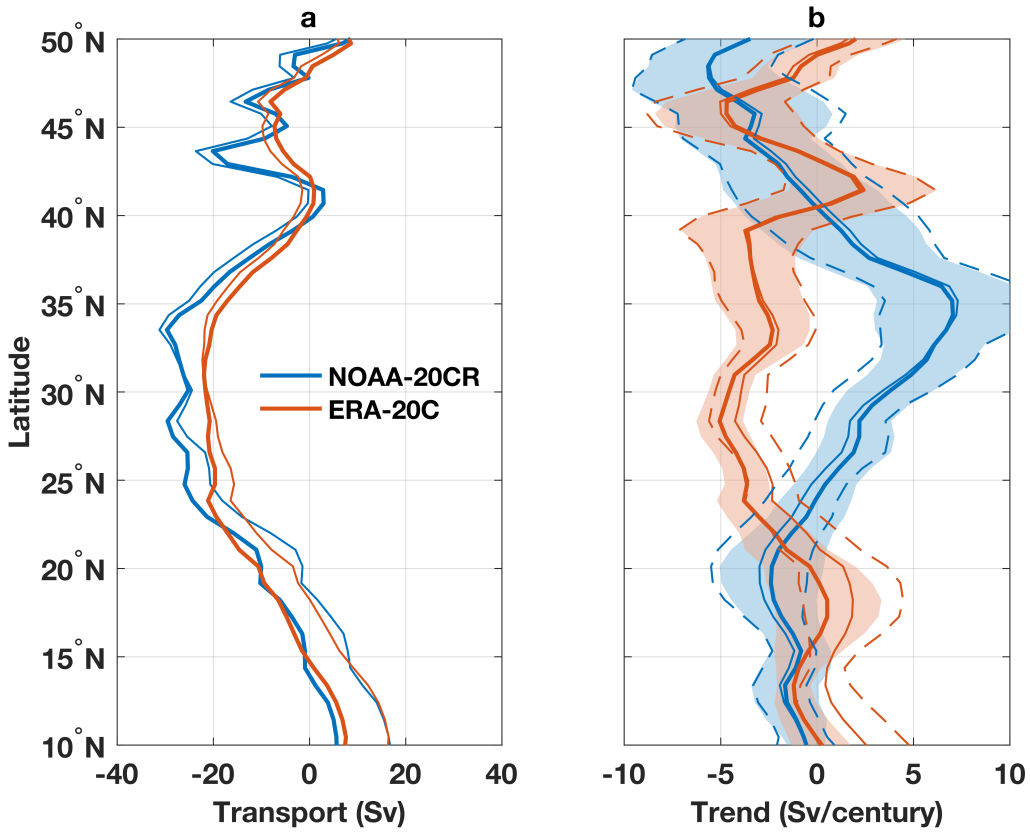

658

659 **Figure 6. Changes in wind-stress curl and gyre circulation.** **a,** Thick lines are time-mean
660 geostrophic Sverdrup streamfunction[9] based on wind-stress curl from NOAA 20CR[61] and ERA
661 20C[62] reanalyses over 1900–2010 as a function of latitude in the North Atlantic. Thin lines are the
662 same, but also incorporate the ageostrophic Ekman transport integrated across the basin. **b,** Median
663 estimates (thick lines) and formal 95% confidence intervals (colored shading) of the trend in Sver-
664 drup streamfunction versus latitude during 1900–2010 from the two reanalyses. Thin and dashed
665 lines represent median estimates and confidence intervals, respectively, with Ekman transports also
666 included.

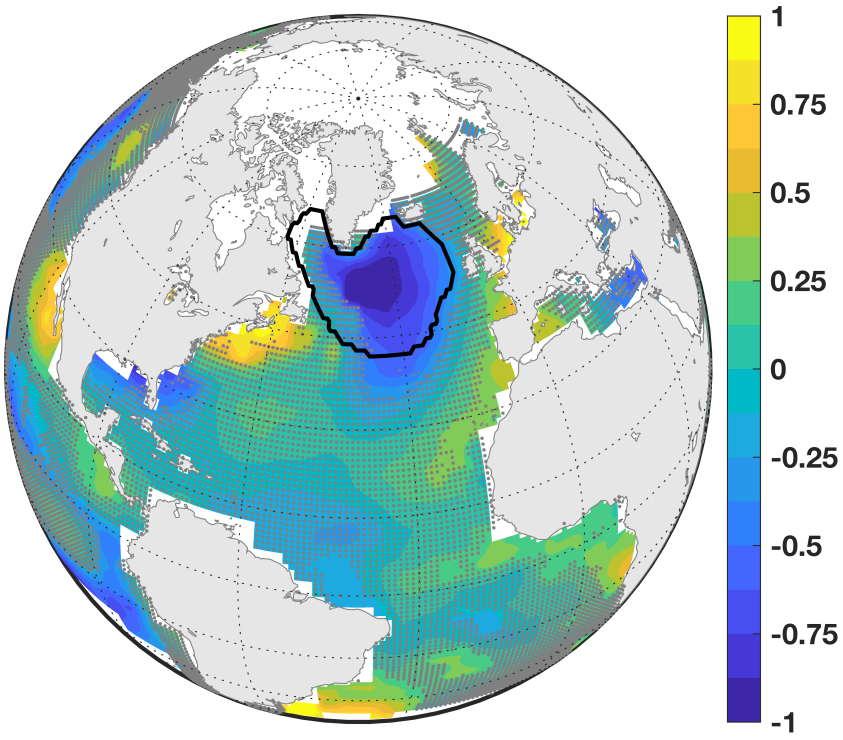

667

668 **Figure 7. Changes in sea-surface temperature.** Shading shows trends in sea-surface temperature
669 over 1909–2018 (°C century^{-1}) averaged over two products: HadISST[69] and Kaplan[70]. Stippling
670 indicates that the magnitude of the trend is less than twice the standard error estimated taking into
671 account autocorrelation of the residuals[59,60] as described in the Supplementary Information. The
672 black contour outlines the "warming-hole" region of Caesar et al.[24]. Note that the time series of
673 global-ocean area-averaged sea-surface temperatures has been removed before computing trends.

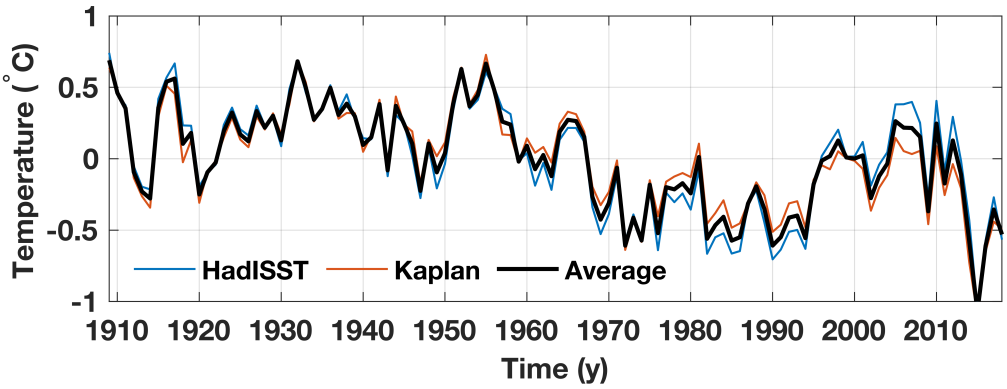

674

675 **Figure 8. Sea-surface-temperature changes over the warming hole.** Time series of anomalous
676 sea-surface temperature (°C; time-mean value removed) averaged over the "warming-hole" region
677 of Caesar et al.[24] (see black contouring in Figure 7) from HadISST[69] (blue), Kaplan[70] (orange),
678 and the average between the two products (black). Note that the time series of global-ocean area-
679 averaged sea-surface temperatures has been removed.

Methods

Observational data used in the Bayesian model I use annual relative sea level from 46 tide gauges along the southeastern USA (19 records), Caribbean Islands (20 records), southeastern Central America (5 records), and northern South America (2 records) during 1909–2018 (Figure 1a; Supplementary Figures 1, 2; Supplementary Table 3). Data were downloaded from the Permanent Service for Mean Sea Level (PSMSL) Revised Local Reference (RLR) database[41] on 4 February 2019. The study period is the longest interval such that, for each year, data is available from at least one southeastern USA tide gauge and at least one gauge in the Caribbean Islands, southeastern Central America, or northern South America. Over the study period, each tide gauge returns on average ~ 30 y of data, but some have as few as ~ 10 y of data, whereas others have as many as ~ 100 y. Fewer data are available earlier in time. The time series together constitute 1,390 y of data over the study period (27% completeness).

I also use Florida Current transport from submarine telephone cables at 27°N between West Palm Beach and Grand Bahama (Figures 1b, 2)[1–4]. Using electromagnetic theory, one can estimate changes in the flow from voltages induced across the cable due to the transport of charged particles by the variable current[1]. The original cable spanned from Jupiter Inlet to Settlement Point, giving measurements from 18 March 1982 to 22 October 1998. Observations resumed on 19 June 2000 based on a cable running from West Palm Beach to Eight Mile Rock. Cable-based transport estimates are calibrated against independent observations from dropsonde and lowered acoustic doppler current profiler made as part of regular (roughly bi-monthly) cruises across Florida

Straits[3,4]. Data are provided by the National Oceanic and Atmospheric Administration (NOAA) at 1-day intervals, but the data have an effective sampling rate of 3 days, due to low-pass filtering applied to the original observations. I use annual averages of the daily data (Figure 2). To estimate standard errors on the annual averages, I divide the standard error on the daily data ($\sim$ 1.7 Sv; ref.[4]) by the square root of the effective degrees of freedom, which is the number of daily transport measurements in a year divided by the integral timescale of Florida Current transport ($\sim$ 10 days; ref.[3]). This gives standard errors of 0.30–0.35 Sv, depending on data availability in any given year, consistent with values computed by Garcia and Meinen[4]. Note that Bayesian model solutions are not overly sensitive to the standard errors placed on the cable data, and similar results are found if the errors are doubled (see below).

Bayesian framework

I apply a hierarchical dynamical spatiotemporal model[42–44] to the submarine-cable data and tide-gauge records to infer annual changes in Florida Current transport and coastal sea level. The model comprises three levels: a process level describing how the physical quantities of interest relate to one another, and vary in space and time; a data level specifying how the imperfect available data correspond to the quantities of interest; and a parameter level placing prior constraints on the uncertain parameters in the process and data levels. My model builds on the Bayesian algorithm of Piecuch et al.[76], who studied the origin of spatial variation in sea-level trends on the east coast of the USA during 1900–2017. Here I develop new equations to consider an expanded geographic region, incorporate the submarine-cable data, and represent the relationship between Florida Current

transport and the difference in coastal sea level across the Florida Straits. See below for residual analyses and synthetic data experiments that establish the appropriateness of the model given the data, and exemplify its ability to accurately estimate the quantities of interest given the available incomplete, noisy, biased data.

Process level

Coastal sea level Coastal relative sea level is a process with spatiotemporal covariance[60,83]. As in Piecuch et al.[76], I model sea level, $\boldsymbol{\eta}_k = [\eta_{1,k}, \ldots, \eta_{N,k}]^\mathsf{T}$, at steps $k \in \{1, \ldots, K\}$ and locations $n \in \{1, \ldots, N\}$, where K is the total number of time steps and N the total number of target locations, as the sum of a spatially correlated autoregressive process of order 1 and a large-scale spatial field of linear temporal trends,

$$\boldsymbol{\eta}_k - \boldsymbol{b}t_k = r\left(\boldsymbol{\eta}_{k-1} - \boldsymbol{b}t_{k-1}\right) + \boldsymbol{e}_k. \tag{1}$$

In Eq. (1), t_k is the time at step k, r is the lag-1 autocorrelation coefficient, $\boldsymbol{b}$ is the spatial vector of temporal trends, and $\boldsymbol{e}_k$ is an innovation sequence, which can be interpreted as the forcing function driving changes in the autoregressive process (e.g., as in a simple stochastic climate model[84]). Supplementary Table 4 describes all of the model parameters. I set $\sum_{k=1}^{K} t_k = 0$ to represent $\boldsymbol{\eta}_k$ as anomalies from a time mean. The trend vector $\boldsymbol{b}$ is modeled as a random normal field with spatial structure, $\boldsymbol{b} \sim \mathcal{N}\left(\mu \mathbf{1}_N, \Pi\right)$, such that μ is the spatial mean, $\mathbf{1}_X$ is a $X \times 1$ column vector of ones, where X is any positive integer, and,

$$\Pi_{ij} = \pi^2 \exp\left(-\lambda \left|\mathbf{s}_i - \mathbf{s}_j\right|\right). \tag{2}$$

Here π^2 is the partial sill, λ is the inverse range, and $|\mathbf{s}_i - \mathbf{s}_j|$ is distance between target sites $\mathbf{s}_i$ and $\mathbf{s}_j$. The symbol $\sim$ means "is distributed as" and $\mathcal{N}(\boldsymbol{p}, \mathsf{q})$ is the multivariate normal distribution with mean vector $\boldsymbol{p}$ and covariance matrix q.

I model $\boldsymbol{e}_k$ as a temporally independent, identically distributed (iid), but spatially correlated vector with zero mean, $\boldsymbol{e}_k \sim \mathcal{N}(\mathbf{0}_N, \Sigma)$, where $\mathbf{0}_X$ is a $X \times 1$ column vector of zeros, and,

$$\Sigma_{ij} = (\mathsf{c}_{ij})\, \sigma^2 \exp\left(-\phi\, |\mathbf{s}_i - \mathbf{s}_j|\right). \tag{3}$$

Here σ^2 is the partial sill and ϕ is the inverse range. Matrix element $\mathsf{c}_{ij} = 1$ if locations $\mathbf{s}_i$ and $\mathbf{s}_j$ are either both on the southeastern USA or both along the Caribbean, Central America, or South America. Otherwise, $\mathsf{c}_{ij} = 0$. That is, sea level covaries within, but not between, these regions. This spatial covariance structure is motivated by previous analyses of tide-gauge records and satellite-altimetry data. Thompson and Mitchum[85] applied clustering methods to low-pass-filtered tide-gauge records during 1952–2001, finding that the Caribbean Sea (which in their analysis comprised Cuba, Puerto Rico, and Colombia) formed one cluster of coherent sea-level variation, and the southeastern USA (from Florida to North Carolina) formed another cluster. Zhao and Johns[86] determined that Florida Current transports over 1993–2011 were positively correlated with sea-surface height over the Caribbean Sea (including the Bahamas) and along southeastern Central America, but negatively correlated with sea-surface height on the southeastern USA coast on interannual timescales; Domingues et al.[87] showed similar results for seasonal timescales.

Florida Current transport For periods ≥ 1 day, the momentum balance across Florida Straights is nearly geostrophic. Assuming that subsurface pressure signals are vertically coherent[49,50], variations in Florida Current transport should therefore be correlated with changes in the sea-level difference across Florida Straits. Based on this reasoning, I assume that the relationship between annual Florida Current transport, $\boldsymbol{T} = [T_1, \ldots, T_K]^\mathsf{T}$, and coastal sea level, $\eta = [\boldsymbol{\eta}_1, \ldots, \boldsymbol{\eta}_K]$, at times $\boldsymbol{t} = [t_1, \ldots, t_K]^\mathsf{T}$ can be written as,

$$\boldsymbol{T} = \overline{T}\mathbf{1}_K + \rho\eta^\mathsf{T}\boldsymbol{\Delta} + \alpha\boldsymbol{t} + \boldsymbol{w}. \tag{4}$$

Here $\overline{T}$ is the time-mean transport and ρ is a scalar coefficient representing the change in transport per unit change in sea-level difference across Florida Straits. I assume that ρ is constant, and does not vary with time period or frequency band. While it might appear simplistic, this assumption is justified based on analysis of an ocean general circulation model (see below; Supplementary Figures 6, 7). The $N \times 1$ vector $\boldsymbol{\Delta}$ is a differencing operator, such that $\Delta_i = 1$ if site i is Settlement Point (the tide gauge nearest to the eastern end of the submarine cable in the Bahamas), $\Delta_i = -1$ if site i is West Palm Beach (the closest tide gauge to the western end of the cable in southeastern Florida), and zero otherwise. Hence, $\rho\eta^\mathsf{T}\boldsymbol{\Delta}$ is the sea-level difference across Florida Straits converted into units of a transport.

The remaining terms in Eq. (4) account for influences on sea level that are unrelated to the large-scale geostrophic flow. I include $\rho\eta^\mathsf{T}\boldsymbol{\Delta}$ in Eq. (4) based on geostrophic considerations, but this term potentially includes both dynamic and static processes. The scalar α is included in Eq. (4) to correct or offset any static trends in sea level unrelated to ocean circulation that should be subtracted for estimating Florida Current transport (e.g., glacial isostatic adjustment). That is, $\alpha\boldsymbol{t}$

is designed to remove static trends from $\rho\eta^{\mathsf{T}}\boldsymbol{\Delta}$. Thus, with reference to Eqs. (1), (4), $\boldsymbol{b}^{\mathsf{T}}\boldsymbol{\Delta}$ is the total difference in sea-level trends across Florida Straits, whereas $-\alpha/\rho$ is the static component of the sea-level trend difference. So, the dynamic component of the trend in sea-level difference across Florida Straits (total minus static) is $\boldsymbol{b}^{\mathsf{T}}\boldsymbol{\Delta} + \alpha/\rho$. As discussed in the main text, posterior Bayesian model solutions for the dynamic component are consistent with trends in dynamic sea-surface height differences across Florida Straits observed by satellite altimetry, and solutions for the static component agree with rates of static sea-level change due to differential vertical land motion between the Bahamas and Florida observed by GPS, and differences in longterm geological processes as inferred from proxy sea-level index points (Supplementary Figure 5). I also include $\boldsymbol{w} = [w_1, \ldots, w_K]^{\mathsf{T}}$, modeled as iid uncorrelated white noise, $w_k \sim \mathcal{N}(0, \omega^2)$, with variance ω^2, to parameterize the response to local atmospheric or terrestrial forcing, such as variable river runoff, air pressure, or wind stress across Florida Straits.

Data level

Tide-gauge records Following Piecuch et al.[76], I represent annual data from tide gauges, $\boldsymbol{z}_k = [z_{1,k}, \ldots, z_{M_k,k}]^{\mathsf{T}}$, where $M_k \leq N$ is the number of tide gauges with measurements at time step k, as corrupted (incomplete, noisy, biased) versions of the underlying $\boldsymbol{\eta}_k$ process,

$$\boldsymbol{z}_k = \mathsf{H}_k\boldsymbol{\eta}_k + \boldsymbol{d}_k + \mathsf{F}_k\left(\boldsymbol{a}t_k + \boldsymbol{\ell}\right). \tag{5}$$

Here $\boldsymbol{d}_k$ is a random error sequence, which is modeled as a spatially and temporally uncorrelated normal field, $\boldsymbol{d}_k \sim \mathcal{N}(\mathbf{0}_{M_k}, \delta^2\mathsf{I}_{M_k})$, with variance δ^2. A vector of location-specific bias offsets $\boldsymbol{\ell}$ are imposed and represented as a spatially uncorrelated Gaussian field, $\boldsymbol{\ell} \sim \mathcal{N}(\nu\mathbf{1}_M, \tau^2\mathsf{I}_M)$, with

mean ν, variance τ^2. Here M is the total number of tide gauges that make a measurement at any point in time, such that $N \geq M \geq M_k \; \forall k$. Purely local error trends in the data $\boldsymbol{a}$ are also modeled as a random normal field without spatial correlation, $\boldsymbol{a} \sim \mathcal{N}\left(\mathbf{0}_M, \gamma^2 \mathsf{I}_M\right)$, with variance γ^2. Finally, H_k and F_k are selection matrices, filled with zeros and ones, which pick out $\boldsymbol{\eta}_k$, $\boldsymbol{a}$, and $\boldsymbol{\ell}$ values where observations are made at time t_k.

Submarine-cable measurements I assume that L annual data values from the submarine cable, $\boldsymbol{x} = [x_1, \ldots, x_L]^{\mathsf{T}}$, are available and represent imperfect (incomplete and noisy) versions of the underlying $\boldsymbol{T}$ process,

$$\boldsymbol{x} = \mathsf{G}\boldsymbol{T} + \boldsymbol{u}. \tag{6}$$

Here G is a $L \times K$ selection matrix that picks out years when cable data are available, and $\boldsymbol{u} = [u_1, \ldots, u_L]^{\mathsf{T}}$ is a zero-mean random data error sequence, where $u_l \sim \mathcal{N}\left(0, \xi_l^2\right)$ and the ξ_l^2 are set equal to the corresponding submarine-cable data standard error variances mentioned above and computed based on the availability of data in any given year.

Parameter level To close the model, I place priors on the parameters. As in Piecuch et al.[76], I use proper, mostly conjugate forms. Priors and hyperparameters are given in Supplementary Table 5. These choices follow the basic philosophy in Piecuch et al.[76]. I use diffuse, mostly uninformative priors, choosing hyperparameters largely to initialize the Gibbs sampler and Metropolis-Hastings algorithm (see below) in an appropriate neighborhood of parameter space. For example, all variance parameters (e.g., π^2, σ^2, δ^2) are given inverse-gamma priors, with shape ξ and scale χ. In

all cases, I select $\xi = 0.5$ and base χ on the variance of the data. As explained by Tingley and Huybers[88], this choice corresponds to 1 prior observation with a variance of 2χ, which is a weak constraint that has little influence on the posterior.

To quantify the relative importances of the priors and the data, after I compute the posterior solutions (see below), I compare the widths of the 95% credible intervals from the posterior and prior probability distribution functions for each parameter (Supplementary Table 6). If the prior and posterior credible intervals have similar widths, it means that the posterior solutions are largely determined by the prior assumptions. If posterior credible intervals are much narrower than the prior credible intervals, it means that the posterior solutions are mostly constrained by the observations. Almost universally, the 95% posterior credible intervals are much narrower than the 95% prior credible intervals (Supplementary Table 6). This implies that posterior inference is drawn predominantly from the information content of the observations, and not overly influenced by prior beliefs encoded into the model.

Drawing samples from the posterior distribution Given the model equations, I use Bayes' rule, and assume that the posterior probability distribution function takes the form,

$$
\begin{aligned}
p\left(\eta, \boldsymbol{T}, \Theta | \mathbf{Z}, \boldsymbol{x}\right) &\propto p\left(\mathbf{Z}, \boldsymbol{x} | \eta, \boldsymbol{T}, \Theta\right) \times p\left(\eta, \boldsymbol{T} | \Theta\right) \times p\left(\Theta\right) \\
&= p\left(\boldsymbol{\eta}_0\right) \times p\left(\overline{T}\right) \times p\left(r\right) \times p\left(\sigma^2\right) \times p\left(\phi\right) \times p\left(\mu\right) \times p\left(\pi^2\right) \\
&\times p\left(\lambda\right) \times p\left(\delta^2\right) \times p\left(\nu\right) \times p\left(\tau^2\right) \times p\left(\gamma^2\right) \times p\left(\rho\right) \times p\left(\alpha\right) \\
&\times p\left(\omega^2\right) \times p\left(\boldsymbol{b} | \mu, \pi^2, \lambda\right) \times p\left(\boldsymbol{\ell} | \nu, \tau^2\right) \times p\left(\boldsymbol{a} | \gamma^2\right) \times p\left(\boldsymbol{x} | \boldsymbol{T}\right) \\
&\times p\left(\boldsymbol{T} | \eta, \rho, \alpha, \omega^2, \overline{T}\right) \times \prod_{k=1}^{K} \left[p\left(\boldsymbol{z}_k | \boldsymbol{\eta}_k, \boldsymbol{a}, \boldsymbol{\ell}, \delta^2\right) \times p\left(\boldsymbol{\eta}_k | \boldsymbol{\eta}_{k-1}, \boldsymbol{b}, r, \sigma^2, \phi\right)\right]
\end{aligned}
\tag{7}
$$

In Eq. (7), $\mathbf{Z}$ is the structure of all tide-gauge data points, p is used to represent probability distribution function, $|$ is conditionality, $\propto$ is proportionality, and $\Theta \doteq \{r, \sigma^2, \phi, \dots\}$ is used to represent the set of all model parameters. I assume that the observations are conditionally independent, provided the process and parameters.

Draws from the posterior probability distribution function are made as in Piecuch et al.[76]. I use Markov chain Monte Carlo (MCMC) methods, evaluating the full conditional distributions for process and parameter values using a Gibbs sampler, but using Metropolis-Hastings steps for the inverse range parameters, which have non-standard full conditionals. I run 200,000 MCMC iterations, setting initial process values to zero, and drawing initial parameter values randomly from the respective prior distribution. To remove initialization transients, I discard the first 100,000 iterations as burn in. Then I keep only 1 out of every 100 of the remaining 100,000 iterations to reduce serial correlation effects between draws. Results shown here are based on a 3,000-element chain produced by performing the above procedure 3 times and stitching together the resulting

1,000-member chains. Solutions for scalar parameters are summarized in Supplementary Table 6. To evaluate convergence of the solution, I compute the convergence monitor $\hat{R}$ of Gelman and Rubin[89], which compares the variance within and between the 3 different 1,000-member solutions. In all cases, $\hat{R} \sim 1.00$ (Supplementary Table 6), indicating that the solutions have converged.

Local and global uncertainty measures

The fully probabilistic nature of the posterior solutions allows both pointwise and pathwise uncertainty measures[90] to be calculated. Pointwise statistics measure probabilities locally. The light blue shading in Figure 2 represents the 95% pointwise posterior credible intervals computed from the transport solutions at each year of the reconstruction. The interpretation is that, for each year, there is a 95% chance that the true transport value falls within this blue shading.

Pathwise statistics measure probabilities more globally. The dashed blue lines in Figure 2 represent the 95% pathwise posterior credible intervals calculated from the transport estimates across all years of the reconstruction. These values are computed by widening the 95% pointwise posterior credible intervals until 95% of modeled transport time series are captured in their entirety. That is, there is a 95% chance that the full time series of transport does not ever stray outside the bounds of these pathwise credible intervals.

Other examples of pathwise statistics include values quoted in the text for the minimum and maximum decadal-average transports and the corresponding histograms of their timing shown Figure 4. For each of the 3,000 ensemble members comprising the posterior solution, I smooth

the transport time series using an 11-point boxcar window, and then identify the minimum and maximum transport values along with the times at which they occurred. These values vary from one ensemble member to the next, and so performing this procedure for each ensemble member allows me to populate histograms for the transport extrema and their occurrence times.

Hypothesis testing

In addition to generating posterior solutions for transport and sea level, the Bayesian model provides data-constrained estimates of the various model parameters (e.g., Supplementary Table 6). This allows for rigorous hypothesis testing through simulation experiments. For example, in Figure 3, I show the change in decadal-average Florida Current transport between all possible pairs of non-overlapping decades, and indicate the probability that such changes would have occurred from stationary red-noise process with the same autocorrelation and variance characteristics. As a specific instance, I state that decadally averaged transport declined by -1.4 ± 1.6 Sv from 1960–1970 to the present, and that this decline is very likely (probability $P = 0.90$) more than would be expected from stationary red noise. This conclusion is determined as follows. First, I use the posterior transport solutions to compute a histogram of transport averaged over 2008–2018 minus the transport averaged over 1960–1970. Next, I use the posterior solutions for the scalar model parameters as the basis for the simulation of a parallel set of 3,000 synthetic transport time series following Eqs. (1) and (4), but with the trends ($\boldsymbol{b}$ and α) set to zero. Then, I populate histograms of the difference between decadally averaged synthetic transport between 1960–1970 and 2008–2018. Finally, I compute what fraction of the original posterior transport solutions shows more of

878 a decline than is shown by the stationary synthetic transport process, which, in this example case,
879 is 0.90.

880 **Residual analysis**

881 Various residual terms appear in the Bayesian model equations (see above). When building the
882 model, I made certain assumptions regarding the spatial and temporal structures of these residuals.
883 To test whether these assumptions are appropriate given the data, I perform a residual analysis,
884 using the posterior solutions and model equations to solve for the sea-level innovations $\boldsymbol{e}_k$, tide-
885 gauge errors $\boldsymbol{d}_k$, transport innovations w_k, cable-data errors $\boldsymbol{u}$, tide-gauge error trends $\boldsymbol{a}$ and tide-
886 gauge data bias $\boldsymbol{\ell}$.

887 I assumed that $\boldsymbol{e}_k$, $\boldsymbol{d}_k$, w_k, and $\boldsymbol{u}$ behave as iid temporal white noise. If this assumption is
888 reasonable, then posterior solutions should look random in time. However, if systematic temporal
889 structure is observed, it means that this assumption is inappropriate, and that the model is mis-
890 specified given the data. Time series of posterior $\boldsymbol{e}_k$ and $\boldsymbol{d}_k$ solutions are shown in Supplementary
891 Figure 15a, 15b for an arbitrary (randomly chosen) target location, while model solutions for w_k
892 and $\boldsymbol{u}$ are shown in Supplementary Figure 15c, 15d. The time series look random in time, and
893 there are no obvious signs of autocorrelation. The amplitudes of $\boldsymbol{e}_k$, $\boldsymbol{d}_k$, and w_k variations are
894 consistent with posterior solutions for the respective variance or partial sill parameters σ^2, δ^2, and
895 ω^2 (Supplementary Table 6), and the magnitude of fluctuations in $\boldsymbol{u}$ is in keeping with the prior
896 error variances placed on the submarine-cable data.

To be more thorough, I compute sample autocorrelation coefficients directly from the posterior solutions for $\boldsymbol{e}_k$, $\boldsymbol{d}_k$, w_k, and $\boldsymbol{u}$ across all space and time points. I compare those values to the autocorrelation coefficients expected theoretically for temporal white noise, given the same number of time steps. Supplementary Figure 16 compares the empirical and theoretical autocorrelation coefficients for time lags between 1 and 20 y. Values calculated empirically from the posterior solutions are consistent with the theoretically expected values. More quantitatively, 96%, 95%, 93%, and 95% of empirical autocorrelation coefficients computed respectively from $\boldsymbol{e}_k$, $\boldsymbol{d}_k$, w_k, and $\boldsymbol{u}$ are captured by the theoretical 95% confidence intervals.

In addition to being random in time, $\boldsymbol{e}_k$ and $\boldsymbol{d}_k$ are supposed to have spatially invariant amplitudes. In Supplementary Figure 17, I map median estimates of standard deviations computed empirically from the posterior model solutions of $\boldsymbol{e}_k$ and $\boldsymbol{d}_k$ at each tide-gauge location. While there is some higher-order spatial variation, these values are to lowest order fairly uniform and constant in space, and very similar to the posterior estimates of the partial sill σ^2 and variance parameter δ^2 (Supplementary Table 6).

Motivated by past studies[85–87], I assume that $\boldsymbol{e}_k$ is spatially structured, such that there is covariance between sites along the Caribbean, Central America, and South America, and between sites on the southeastern USA, but no covariance between these two broad regions. These assumptions are reflected in the block structure of the theoretical covariance matrix Σ shown in Supplementary Figure 18b computed from the posterior median solution for the partial sill σ^2 (Supplementary Table 6). This theoretical covariance matrix is very similar to the covariance ma-

trix determined empirically by comparing all pairs of posterior solutions for $\boldsymbol{e}_k$ (Supplementary Figure 18a). Indeed, the Pearson correlation coefficient between the two matrices in Supplementary Figure 18 is 0.91, and the theoretical covariance matrix explains 82% of the variance in the empirical covariance matrix.

In Supplementary Figure 19a, I show a map of median values of Pearson correlation coefficients computed between posterior solutions for the Florida Current transport and sea level at every coastal location after removing linear trends from the time series. Correlation coefficients are positive over the Caribbean, Central America, and South America, and negative along the southeastern USA. The magnitude of the correlation decreases with increasing distance of the sea-level location from the Florida Straits. This behavior of the empirically determined correlation coefficients is broadly consistent with the correlation pattern expected theoretically (Supplementary Figure 19b), given Eqs. (3) and (4) and posterior solutions for the model parameters (Supplementary Table 6).

Finally, I consider residual spatial fields of the tide-gauge data biases $\boldsymbol{\ell} - \nu\mathbf{1}$ and error trends $\boldsymbol{a}$. According to data-level Eq. (5) for the tide gauges, these two vectors should have zero mean, no spatial correlation, and spatial variances of τ^2 and γ^2, respectively. Supplementary Figure 20 facilitates an assessment of these assumptions, showing both posterior solutions for $\boldsymbol{\ell} - \nu\mathbf{1}$ and $\boldsymbol{a}$ alongside the solutions expected for a zero-mean random process given the posterior solutions for τ^2 and γ^2 (Supplementary Table 6). Consistent with model assumptions, these vector fields look fairly random, scattered about zero. The spatial spread in $\boldsymbol{\ell} - \nu\mathbf{1}$ and $\boldsymbol{a}$ appears consistent with the posterior τ^2 and γ^2 solutions. Indeed, 95% of the posterior $\boldsymbol{\ell} - \nu\mathbf{1}$ solutions are captured by the 95%

credible intervals predicted for a zero-mean, spatially uncorrelated Gaussian process with variance τ^2, and similarly 95% of posterior solutions for $\boldsymbol{a}$ fall within the 95% credible interval produced by simulating a zero-mean random normal field with variance γ^2 (Supplementary Figure 20).

In conclusion, the design of my Bayesian algorithm is supported by residual analysis, which demonstrates that the model structure is appropriate and warranted given the available data.

Sensitivity of model solutions to input data

Posterior solutions for Florida Current transports in the main text are based on the assimilation of submarine cable data over 1982–2018 with standard errors of 0.30–0.35 Sv (see above). To quantify how robust or sensitive the solutions are to the duration of the data and the selected standard errors, I perform two additional data assimilation experiments. In the first experiment, I double the standard errors on the cable data given to the Bayesian algorithm during 1982–2018. I refer to this first experiment as the "double-error" experiment. For clarity, in this section, I call the Bayesian model solution from the main text the "baseline" experiment. In the second sensitivity experiment, I maintain the original standard errors, and I give the Bayesian algorithm all of the cable measurements for the period 2000–2018, but I withhold all data during 1982–1998. Due to an outage in the observing system, no data are available for 1999. I call this second experiment the "half-data" experiment.

Salient features of the sensitivity experiments are summarized alongside the baseline experiment in Supplementary Figure 21. Baseline and double-error solutions are, in many respects, very

similar. For example, Florida Current transport during 1909–1981, transport trend over 1909–2018, and regression coefficient between transport and sea-level difference across the Florida Straits from these two experiments are nearly the same (cf. blue and orange in Supplementary Figure 21). One difference is that widths of the posterior 95% credible intervals on the transport during 1982–2018 (i.e., the period when transport observations are available) are about twice as large in the double-error experiment compared to the baseline experiment (Supplementary Figure 21a). This is consistent with the larger standard errors placed on the data in the former experiment. In sum, I conclude that model solutions are generally quantitatively insensitive to reasonable alternative specifications of the standard error on the cable transport measurements.

Solutions from the half-data experiment (yellow in Supplementary Figure 21) show similarities to the other two solutions, but can show larger uncertainty. This is unsurprising, since the half-data experiment has fewer data constraints. For example, whereas the posterior 95% credible intervals on the 110-y transport trend are -1.7 ± 3.7 and -1.6 ± 3.9 Sv century^{-1} in the baseline and double-error experiments, in the half-data experiment it is -2.3 ± 6.9 Sv century^{-1}. The fact that uncertainties from the double-error experiment are smaller than from the half-data experiment suggests that having more data with larger errors is more informative for constraining the transport history than having fewer data that have smaller errors. Importantly, although the trend from the half-data experiment is more uncertain in an absolute sense, the sign of the trend is similarly determined in all three experiments. I find that 82%, 80%, and 77% of trend solutions in the baseline, double-error, and half-data experiments are negative, respectively (Supplementary Figure 21b). That is, all three experiments suggest that Florida Current transport probably declined

over the past century. Thus, I reason that the main findings in this study are qualitatively robust to reasonable alternative choices for the duration of the transport data assimilated into the Bayesian algorithm.

Synthetic data experiments

In the half-data experiment, $\sim 90\%$ of the withheld Florida Current transport values during 1982–1998 fall within the pointwise posterior 95% credible intervals on the transport. This suggests that the uncertainties estimated by the Bayesian algorithm are reasonable. To more thoroughly evaluate the meaningfulness of the posterior solutions from the Bayesian algorithm, I perform a number of synthetic data experiments. In these experiments, I take a set of known processes and corrupt them to look like the observations, and then apply the model to the corrupted process values. By comparing the posterior solutions to the known but withheld values, I quantify the accuracy and precision of the error bars estimated by the model (e.g., are $\sim 95\%$ of the true values actually captured by the posterior 95% credible intervals?).

First experiment—perfect model I run a perfect model experiment. I choose, from the ensemble of posterior model solutions presented in the main text, the array of scalar parameter solutions $\left(\overline{T}, r, \sigma^2, \dots\right)$ from the ensemble member that minimizes the Mahalanobis distance to the mean parameter array. Using these scalar parameter values, I simulate synthetic versions of the sea-level and transport processes based on the process-level equations. Using the data-level equations, I generate synthetic tide-gauge and submarine-cable data by adding noise, bias, and gaps to the

simulated processes, as in the real world, and I apply the Bayesian model to these synthetic data.

Results are summarized in Supplementary Table 7 and Supplementary Figure 22. For 13 out of the 14 scalar parameters, or $\sim 93\%$, the true value is captured by the corresponding 95% posterior credible interval from the model (Supplementary Table 7). Considering vector fields, I find that 100%, 98%, and 100% of the true values for regional sea-level trends $\boldsymbol{b}$, tide-gauge biases $\boldsymbol{\ell}$, and tide-gauge error trends $\boldsymbol{a}$, respectively, fall within the corresponding pointwise posterior 95% credible intervals (not shown). In terms of the processes, 98% of the true sea-level values and 99% of true transport values fall within the estimated pointwise 95% credible intervals, and the true transport time series is entirely encompassed by the pathwise 95% posterior credible intervals (e.g., Supplementary Figure 22). Together, these results show that the model performs well, and that the posterior credible intervals are meaningful, albeit slightly conservative, roughly capturing the correct fraction of true process and parameter values.

Second experiment—more realistic case The first synthetic data experiment is informative, showing that the processes and parameters are identifiable given incomplete, noisy, biased data. It is also potentially idealistic, since the model is perfectly specified. The equations governing the spatiotemporal evolution of the processes, and the relationship between the observations and the processes were known perfectly, and the task was to infer the uncertain values of the processes and parameters appearing in those equations. While residual analysis suggests that they are appropriate given the data, the model equations probably represent a simplification of the complex, myriad oceanographic and geophysical processes contributing to changes in sea level and transport, and

their correspondence to observations in the real world. While some degree of model misspecification is inevitable, the salient question is whether the model is robust to misspecification and still provides meaningful posterior estimates.

So, I perform a second synthetic data experiment. Rather than use the process equations to simulate sea level and transport, I bring together output from more complex physical models. I begin with ocean dynamics. I take 110 y of monthly Florida Current transport near $27°$N, and sea level from each of the model grid cells nearest to the 46 tide gauges from version 2.2.4 of the Simple Ocean Data Assimilation (SODA) product[52]. This version of SODA represents a solution to an ocean general circulation model forced at the surface by an atmospheric reanalysis over the period 1871–2010 (I use the past 110 y of output covering from 1901 to 2010). The model has moderate spatial resolution, with 40 vertical levels and a native $0.25° \times 0.40°$ horizontal grid in longitude and latitude. A version of the solution, which was interpolated onto a regular $0.5° \times 0.5°$ horizontal grid, was downloaded from the Asia-Pacific Data-Research Center (APDRC) of the University of Hawai'i School of Ocean and Earth Science and Technology. After downloading, I removed the monthly time series of global-mean sea level and computed annual means from the resulting monthly sea-level values.

The SODA solution represents a tradeoff between spatial resolution and temporal coverage. Coupled climate models are available that cover comparable or longer time periods[91], but most publicly available solutions have coarser horizontal resolution (nominally $\sim 1°$ in longitude and latitude), and may not faithfully represent the Florida Current and coastal sea level. While

much higher-resolution ocean models are available[92] that more accurately portray the complexity of Florida Current transport and coastal sea level, these model runs are typically short, and do not span the centennial timescales of primary interest here. Thus, while it has its deficiencies (see below), SODA is perhaps one of the best-suited ocean models for my purposes. For example, Chepurin et al.[93] show that version 2.2.4 of SODA simulates interannual-to-decadal variations in coastal sea level along the eastern USA and parts of the Caribbean, Central America, and South America reasonably well over 1950–2011.

I superimpose static sea-level effects on the dynamic sea-level fields from SODA. I add a yearly time series of global-mean sea level due to ocean warming and thermal expansion over 1901–2010 from the Version 4 of the Community Climate System Model[94] (downloaded from the Woods Hole Oceanographic Institution's Community Storage Server). I also include, at each tide-gauge location, an estimate of the trend in relative sea level due to the combined effects of ongoing glacial isostatic adjustment from Peltier et al.[95] (downloaded from the PSMSL) along with twentieth-century melting of mountain glaciers and ice sheets due to Hamlington et al.[96] (courtesy of S. Adhikari, Jet Propulsion Laboratory). Finally, I add time series of a temporally random but spatially correlated process with zero mean and temporal variance of $\sim (1\ \mathrm{cm})^2$ to simulate sea-level changes due to the inverted barometer effect linked with the North Atlantic Oscillation[97].

I apply the data-level equations to the transport and sea-level values, incorporating noise and bias, and imparting data gaps so that the synthetic tide-gauge and submarine-cable data are only available when and where the true observations are available. The synthetic datasets are

subsequently fed into the Bayesian algorithm. The results of this second synthetic data experiment are summarized in Supplementary Table 8 and Supplementary Figure 23. In this case, only four scalar parameters (those appearing in the data-level equations) are known perfectly. For three out of these four parameters, or 75%, the true value is captured by the 95% posterior credible intervals from the model (Supplementary Table 8). For one parameter, δ^2, the tide-gauge data error variance, the Bayesian model slightly underestimates the true value. Considering the process time series, I find that 81% of the true transport values and 95% of the true sea-level values are captured by the pointwise 95% posterior credible intervals produced by the Bayesian model, and that, as in the previous experiment, the full time series of the true transport is totally captured by the pathwise 95% posterior credible interval (Supplementary Figure 23).

It is worth noting that the posterior solution for α, the apparent trend in the transport process Eq. (4), suggests that sea level at Settlement Point on Grand Bahama must have risen 0.2 ± 1.6 mm y^{-1} faster than at West Palm Beach near West Palm Beach due to processes unrelated to ocean dynamics. Although uncertain, this is consistent with the trend difference of ~ 0.1 mm y^{-1} I imposed between these two sites based on model estimates of GIA and contemporary ice melt[95,96], demonstrating that the model succeeds in separating static and dynamic sea-level trends.

Recall that my Bayesian model assumes that the transfer coefficient ρ between sea level and transport is a fixed constant. To test this assumption, I consider in more detail time series of Florida Current transport and sea-level difference across Florida Straits from SODA. Transport and sea-level difference are highly correlated with one another (Pearson correlation coefficient of ~ 0.9),

and a linear regression suggests that transport increases by ~ 0.9 Sv for every 1-cm increase in sea level difference (Supplementary Figure 7), consistent with a visual inspection of the two time series (Supplementary Figure 6a). To study the correspondence as a function of frequency band, I apply admittance and coherence analysis[53] to the model output. Transport and sea-level difference are significantly coherent at all accessible periods from 2- to 32-y (Supplementary Figure 6b), in agreement with basic expectations from geostrophy. Moreover, the transfer function (using sea-level difference as the input and transport as the output) is qualitatively insensitive to frequency band, with similar values found at interannual and multidecadal timescales (Supplementary Figure 6c). Importantly, the Bayesian model posterior estimate for the transfer coefficient ρ is consistent with SODA and overlaps the values obtained from the admittance analysis (Supplementary Figures 6, 7). This suggests that it is reasonable to assume that there is a constant transfer coefficient between sea-level difference and transport on the timescales of this study, and also that the Bayesian model successfully infers the correct transfer-coefficient value.

Note that Florida Current transport from SODA is suspicious (Supplementary Figure 23c). The mean transport is ~ 51 Sv, growing from ~ 42 Sv at the beginning of the period to ~ 56 Sv at the end. This value is $\sim 60\%$ larger than the average value observed by submarine cable since 1982, and ~ 10 Sv larger than the largest annual transport value inferred at any time in the original Bayesian model solution discussed in the main text. The striking increase of ~ 14 Sv over the 110-y run seems extreme in light of the more subtle trend estimates produced by the original Bayesian model solution (cf. Figure 2; Supplementary Figure 23c). Although it is imperfect, in that it does not realistically represent the true evolution of the Florida Current over the past century, SODA

is nevertheless informative in the present context. For establishing the ability of the Bayesian algorithm to infer the parameters and processes from imperfect data, I do not require that SODA reproduces observed reality, but rather that it portrays a physically plausible scenario, and that the basic "statistics" (e.g., spatiotemporal covariance structure, relationship between state variables, etc.) are believable.

In sum, I conclude that, even in a more complex setting, my Bayesian model performs reasonably well, giving uncertainty estimates that roughly capture the correct fraction of true values.

83. Hughes, C. W., and M. P. Meredith. Coherent sea-level fluctuations along the global continental slope, *Phil. Trans. R. Soc. A.*, **364**, 885–901 (2006).

84. Frankignoul, C., and K. Hasselmann. Stochastic climate models, part II: application to sea-surface temperature anomalies and thermocline variability, *Tellus*, **29**, 289–305 (1977).

85. Thompson, P. R., and G. T. Mitchum. Coherent sea level variability on the North Atlantic western boundary, *J. Geophys. Res. Oceans*, **119**, 5676–5689, doi:10.1002/2014JC009999 (2014).

86. Zhao, J., and W. Johns. Wind-forced interannual variability of the Atlantic meridional overturning circulation at $26.5°$N, *J. Geophys. Res.-Oceans*, **119**, 2403–2419.

87. Domingues, R., M. Baringer, and G. Goni. Remote sources for year-to-year changes in the seasonality of the Florida Current transport, *J. Geophys. Res.-Oceans*, **121**, 7547–7559.

88. Tingley, M. P., & P. Huybers. A Bayesian algorithm for reconstructing climate anomalies in space and time. Part I: development and application to paleoclimate reconstruction problems, *J. Clim.*, **23**, 2759–2781 (2010).

89. Gelman, A., and D. B. Rubin. Inference from iterative simulation using multiple sequences, *Stat. Sci.*, **7**, 457–472 (1992).

90. Tingley, M. P., & P. Huybers. Recent temperature extremes at high northern latitudes unprecedented in the past 600 years, *Nature*, **496**, 201–205 (2013).

91. Taylor, K. E., et al. An Overview of CMIP5 and the Experimental Design, *B. Am. Meteorol. Soc.*, **93**, 485–498 (2012).

92. Gula, J., M. J. Molemaker, and J. C. McWilliams. Topographic generation of submesoscale centrifugal instability and energy dissipation, *Nat. Commun.*, **7**, 12811 (2016).

93. Chepurin, G. A., J. A. Carton, and E. Leuliette. Sea level in ocean reanalyses and tide gauges, *J. Geophys. Res.-Oceans*, **119**, 147–155 (2014).

94. Gent, P. R., et al. The Community Climate System Model Version 4 , *J. Clim.*, **24**, 4973–4991 (2011).

95. Peltier, W. R., et al. Space geodesy constrains ice age terminal deglaciation: The global ICE-6G_C (VM5a) model, *J. Geophys. Res.-Solid Earth*, **120**, 450–487 (2015).

96. Hamlington, B. D., et al. Observation-Driven Estimation of the Spatial Variability of 20th Century Sea Level Rise, *J. Geophys. Res.-Oceans*, **123**, 2129–2140 (2018).

97. Piecuch, C. G., and R. M. Ponte. Inverted barometer contributions to recent sea level changes along the northeast coast of North America, *Geophys. Res. Lett.*, **42**, 5918–5925 (2015).

Supplementary Information for "Likely weakening of the Florida Current during the past century revealed by sea-level observations"

Christopher G. Piecuch[1]

[1] *Woods Hole Oceanographic Institution, Woods Hole, Massachusetts, USA*

S1 A note on symbols and notation in this document

In the Methods section, where I develop the Bayesian algorithm, I exhaust most of the letters in the Roman and Greek alphabets. In what follows here, I present more equations, which are informative for interpreting results in the main text. To avoid making these equations cumbersome, I must reuse some of the letters from Methods, but for different purposes. To reduce confusion, I have structured the text of this section and the Methods so that there is no crossover in symbol meaning between the text in the two documents; that is, symbols and letters as defined in the text here are not referred to as such in Methods, and vice versa. The one unavoidable exception is the Supplementary Tables below, some of which (Supplementary Tables 4–8) reference the symbols and letters defined in Methods, and the supplementary figure captions.

S2 Using the method of surrogate data to evaluate uncertainty on linear trends computed in ancillary datasets accounting for autocorrelation of residuals

At different points in the text, I quote trends computed from ancillary time series not incorporated into the Bayesian model, namely wind-stress curl, sea-surface temperature, and sea-surface height. In these cases, I give the best estimate of the trend followed by a $\pm$ value that represents twice the estimated standard error. Here I describe how the standard errors are estimated.

Typically, when estimating a trend from ordinary least squares, one assumes that residuals are independent and identically distributed (iid) and errors are uncorrelated (e.g., white noise). Yet, many geophysical time series do not behave as white-noise processes, but rather exhibit temporal autocorrelation[1,2], which is sometimes called long-range dependence or persistence or memory[3–5]. If autocorrelation is not taken into account, then standard errors on trends will be underestimated.

To account for autocorrelation of the residuals, I use the method of surrogate data[6]. Given a data time series $x(t)$, I compute the best estimate of the trend through the data using ordinary least squares. I then remove the trend from the data, leaving the residual series $x'(t)$. Next, I randomly generate a large number (e.g., 10^3) of synthetic time series $\left\{\tilde{x'}_i(t)\right\}$ based on $x'(t)$, such that each $\tilde{x'}_i(t)$ has the same Fourier amplitudes as $x'(t)$ but randomized (scrambled) phase. I compute linear trends in each $\tilde{x'}_i(t)$, resulting in a histogram of the possible apparent trends, or stochastic trends, in a random stationary process with the same basic timescales and amplitudes of variation and the same effective degrees of freedom as the original data series. I take the standard deviation of all of the $\tilde{x'}_i(t)$ trends as the estimated standard error on the original $x(t)$ trend.

S3 Simulating the hypothetical transport of the Antilles Current

The question arose in the text as to whether the probable weakening of the Florida Current transport over the past century is partly balanced by compensating changes in the Antilles Current transport. Direct measurements of the Antilles Current are short and do not allow for a direct observational assessment. However, it is possible to estimate a range of possible stochastic (or random) transport trends, given the time-series properties of the available data.

Meinen et al.[7] report, based on ~ 11 y of daily data (2005–2015), that the Antilles Current transport has a standard deviation of 7.5 Sv and an integral timescale of 19.0 days (cf. their Table 3). Following Emery and Thomson[8], the integral timescale τ of a discrete time series is defined as,

$$\tau = 2\Delta t \sum_{k=0}^{+\infty} C_k, \tag{S1}$$

where $C_k = C\left(k\Delta t\right)$ is the autocorrelation function of the time series with itself at lag $k\Delta t$ for a time increment Δt. These statistics form the basis of simple simulation experiments of the Antilles Current transport.

I assume that Antilles Current transport behaves as random stationary red noise that can be modeled as an autoregressive process of order 1,

$$y_k = \varphi y_{k-1} + \varepsilon_k. \tag{S2}$$

Here y_k is Antilles Current transport at time step k, φ is the lag-1 autocorrelation coefficient, and $\varepsilon_k \sim \mathcal{N}\left(0, \sigma^2\right)$ is stationary white noise with zero mean and variance σ^2. To simulate this process, values for φ and σ^2 must be assigned based on the Antilles Current transport observations.

Based on the properties of an autoregressive processes, the autocorrelation of y_k is $C_k = \varphi^k$. Using this form of C_k in Eq. $(S1)$ and evaluating the sum of the geometric series gives,

$$\tau = \frac{2\Delta t}{1-\varphi}. \tag{S3}$$

Rearranging to solve for φ, and using $\tau = 19.0$ days and $\Delta t = 1$ day from Meinen et al.[7], gives,

$$\varphi = 1 - \frac{2\Delta t}{\tau} = 0.9. \tag{S4}$$

The variance of y_k is $\mathrm{var}\,(y_k) = \sigma^2 \big/ (1-\varphi^2)$. Rearranging to solve for σ^2, setting $\varphi = 0.9$ based on Eq. $(S4)$, and using $\mathrm{var}\,(y_k) = (7.5\ \mathrm{Sv})^2$ from Meinen et al.[7] gives,

$$\sigma^2 = \left(1-\varphi^2\right) \mathrm{var}\,(y_k) = (3.3\ \mathrm{Sv})^2\,. \tag{S5}$$

Using these values for φ and σ^2, I run simulation experiments to quantify the possible range of stochastic trends in Antilles Current transport as a function of timescale. For time-series lengths between 1 and 150 y, I generate random values for ε_k in Eq. $(S2)$ to yield 1,000 separate synthetic daily series of surrogate Antilles Current transport. I compute the linear trend in each of these 1,000 surrogate time series for each specified time-series length. This allows me to populate a histogram of the trends possible for a stationary random red-noise process with the same variance and integral timescale as the Antilles Current transport data. Shading in Supplementary Figure 11 represents the 95% confidence interval (2.5th and 97.5th percentiles) from these simulations as a function of timescale, which are ± 2.9 and ± 1.2 Sv century^{-1} for periods of 50- and 100-y, respectively.

S4 Computing the trend in surface heat flux implied by a trend in sea-surface temperature

What follows in this section is based on the forms of air-sea fluxes described by Large and Yeager[9] (their section 2.1). Most symbols used in this section are theirs.

I start by establishing basic definitions, after Large and Yeager[9]. The total air-sea heat flux Q_{as} (positive into the ocean) is given by a sum of contributions,

$$Q_{as} = Q_S + Q_L + Q_E + Q_H, \tag{S6}$$

where Q_S is shortwave solar radiation,

$$Q_S = Q_I \left(1 - \alpha\right), \tag{S7}$$

where Q_I is the insolation and α is the surface albedo; Q_L is the net longwave flux,

$$Q_L = Q_A - \sigma \left(\mathrm{SST}\right)^4, \tag{S8}$$

where Q_A is the longwave energy received from the atmosphere, SST is sea-surface temperature, and $\sigma = 5.67 \times 10^{-8}$ W m^{-2} K^{-4} is the Stefan-Boltzmann constant; Q_E is the latent turbulent flux,

$$Q_E = \Lambda_v \rho_a C_E \left[q\left(z_q\right) - q_{sat}\left(\mathrm{SST}\right)\right] \left|\Delta\vec{U}\right|, \tag{S9}$$

where $\Lambda_v = 2.5 \times 10^6$ J kg^{-1} is the latent heat of vaporization, $\rho_a = 1.22$ kg m^{-3} is air density near the surface, $q\left(z_q\right)$ is the specific humidity of air at a height z_q above the surface, C_E is the transfer coefficient for evaporation, q_{sat} is the specific humidity of air at saturation, and $\left|\Delta\vec{U}\right|$ is the near-surface wind speed; and Q_H is the sensible turbulent flux,

$$Q_H = \rho_a c_p C_H \left[\theta\left(z_\theta\right) - \mathrm{SST}\right] \left|\Delta\vec{U}\right|, \tag{S10}$$

where $c_p = 1000.5$ J kg^{-1} K^{-1} is the specific heat of air, C_H is the transfer coefficient of sensible heat, and $\theta\,(z_\theta)$ is air temperature at a height z_θ above the surface. Note that I ignore heat flux due to precipitation, since its contribution is often small and uncertain.

The transfer coefficients of latent and sensible heat are functions of the drag coefficient C_D,

$$C_E = \frac{34.6}{1000}\sqrt{C_D}, \tag{S11}$$

and

$$C_H = \frac{18.0}{1000}\sqrt{C_D}, \tag{S12}$$

with

$$C_D = \frac{2.70\ \mathrm{m\ s^{-1}}}{U_N\,(10\ \mathrm{m})} + 0.142 + \frac{U_N\,(10\ \mathrm{m})}{13.09\ \mathrm{m\ s^{-1}}}, \tag{S13}$$

where $U_N\,(10\ \mathrm{m})$ is variable wind speed at 10 m under neutral stability. Note that I assume stability in defining C_H in Eq. $(S12)$; see Large and Yeager[9] for more details on forms of C_H.

The specific humidity at saturation q_{sat} is a function of SST,

$$q_{sat}\,(q_1, q_2, \mathrm{SST}) = \frac{q_1}{\rho_a}\exp\left(\frac{q_2}{\mathrm{SST}}\right), \tag{S14}$$

where $q_1 = 0.98 \times 640380$ kg m^{-3} and $q_2 = -5107.4$ K are the coefficients.

All of the above is as in Large and Yeager[9]. I now use these forms to consider an infinitesimal perturbation $d\mathrm{SST}$ in sea-surface temperature. The resulting perturbation dQ_{as} in surface heat flux is exactly,

$$dQ_{as} = \frac{\partial Q_{as}}{\partial \mathrm{SST}}\Big|_{\overline{\mathrm{SST}}} d\mathrm{SST} = \left(\frac{\partial Q_L}{\partial \mathrm{SST}}\Big|_{\overline{\mathrm{SST}}} + \frac{\partial Q_E}{\partial \mathrm{SST}}\Big|_{\overline{\mathrm{SST}}} + \frac{\partial Q_H}{\partial \mathrm{SST}}\Big|_{\overline{\mathrm{SST}}}\right) d\mathrm{SST}, \tag{S15}$$

where $\big|_{\overline{\mathrm{SST}}}$ indicates that values are evaluated at the background average SST value. Contributions from Q_S fall away because they have no explicit dependence on SST. The partial derivatives on the right-hand side of Eq. $(S15)$ are,

$$\frac{\partial Q_L}{\partial \mathrm{SST}}\Big|_{\overline{\mathrm{SST}}} = -4\sigma \left(\overline{\mathrm{SST}}\right)^3, \tag{S16}$$

$$\frac{\partial Q_E}{\partial \mathrm{SST}}\Big|_{\overline{\mathrm{SST}}} = \Lambda_v \rho_a C_E \big|\Delta\vec{U}\big| \frac{q_2}{\overline{\mathrm{SST}}^2} q_{sat}\left(\overline{\mathrm{SST}}\right), \tag{S17}$$

and

$$\frac{\partial Q_H}{\partial \mathrm{SST}}\Big|_{\overline{\mathrm{SST}}} = -\rho_a c_p C_H \big|\Delta\vec{U}\big|, \tag{S18}$$

whence,

$$dQ_{as} = \underbrace{\left[\Lambda_v \rho_a C_E \big|\Delta\vec{U}\big| \frac{q_2}{\overline{\mathrm{SST}}^2} q_{sat}\left(\overline{\mathrm{SST}}\right) - 4\sigma\left(\overline{\mathrm{SST}}\right)^3 - \rho_a c_p C_H \big|\Delta\vec{U}\big|\right]}_{\Gamma} d\mathrm{SST}. \tag{S19}$$

For a finite but small, linear SST perturbation, Eq. $(S19)$ will hold approximately. Therefore, I use Eq. $(S19)$ to estimate the Q_{as} trend implied by the SST trend observed over the warming hole. Values for Λ_v, ρ_a, q_1, q_2, σ, and c_p are given above. Based on examination of a global oceanic state estimate[10], I determine that $C_D = 0.0011$, $C_E = 0.0012$, and $C_H = 0.00061$ are reasonable values for the transfer coefficients over the subpolar gyre. Judging from this state estimate, I also assume reasonable distributions $\overline{\mathrm{SST}} \sim \mathcal{U}\left(6.5^{\circ}\mathrm{C}, 11.5^{\circ}\mathrm{C}\right)$ and $\big|\Delta\vec{U}\big| \sim \mathcal{U}\left(7.5\ \mathrm{m\ s^{-1}}, 10.5\ \mathrm{m\ s^{-1}}\right)$ for the subpolar gyre, where $\mathcal{U}\left(a, b\right)$ is the uniform distribution with minimum a and maximum b. Using these values, I estimate an approximate 95% confidence interval for the bracketed term (Γ) on the right-hand side of Eq. $(S19)$ of -27 ± 4.6 W m^{-2} $^{\circ}$C^{-1}. Multiplying this estimate of Γ times the

trend in SST over the subpolar warming hole quoted in the main text (-0.6 ± 0.4 °C century^{-1}) produces the surface heat flux trend of 16 ± 11 W m^{-2} century^{-1} given in the text.

S5 Converting a trend in surface heat flux over the subpolar warming hole to a temperature acceleration over the northern North Atlantic and Arctic Oceans

From basic conservation principles, if a surface heat flux Q_{as} acts on the ocean surface, and all of the heat gained is stored locally in the ocean, then the heat budget is,

$$\frac{\partial \Theta}{\partial t} = \frac{1}{\rho C_p H} Q_{as}, \tag{S20}$$

where Θ is the depth-averaged ocean (potential) temperature, ρ is seawater density, C_p is the specific heat of seawater (distinct from c_p, which is the specific heat of air in the past section), and H is the depth of the water column. Equivalently, taking a time derivative,

$$\frac{\partial^2 \Theta}{\partial t^2} = \frac{1}{\rho C_p H} \frac{\partial Q_{as}}{\partial t}. \tag{S21}$$

Hence, the right-hand side takes the form of a temperature acceleration. Setting $\partial Q_{as} / \partial t$ equal to 16 ± 11 W m^{-2} century^{-1} for the warming-hole region from the previous section, choosing typical round numbers of $\rho = 10^3$ kg m^{-3} and $C_p = 4 \times 10^3$ J kg^{-1} °C^{-1}, and selecting $H = 2.5 \times 10^3$ m as a representative depth for the northern North Atlantic Ocean, I obtain a range for the temperature acceleration $\partial^2 \Theta / \partial t^2$ of 5.0 ± 3.5 °C century^{-2}, which equates to a warming of 3.1 ± 2.1 °C over a 110-y period.

These acceleration and warming numbers apply to the subpolar warming-hole region, which has a surface area of about 5.3×10^{12} m^2 (Figure 7). In other words, these are the ocean temperature

changes that would be experienced in that region due to the surface heat flux in the absence of any lateral redistribution of heat by circulation and mixing. However, given the focus of this paper, it is instructive to consider whether the heat gain is stored not locally over the warming hole, but rather more broadly across the northern North Atlantic and Arctic Ocean, from $27°$N to Bering Strait. The motivation for choosing $27°$N as a boundary of the control volume is obvious, given the focus of the paper at that latitude. Bering Strait is typically chosen a convenient boundary to close the control volume in studies of Atlantic Ocean heat transport and storage, since transports of mass, heat, and freshwater through Bering Strait are relatively small and stable compared to transports in the Atlantic[11,12]. (Here I assume changes in transports through Bering Strait are totally negligible.) The surface area of this larger North Atlantic and Arctic control volume is 3.6×10^{13} m^2. Hence, multiplying the values above by the ratio of surface areas (5.3×10^{12} m^2/3.6×10^{13} m^2 $= 0.15$), the temperature acceleration and overall warming from earlier become 0.7 ± 0.5 °C century^{-2} and 0.4 ± 0.3 °C, respectively, if the heat flux over the warming hole was redistributed evenly over the northern North Atlantic and Arctic. These are the values quoted in the main text.

S6 Estimating trends in the deep branch of the overturning circulation and thermocline recirculation from trends in the Florida Current and subpolar sea-surface temperature

In the main text, I explain that the weakening of Florida Current transport and the surface heat flux trend resulting from the cooling of subpolar sea-surface temperatures over the warming hole must be physically consistent with two simple conservation principles: the sum of changes in all volume transports at $27°$N must equal zero (mass conservation), and the trend in ocean heat transport across

145 27°N must match to lowest order the trend in surface heat flux over the warming-hole region (heat
146 conservation). I express these requirements for mass and heat conservation respectively as,

$$\psi'_F + \psi'_D + \psi'_T = 0, \tag{S22}$$

147 and

$$-\psi'_F\overline{\Theta}_F - \psi'_D\overline{\Theta}_D - \psi'_T\overline{\Theta}_T = \frac{A}{C_p\rho}Q'_{as}. \tag{S23}$$

148 Here ψ_F, ψ_D, and ψ_T are the volume transports across 27°N (positive northward) by the Florida
149 Current, the deep branch of the overturning circulation, and thermocline recirculation, respectively,
150 and Θ_F, Θ_D, and Θ_T are corresponding representative ocean temperatures in Florida Straits, the
151 deep ocean ($\gtrsim 1000$ m), and the interior upper ocean ($\lesssim 1000$ m), respectively. As before, Q_{as} is
152 surface heat flux over the warming hole, ρ ocean density, and C_p specific heat capacity of seawater,
153 and here A is the surface area of the warming hole, so that AQ_{as} is the total surface heating of
154 the control volume. Primes are used here to indicate linear trends whereas overbars represent time
155 means. Note that in Eq. ($S23$), I ignore the time-tendency (local storage) term and heat transport by
156 currents acting on temperature anomalies. These assumptions are discussed in more detail below.

157 This linear system can be rearranged to solve for ψ'_D and ψ'_T in terms of ψ'_F and SST', *viz.*,

$$\psi'_D = \frac{\overline{\Theta}_F - \overline{\Theta}_T}{\overline{\Theta}_T - \overline{\Theta}_D}\psi'_F + \frac{1}{\overline{\Theta}_T - \overline{\Theta}_D}\frac{A\Gamma}{C_p\rho}\mathrm{SST}', \tag{S24}$$

158 and,

$$\psi'_T = -\frac{\overline{\Theta}_F - \overline{\Theta}_D}{\overline{\Theta}_T - \overline{\Theta}_D}\psi'_F - \frac{1}{\overline{\Theta}_T - \overline{\Theta}_D}\frac{A\Gamma}{C_p\rho}\mathrm{SST}', \tag{S25}$$

159 where Eq. ($S19$) was used to substitute $\Gamma\ \mathrm{SST}'$ for Q'_{as}. Based on examination of climatological

temperature from the World Ocean Atlas[13] along 27°N (Supplementary Figure 14), I assume that $\overline{\Theta}_F \sim \mathcal{U}\,(14.2°\mathrm{C}, 20.5°\mathrm{C})$, $\overline{\Theta}_T \sim \mathcal{U}\,(12.2°\mathrm{C}, 16.9°\mathrm{C})$, and $\overline{\Theta}_D \sim \mathcal{U}\,(1.4°\mathrm{C}, 3.6°\mathrm{C})$.

Given the $\overline{\Theta}_F$, $\overline{\Theta}_T$, and $\overline{\Theta}_D$ distributions, and values of $A = 5.3 \times 10^{12}$ m^2, $\rho = 10^3$ kg m^{-3}, $C_p = 4 \times 10^3$ J kg^{-1} °C^{-1}, and $\Gamma = -27 \pm 4.6$ W m^{-2} °C^{-1} from before, I can evaluate Eqs. $(S24)$, $(S25)$. Using the values of $\psi'_F = -1.7 \pm 3.7$ Sv century^{-1} and $\mathrm{SST}' = -0.6 \pm 0.4$ °C century^{-1} presented and discussed in the main text for 1909–2018, I find $\psi'_D = 1.4 \pm 1.8$ Sv century^{-1} and $\psi'_T = -0.3 \pm 4.9$ Sv century^{-1}, which are also quoted in the main text. More general estimates of ψ'_D and ψ'_T through time, and shown in Supplementary Figure 13, are generated by computing the posterior median and 95% credible interval of the mean rate of change in Florida Current transport from the Bayesian model and the linear trend in sea-surface temperature over the warming hole for all periods starting between 1909 and 1980 and ending in 2018, and then applying those values for the mean rates of change and linear trends to Eqs. $(S24)$, $(S25)$.

Some caveats should be discussed. The form of heat conservation $(S23)$ assumes that (1.) the time rate of change of temperature is negligible and (2.) heat transport due to currents acting on variable temperatures can be ignored.

Assumption (1.), that local ocean heat storage is negligible, was mentioned in the main text. I argued, using available estimates of ocean warming, that changes in local ocean heat content are too small to account for the surface heat flux implied by the longterm changes in sea-surface temperature, and therefore the surface heat flux must be mostly balanced by ocean heat transport. Note that, while it is reasonable on long, multidecadal to centennial timescales, assumption (1.)

does not apply on shorter, interannual and decadal periods, when changes in local ocean heat content become relatively more important. For example, over 1993–2015, decadal changes in subpolar North Atlantic Ocean heat content largely balanced ocean heat transport into the region due to changes in ocean circulation, and changes in surface heat flux were relatively small in comparison[14]. For this reason, Eqs. $(S24)$ and $(S25)$ are not evaluated for $\lesssim 40$-y periods.

Assumption (2.), that circulation changes operating on mean temperatures make the leading contributions to the heat transport, was not discussed in the text. This assumption has precedent in the observational literature and is supported by modeling results. For example, ocean heat transport estimates based on data from the RAPID array at 26°N have largely ignored nonseasonal changes in ocean temperature[15–17]. This assumption has been justified from strong correlation found between cable-based volume transports and directly measured temperature transports in Florida Straits[15,18], for example. Models generally support this result. Across a range of timescales, from seasonal to decadal, modeled ocean heat transports in the subtropical North Atlantic are strongly determined by changes in circulation acting on time-mean ocean temperatures, though time variations in temperature are not totally negligible[19–21].

These arguments make the case that assumptions (1.) and (2.) are reasonable and justifiable in the context of the back-of-the-envelope, order-of-magnitude estimates presented here. However, they are simplifications, as acknowledged above. Future studies should revisit these topics in more detail (e.g., relative importance of local ocean heat storage versus surface heat flux and ocean heat transport, or temperature versus velocity effects on ocean heat transports as a function of timescale)

based on models. However, such in-depth analyses are beyond the scope of the simple calculations presented here for purposes of interpreting posterior solutions from the Bayesian model, and so are left to more focused future studies.

References

1. Bos, M. S., S. D. P. Williams, I. B. Araújo, & L. Bastos. The effect of temporal correlated noise on the sea level rate and acceleration uncertainty, *Geophys. J. Int.*, **196**, 1423–1430.

2. Frankignoul, C., and K. Hasselmann. Stochastic climate models, part II: application to sea-surface temperature anomalies and thermocline variability, *Tellus*, **29**, 289–305 (1977).

3. Dangendorf, S., D. Rybski, C. Mudersbach, A. Müller, E. Kaufmann, E. Zorita, and J. Jensen. Evidence for long-term memory in sea level, *Geophys. Res. Lett.*, **41**, 5530–5537 (2014).

4. Fatichi, S., S. M. Barbosa, E. Caporali, and M. E. Silva. Deterministic versus stochastic trends: Detection and challenges, *J. Geophys. Res.*, **114**, D18121 (2009).

5. Ocaña, V., E. Zorita, and P. Heimbach. Stochastic secular trends in sea level rise, *J. Geophys. Res.-Oceans*, **121**, 2183–2202 (2016).

6. Theiler, J., S. Eubank, A. Longtin, B. Galdrikian, and J. D. Farmer. Testing for nonlinearity in time series: the method of surrogate data, *Physica D*, **58**, 77–94 (1992).

7. Meinen, C. S., W. E. Johns, B. I. Moat, R. H. Smith, E. M. Johns, D. Rayner, E. Frajka-Williams, R. F. Garcia, and S. L. Garzoli. Structure and variability of the Antilles Current at $26.5°$N, *J. Geophys. Res.-Oceans*, **124**, 3700–3723 (2019).

8. Emery, R. E., and W. J. Thomson. Data analysis methods in physical oceanography, 3rd Edition, Elsevier, 728 pp (2014).

9. Large, W. G., and S. G. Yeager. Diurnal to decadal global forcing for ocean and sea-ice models: the data sets and flux climatologies, *NCAR Technical Note*, NCAR/TN-460+STR, 112 pp.

10. Forget, G., et al. ECCO version 4: an integrated framework for non-linear inverse modeling and global ocean state estimation, *Geosci. Model Dev.*, **8**, 3071–3104 (2015).

11. Roach, A. T., K. Aagaard, C. H. Pease, S. A. Salo, T. Weingartner, V. Pavlov, and M. Kulakov. Direct measurements of transport and water properties through the Bering Strait, *J. Geophys. Res.*, **100**(C9), 18443–18457 (1995).

12. Woodgate, R. A. Increases in the Pacific inflow to the Arctic from 1990 to 2015, and insights into seasonal trends and driving mechanisms from year-round Bering Strait mooring data, *Prog. Oceanogr.*, **160**, 124–154 (2018).

13. Locarni, R. A., A. V. Mishonov, O. K. Baranova, T. P. Boyer, M. M. Zweng, H. E. Garcia, J. R. Reagan, D. Seidov, K. Weathers, C. R. Paver, and I. Smolyar. World Ocean Atlas 2018, Volume 1: Temperature, NOAA Atlas NESDIS 81, 52 pp (2018).

14. Piecuch, C. G., R. M. Ponte, C. M. Little, M. W. Buckley, and I. Fukumori. Mechanisms underlying recent decadal changes in subpolar North Atlantic Ocean heat content, *J. Geophys. Res.-Oceans*, **122**, 7181–7197 (2017).

15. Johns, W. E., M. O. Baringer, L. M. Beal, S. A. Cunningham, T. Kanzow, H. L. Bryden, J. J. M. Hirschi, J. Marotzke, C. S. Meinen, B. Shaw, and R. Curry. Continuous, array-based estimates of Atlantic Ocean heat transport at $26.5°$N, *J. Clim.*, **24**, 2429–2449 (2011).

16. Bryden, H. L., B. A. King, G. D. McCarthy, and E. L. McDonagh. Impact of a 30% reduction in Atlantic meridional overturning 2009–2010, *Ocean Sci.*, **10**, 683–691 (2014).

17. Bryden, H. L., W. E. Johns, B. A. King, G. McCarthy, E. L. McDonagh, B. I. Moat, and D. A. Smeed. Reduction in ocean heat transport at $26°$N since 2008 cools the eastern subpolar gyre of the North Atlantic Ocean, *J. Clim.*, **33**, 1677–1689 (2020).

18. Shoosmith, D. R., M. O. Baringer, and W. E. Johns. A continuous record of Florida Current temperature transport at $27°$N, *Geophys. Res. Lett.*, **32**, L23603 (2005).

19. Jayne, S. R., and J. Marotzke. The dynamics of ocean heat transport variability, *Rev. Geophys*, **39**, 385–411 (2001).

20. Dong, B., and R. T. Sutton. Variability in North Atlantic heat content and heat transport in a coupled ocean-atmosphere GCM, *Clim. Dynam.*, **19**, 485–497 (2002).

21. Piecuch, C. G., and R. M. Ponte. Importance of circulation changes to Atlantic heat storage rates on seasonal and interannual time scales, *J. Clim.*, **25**, 350–362 (2012).

253 22. Santamaría-Gómez, A., et al. Uncertainty of the 20th century sea-level rise due to vertical land
254 motion errors, *Earth Planet. Sci. Lett.*, **473**, 24–32 (2017).

255 23. Love, R., et al. The contribution of glacial isostatic adjustment to projections of sea-level
256 change along the Atlantic and Gulf coasts of North America, *Earth's Future*, **4**, 440–464 (2016).

257 24. Khan, N. S., et al. Drivers of Holocene sea-level change in the Caribbean, *Quaternary Sci.*
258 *Rev.*, **155**, 13–36 (2017).

259 25. Gelman, A, and D. B. Rubin. Inference from iterative simulation using multiple sequences,
260 *Stat. Sci.*, **7**, 457–472 (1992).

261 26. Birol, F., et al. Coastal applications from nadir altimetry: Example of the X-TRACK regional
262 products, *Adv. Space Res.*, **59**, 936–953 (2017).

263 27. Gebbie, G., and P. Huybers. The Little Ice Age and 20th-century deep Pacific cooling, *Science*,
264 **363**, 70–74 (2019).

Region	Site	Lon (°W)	Lat (°N)	Duration (years)	Rate (mm y^{-1})	Error (mm y^{-1})
Florida	AOML	80.1622	25.7347	6.37	0.27	0.74
Florida	CCV6	80.5455	28.4600	6.93	-2.95	0.74
Florida	MIA3	80.1602	25.7328	11.00	-0.32	0.80
Bahamas	EXU0	75.8734	23.5640	6.50	-1.85	0.54
Bahamas	NAS0	77.4623	25.0525	6.51	-2.18	2.42

Supplementary Table 1. Summary of GPS data from Version 6b of the dataset from Université de la Rochelle[22] used to estimate the difference in static sea-level rate across Florida Straits due to differential land motion quoted in the main text. Duration is the length of the data record. Error is twice the formal standard error provided with the dataset. Assuming errors are independent, the average rate across the two Bahamas sites is -2.02 ± 1.24 mm y^{-1} and the average rate across the three southeastern Florida sites is -1.00 ± 0.44 mm y^{-1}. The difference between the former and latter average values is -1.02 ± 1.32 mm y^{-1}, which represents the rate of differential vertical land motion across Florida Straits quoted in the main text. Multiplying by -1 to convert from the land-motion frame to the sea-level frame gives the value of 1.0 ± 1.3 mm y^{-1} quoted in the main text.

Region	Site	Reference	Lon (°W)	Lat (°N)	age (y BP)	sea level (m)
Florida	Florida Bay	Love et al.[23]	80.6	25	1260 ± 275	-1.34 ± 1.27
					890 ± 290	-0.83 ± 1.39
					400 ± 335	-1.00 ± 1.26
Florida	Bear Point	Love et al.[23]	80.3	27.4	1930 ± 350	-0.93 ± 1.45
					1380 ± 225	-1.13 ± 1.45
					1120 ± 215	-0.83 ± 1.45
Bahamas	Acklins Island	Khan et al.[24]	73.9	22.5	1048 ± 490	-1.64 ± 1.14
					698 ± 392	-1.23 ± 1.26
					398 ± 500	-1.08 ± 1.22
					242 ± 484	-0.97 ± 1.18

Supplementary Table 2. Proxy sea-level index points from southeastern Florida and the Bahamas used to estimate the difference in the rate of late-Holocene sea-level change across Florida Straits quoted in the main text. Latitudes and longitudes have been rounded to the nearest tenth of a degree. The "y BP" abbreviation stands for years before present, where present is 1950. The $\pm$ values are twice the standard errors on the age and sea-level values provided in the given references. Using ordinary least squares to fit a trend line to the index points at each site, and ignoring age and sea-level uncertainty, I compute trends of 0.36 ± 0.97, 0.05 ± 0.73 and 0.81 ± 0.22 mm y^{-1} at Florida Bay, Bear Point, and Acklins Island, respectively, where $\pm$ is twice the formal standard error furnished by ordinary least squares assuming independent data. The average of the two trends from southeastern Florida is thus 0.20 ± 0.61 mm y^{-1} and so the difference between the Bahamas and southeastern Florida is 0.6 ± 0.6, which is the value quoted in the main text.

No.	Location	Lon (°E)	Lat (°N)	Timespan (Completeness)	Coast
1	Cristóbal	−79.9167	9.35	1909–1979 (100%)	904
2	Puerto Limon	−83.0333	10	1949–1968 (90%)	906
3	Cartagena	−75.55	10.4	1949–1992 (68%)	902
4	Riohacha	−72.9167	11.55	1953–1969 (82%)	902
5	Fort-de-France II	−61.0632	14.6015	2006–2017 (100%)	912
6	Santo Tomás de Castilla	−88.6167	15.7	1965–1980 (75%)	916
7	Puerto Cortes	−87.95	15.8333	1948–1968 (100%)	908
8	Puerto Castilla	−86.0333	16.0167	1956–1968 (100%)	908
9	Lime Tree Bay	−64.7533	17.6933	1986–2015 (80%)	939
10	Port Royal	−76.85	17.9333	1955–1969 (100%)	932
11	Magueyes Island	−67.045	17.97	1955–2016 (90%)	938
12	Barahona	−71.0833	18.2	1955–1969 (67%)	936
13	Charlotte Amalie	−64.92	18.335	1976–2016 (61%)	939
14	San Juan	−66.115	18.4583	1963–2016 (81%)	938
15	Port-au-Prince	−72.35	18.5667	1950–1961 (100%)	934
16	South Sound	−81.3833	19.2667	1976–1993 (89%)	931
17	North Sound	−81.3167	19.3	1976–1996 (86%)	931
18	Puerto Plata	−70.7	19.8167	1950–1969 (70%)	936
19	Cabo Cruz	−77.7333	19.8333	1993–2017 (76%)	930
20	Guantanamo Bay	−75.1467	19.9067	1938–1971 (85%)	930
21	Gibara	−76.125	21.1083	1976–2016 (100%)	930
22	Nuevitas Punta Practico	−77.1095	21.5913	1992–2017 (35%)	930
23	Casilda II	−79.9917	21.7533	1984–2014 (48%)	930
24	Cabo de San Antonio	−84.9	21.9	1973–2017 (60%)	930
25	Isabela de Sagua	−80.0167	22.9333	2000–2016 (71%)	930
26	Key West	−81.8067	24.555	1913–2018 (97%)	940
27	Vaca Key	−81.105	24.7117	1990–2017 (79%)	940
28	Key Colony Beach	−81.0167	24.7183	1978–1994 (71%)	940
29	Virginia Key	−80.1617	25.73	1995–2017 (87%)	960
30	Miami Beach	−80.1317	25.7683	1932–1980 (92%)	960
31	Naples	−81.8067	26.1317	1966–2017 (83%)	940
32	West Palm Beach	−80.0333	26.6117	1974–2017 (36%)	960
33	Settlement Point	−78.9833	26.6833	2005–2015 (82%)	941
34	Settlement Point	−78.9967	26.71	1986–2000 (67%)	941
35	Trident Pier	−80.5917	28.415	1995–2017 (91%)	960
36	Daytona Beach Shores	−80.9633	29.1467	1967–1983 (71%)	960
37	Daytona Beach	−81	29.2333	1925–1969 (51%)	960
38	Jacksonville	−81.6167	30.35	1954–1967 (100%)	960
39	Mayport	−81.4317	30.3933	1929–1999 (99%)	960
40	Mayport	−81.4283	30.3983	2001–2017 (94%)	960
41	Fernandina Beach	−81.465	30.6717	1909–2018 (78%)	960
42	Fort Pulaski	−80.9017	32.0333	1935–2018 (95%)	960
43	Charleston	−79.925	32.7817	1922–2018 (100%)	960
44	Springmaid Pier	−78.9183	33.655	1978–2017 (60%)	960
45	Myrtle Beach	−78.885	33.6833	1958–1977 (55%)	960
46	Wilmington	−77.9533	34.2267	1936–2018 (95%)	960

Supplementary Table 3. Descriptions of tide-gauge sea-level records used in this study. "Completeness" is the percentage of timespan during which data are available. "Coast" number is the code used by the PSMSL to indicate the country and coastline of measurement.

Parameter	Description
$\boldsymbol{\eta}_0$	Sea-level initial condition
$\boldsymbol{\eta}_k$	Sea-level values at time t_k
$\overline{T}$	Transport time-mean value
T_k	Transport value at time t_k
$\boldsymbol{b}$	Spatial vector of regional trends in sea level
$\boldsymbol{a}$	Spatial vector of local trends in sea level
$\boldsymbol{\ell}$	Spatial vector of tide-gauge biases
r	AR(1) coefficient of sea level
μ	Mean value of regional trends in sea level
ν	Mean value of tide-gauge biases
ρ	Transport change per unit sea-level difference
α	Transport trend correction
π^2	Partial sill of regional trends in sea level
σ^2	Partial sill of sea-level innovations
δ^2	Tide-gauge error variance
τ^2	Spatial variance in observational biases
γ^2	Variance of local trends in sea level
ω^2	Variance of transport noise correction
ϕ	Inverse range of sea-level innovations
λ	Inverse range of regional trends in sea level

Supplementary Table 4. Descriptions of model processes and parameters.

Parameter	Prior Distribution	Hyperparameter Values
$\boldsymbol{\eta}_0$	$\mathcal{N}\left(\tilde{\eta}_{\boldsymbol{\eta}_0}\mathbf{1}, \tilde{\zeta}^2_{\boldsymbol{\eta}_0}\mathsf{I}\right)$	$\tilde{\eta}_{\boldsymbol{\eta}_0} = -0.2$ m , $\tilde{\zeta}^2_{\boldsymbol{\eta}_0} = (7.6 \times 10^{-2}\ \text{m})^2$
$\overline{T}$	$\mathcal{N}\left(\tilde{\eta}_{\overline{T}}, \tilde{\zeta}^2_{\overline{T}}\right)$	$\tilde{\eta}_{\overline{T}} = 32$ Sv , $\tilde{\zeta}^2_{\overline{T}} = (5.2\ \text{Sv})^2$
r	$\mathcal{U}\left(\tilde{u}_r, \tilde{v}^2_r\right)$	$\tilde{u}_r = 0.0$, $\tilde{v}^2_r = 1.0$
μ	$\mathcal{N}\left(\tilde{\eta}_\mu, \tilde{\zeta}^2_\mu\right)$	$\tilde{\eta}_\mu = 3.4 \times 10^{-3}\ \text{m y}^{-1}$, $\tilde{\zeta}^2_\mu = (2.7 \times 10^{-2}\ \text{m y}^{-1})^2$
ν	$\mathcal{N}\left(\tilde{\eta}_\nu, \tilde{\zeta}^2_\nu\right)$	$\tilde{\eta}_\nu = 7.0$ m , $\tilde{\zeta}^2_\nu = (0.6\ \text{m})^2$
ρ	$\mathcal{N}\left(\tilde{\eta}_\rho, \tilde{\zeta}^2_\rho\right)$	$\tilde{\eta}_\rho = 0.0\ \text{Sv m}^{-1}$, $\tilde{\zeta}^2_\rho = (190\ \text{Sv m}^{-1})^2$
α	$\mathcal{N}\left(\tilde{\eta}_\alpha, \tilde{\zeta}^2_\alpha\right)$	$\tilde{\eta}_\alpha = 0.0\ \text{Sv y}^{-1}$, $\tilde{\zeta}^2_\alpha = (0.3\ \text{Sv y}^{-1})^2$
π^2	$\mathcal{IG}\left(\tilde{\xi}_{\pi^2}, \tilde{\chi}^2_{\pi^2}\right)$	$\tilde{\xi}_{\pi^2} = 0.5$, $\tilde{\chi}^2_{\pi^2} = (1.9 \times 10^{-3}\ \text{m y}^{-1})^2$
σ^2	$\mathcal{IG}\left(\tilde{\xi}_{\sigma^2}, \tilde{\chi}^2_{\sigma^2}\right)$	$\tilde{\xi}_{\sigma^2} = 0.5$, $\tilde{\chi}^2_{\sigma^2} = (1.8 \times 10^{-2}\ \text{m})^2$
δ^2	$\mathcal{IG}\left(\tilde{\xi}_{\delta^2}, \tilde{\chi}^2_{\delta^2}\right)$	$\tilde{\xi}_{\delta^2} = 0.5$, $\tilde{\chi}^2_{\delta^2} = (7.1 \times 10^{-3}\ \text{m})^2$
τ^2	$\mathcal{IG}\left(\tilde{\xi}_{\tau^2}, \tilde{\chi}^2_{\tau^2}\right)$	$\tilde{\xi}_{\tau^2} = 0.5$, $\tilde{\chi}^2_{\tau^2} = (8.5 \times 10^{-2}\ \text{m})^2$
γ^2	$\mathcal{IG}\left(\tilde{\xi}_{\gamma^2}, \tilde{\chi}^2_{\gamma^2}\right)$	$\tilde{\xi}_{\gamma^2} = 0.5$, $\tilde{\chi}^2_{\gamma^2} = (7.1 \times 10^{-4}\ \text{m y}^{-1})^2$
ω^2	$\mathcal{IG}\left(\tilde{\xi}_{\omega^2}, \tilde{\chi}^2_{\omega^2}\right)$	$\tilde{\xi}_{\omega^2} = 0.5$, $\tilde{\chi}^2_{\omega^2} = (0.7\ \text{Sv})^2$
ϕ	$\mathcal{LN}\left(\tilde{\eta}_\phi, \tilde{\zeta}^2_\phi\right)$	$\tilde{\eta}_\phi = -7.0\ \text{log km}^{-1}$, $\tilde{\zeta}^2_\phi = (2.2\ \text{log km}^{-1})^2$
λ	$\mathcal{LN}\left(\tilde{\eta}_\lambda, \tilde{\zeta}^2_\lambda\right)$	$\tilde{\eta}_\lambda = -6.9\ \text{log km}^{-1}$, $\tilde{\zeta}^2_\lambda = (0.4\ \text{log km}^{-1})^2$

Supplementary Table 5. Prior distributions and hyperparameters. Hyperparameters are denoted with tildes to distinguish them from the other (uncertain) model parameters. The scripts are: $\mathcal{N}$ normal (or multivariate normal) distribution with mean $\tilde{\eta}$ and variance $\tilde{\zeta}^2$; $\mathcal{U}$ uniform distribution with lower bound $\tilde{u}$ and upper bound $\tilde{v}$; $\mathcal{IG}$ inverse-gamma distribution with shape ξ and scale χ; $\mathcal{LN}$ log-normal distribution with "mean" $\tilde{\eta}$ and "variance" $\tilde{\zeta}^2$.

Parameter	Units	$\hat{R}$	Median Value	95% CI	Width Ratio
$\overline{T}$	Sv	1.001	32.6317	$[31.2047,\ 34.0538]$	0.13837
α	Sv y^{-1}	1.0007	-0.013584	$[-0.054013,\ 0.0293]$	0.085205
r	—	1.0066	0.55246	$[0.47413,\ 0.63057]$	0.16441
μ ($\times 10^3$)	m y^{-1}	1.0007	2.6671	$[1.1105,\ 4.2612]$	0.028929
ν	m	0.99976	6.9845	$[6.9619,\ 7.0065]$	0.018982
ρ	Sv m^{-1}	0.9996	21.3501	$[10.4544,\ 32.4271]$	0.029465
π^2 ($\times 10^6$)	(m y^{-1})^2	1.0001	$(1.1673)^2$	$[(0.75971)^2,\ (1.9104)^2]$	0.00056614
σ^2 ($\times 10^6$)	m^2	1.0019	$(26.2588)^2$	$[(24.4292)^2,\ (28.3339)^2]$	0.00024641
δ^2 ($\times 10^6$)	m^2	0.99995	$(8.3539)^2$	$[(7.3177)^2,\ (9.4754)^2]$	0.00037666
τ^2 ($\times 10^6$)	m^2	0.99973	$(66.9832)^2$	$[(54.0808)^2,\ (85.3079)^2]$	0.00040194
γ^2 ($\times 10^6$)	(m y^{-1})^2	0.99995	$(0.6992)^2$	$[(0.40244)^2,\ (1.1171)^2]$	0.00090338
ω^2	Sv^2	0.9997	$(0.708)^2$	$[(0.4832)^2,\ (1.0033)^2]$	0.00058865
ϕ ($\times 10^3$)	km^{-1}	1.0025	0.68742	$[0.52277,\ 0.87158]$	0.0040641
λ ($\times 10^3$)	km^{-1}	1.0005	0.8429	$[0.43847,\ 1.6407]$	0.80349

Supplementary Table 6. Summary of posterior solutions for scalar parameters. The symbol $\hat{R}$ is a convergence monitor of Gelman and Rubin[25], such that values near 1 indicate convergence. Median Value and 95% credible interval (CI) are computed from the ensemble of posterior model solutions. The Width Ratio is defined as ratio of the width of the posterior 95% CI to the prior 95% CI width.

Parameter	Units	Truth	Median Value	95% CI
$\overline{T}$	Sv	32.8942	32.0523	$[30.9524,\ 33.0873]$
α	Sv y^{-1}	-0.018899	-0.023436	$[-0.059135,\ 0.0090315]$
r	—	0.54595	0.53247	$[0.46355,\ 0.60654]$
μ $(\times 10^3)$	m y^{-1}	2.977	3.1574	$[1.2438,\ 5.1438]$
ν	m	6.9876	6.9947	$[6.9739,\ 7.0165]$
ρ	Sv m^{-1}	23.5497	20.974	$[14.9067,\ 27.6991]$
π^2 $(\times 10^6)$	(m y^{-1})^2	$(1.078)^2$	$(1.4473)^2$	$[(0.94505)^2,\ (2.2444)^2]$
σ^2 $(\times 10^6)$	m^2	$(26.443)^2$	$(25.5557)^2$	$[(23.6732)^2,\ (27.7207)^2]$
δ^2 $(\times 10^6)$	m^2	$(8.7092)^2$	$(9.2437)^2$	$[(8.3297)^2,\ (10.1856)^2]$
τ^2 $(\times 10^6)$	m^2	$(67.1828)^2$	$(66.178)^2$	$[(54.0051)^2,\ (83.3185)^2]$
γ^2 $(\times 10^6)$	(m y^{-1})^2	$(0.64645)^2$	$(0.80521)^2$	$[(0.54918)^2,\ (1.1481)^2]$
ω^2	Sv^2	$(0.77083)^2$	$(0.34671)^2$	$[(0.23695)^2,\ (0.51894)^2]$
ϕ $(\times 10^3)$	km^{-1}	0.63572	0.60636	$[0.46714,\ 0.78344]$
λ $(\times 10^3)$	km^{-1}	0.79168	0.83584	$[0.44534,\ 1.6007]$

Supplementary Table 7. Summary of first synthetic data experiment. Comparison between the true (withheld) parameter values and the posterior model estimates.

Parameter	Units	True Value	Median Value	95% CI
ν	m	6.9876	6.9707	$[6.9506,\ 6.9918]$
$\delta^2\ (\times 10^6)$	m^2	$(8.7092)^2$	$(7.2674)^2$	$[(6.4296)^2,\ (8.1361)^2]$
$\tau^2\ (\times 10^6)$	m^2	$(67.1828)^2$	$(62.0712)^2$	$[(50.8668)^2,\ (78.9978)^2]$
$\gamma^2\ (\times 10^6)$	$(\mathsf{m\ y}^{-1})^2$	$(0.64645)^2$	$(0.80316)^2$	$[(0.55894)^2,\ (1.1291)^2]$

Supplementary Table 8. Summary of second synthetic data experiment. Comparison between the true (withheld) parameter values and the posterior model estimates.

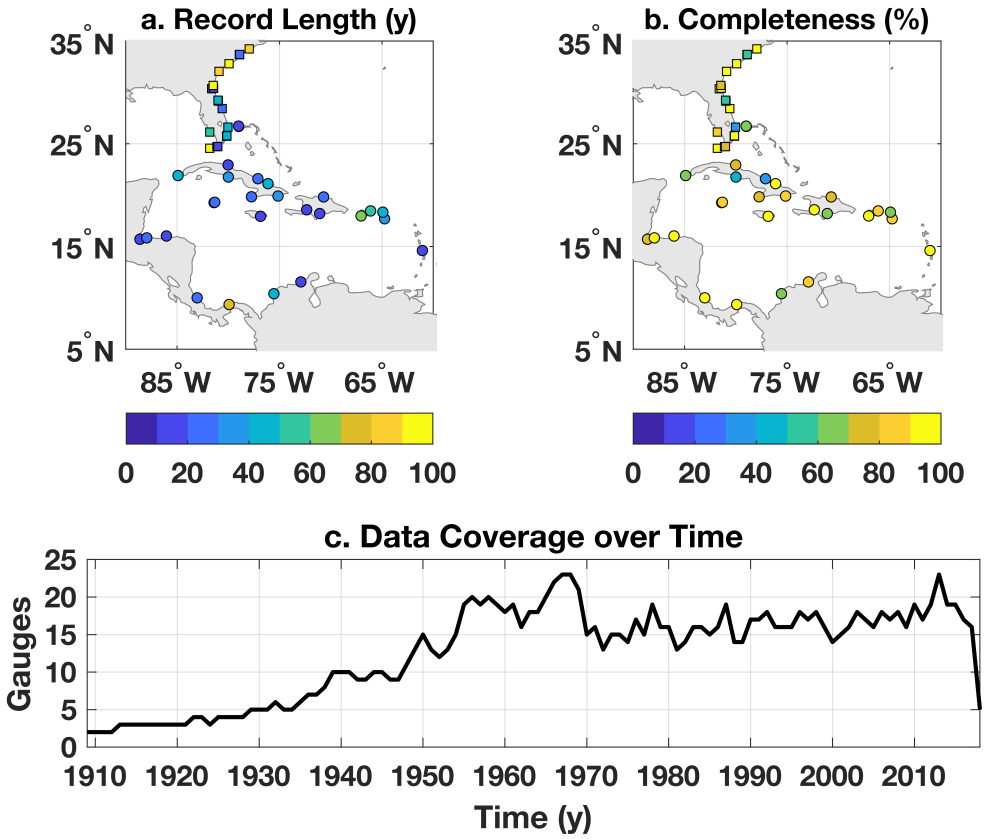

Supplementary Figure 1. Characteristics of tide-gauge data. **a,** Record length of tide-gauge records (number of y between the first and last measurements made during the study period). Yellower (bluer) colors indicate longer (shorter) records. **b,** Record completeness (percentage of y during the record length for which annual data are available). Yellower (bluer) colors indicate more (less) complete records. **c,** Number of tide gauges returning annual sea-level data during the course of the study period.

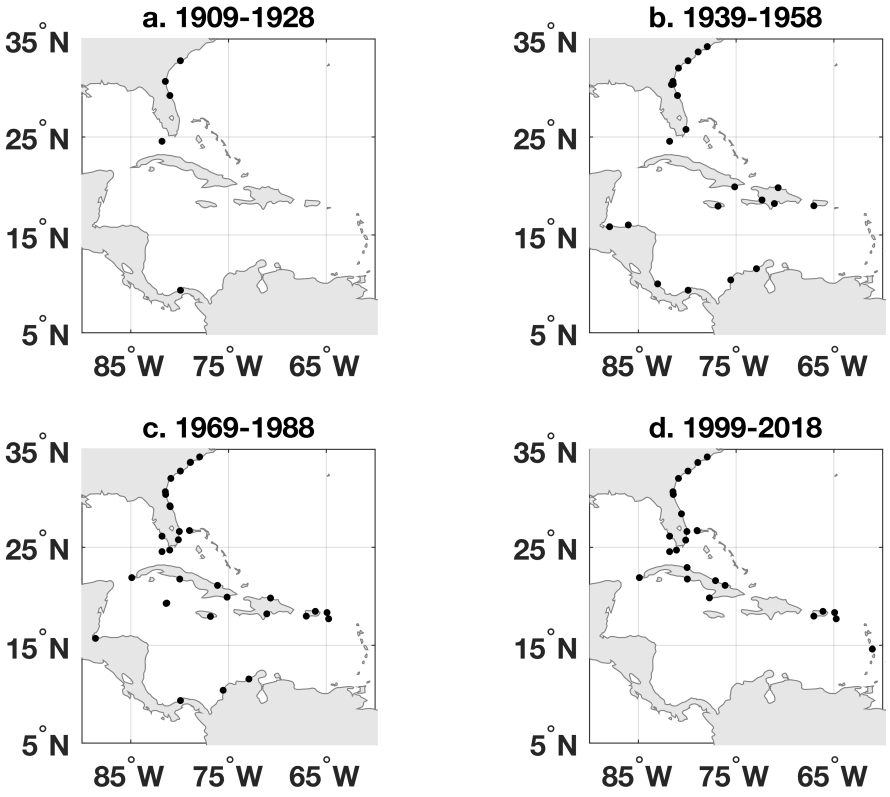

272

273 **Supplementary Figure 2. Availability of tide-gauge data over time.** Dots show tide gauges with

274 at least 1 y of data during **a,** 1909–1928, **b,** 1939–1958, **c,** 1969–1988, and **d,** 1999–1928.

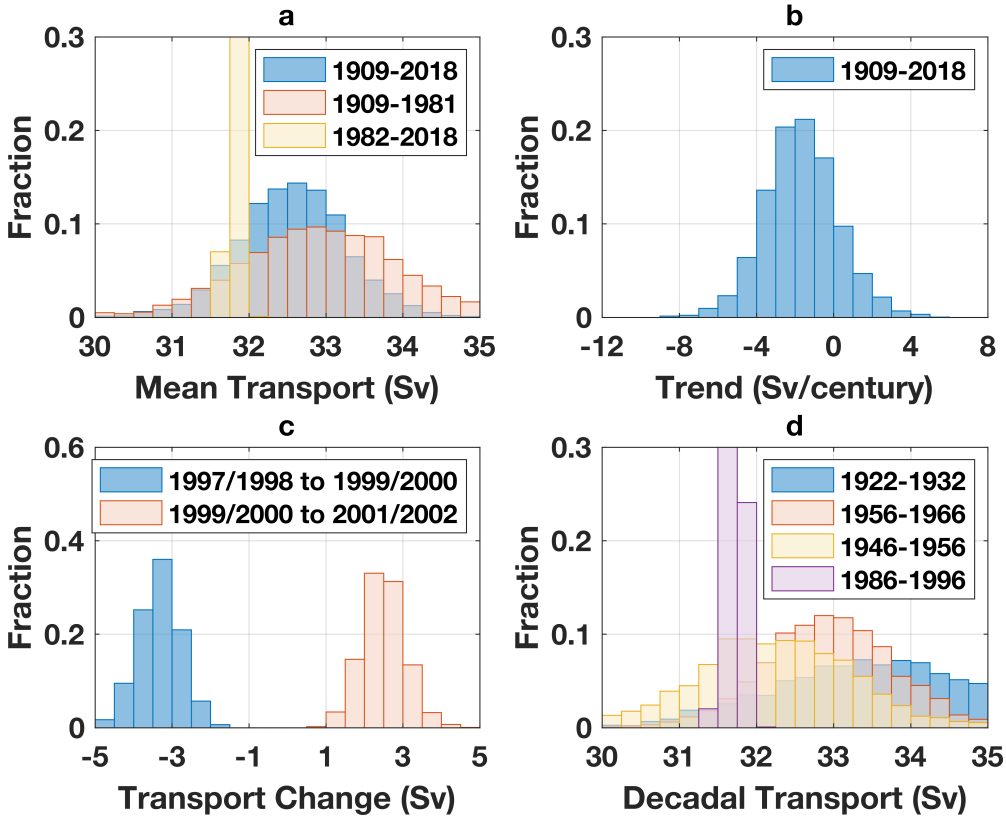

Supplementary Figure 3. Aspects of the posterior solution. **a,** Blue, orange, and yellow are histograms of transport $\boldsymbol{T}$ averaged during 1909–2018, 1909–1981, and 1982–2018, respectively (Sv). **b,** Histogram of the transport trend $\rho \boldsymbol{b}^{\mathsf{T}} \boldsymbol{\Delta} + \alpha$ over 1909–2018 (Sv century^{-1}). **c,** Blue (orange) is the histogram of the change in transport $\boldsymbol{T}$ between 1997/1998 to 1999/2000 (1999/2000 to 2001/2002) in units of Sv. **d,** Histograms of decadally averaged transport $\boldsymbol{T}$ in units of Sv: blue 1922–1932; orange 1956–1966; yellow 1946–1956; and purple 1986–1996. See Supplementary Table 4 for descriptions of symbols.

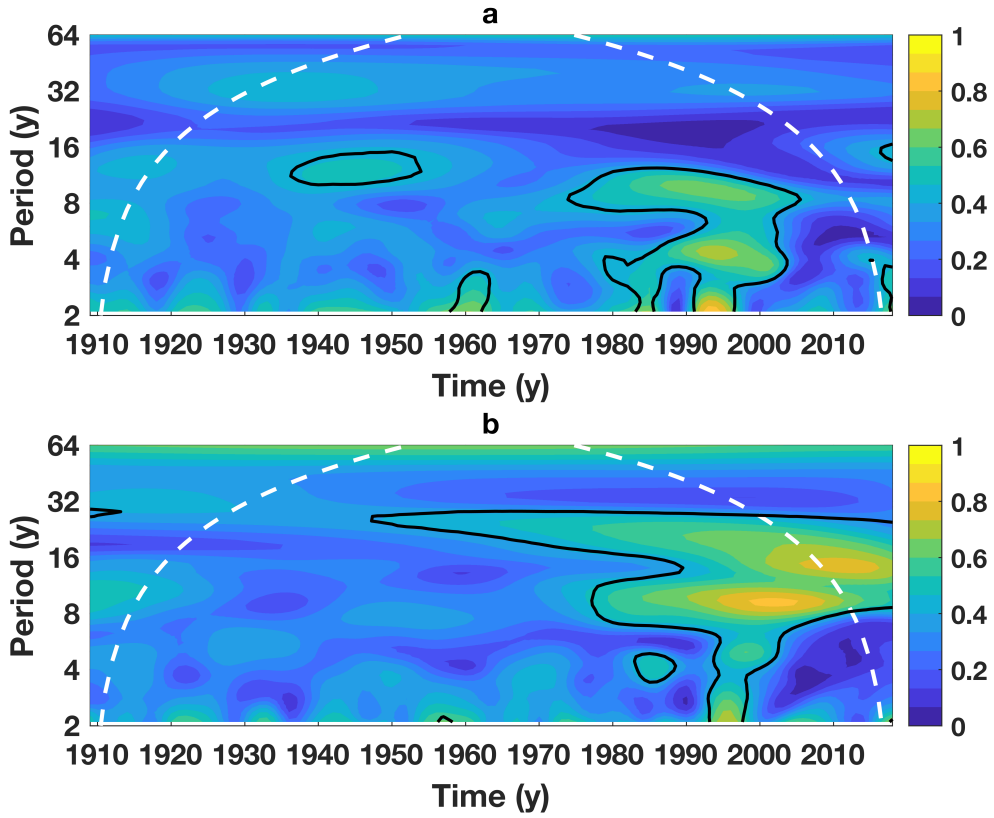

Supplementary Figure 4. Wavelet coherences. Magnitude squared wavelet coherence between Florida Current transport $\boldsymbol{T}$ and **a,** North Atlantic Oscillation and **b,** Atlantic Multidecadal Variability. Values are computed as follows. For each ensemble member, the wavelet coherence is computed between the transport solution and the climate index. For the same ensemble member, two random time series are generated, which have identical Fourier amplitudes to the transport solution and climate index, but randomized phases, and the wavelet coherence between the random time series is computed. Shaded colors represent medians of the set of wavelet-coherence values computed between all transport solutions and the given climate index. Black contouring indicates where 68% of wavelet coherences computed between transport solutions and the climate index exceed the value calculated between the pairs of random time series.

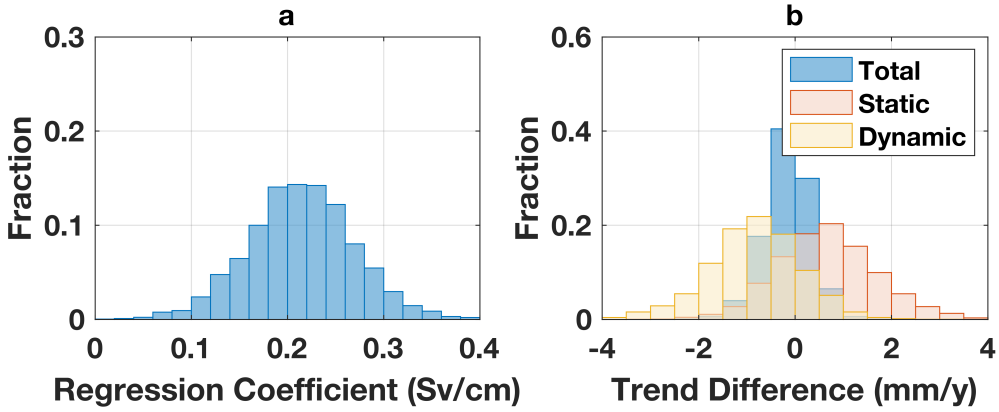

Supplementary Figure 5. More aspects of the posterior solution. **a,** Histogram of posterior solutions for the regression coefficient ρ (Sv cm^{-1}) between sea-level difference across Florida Straits and Florida Current transport. **b,** Histogram of posterior solutions for the total (blue), static (orange), and dynamic (yellow) trends in sea-level difference across Florida Straits, which are computed respectively as $\boldsymbol{b}^{\mathsf{T}}\boldsymbol{\Delta}$, $-\alpha/\rho$, and $\boldsymbol{b}^{\mathsf{T}}\boldsymbol{\Delta} + \alpha/\rho$ (mm y^{-1}) (see Methods). See Supplementary Table 4 for descriptions of symbols.

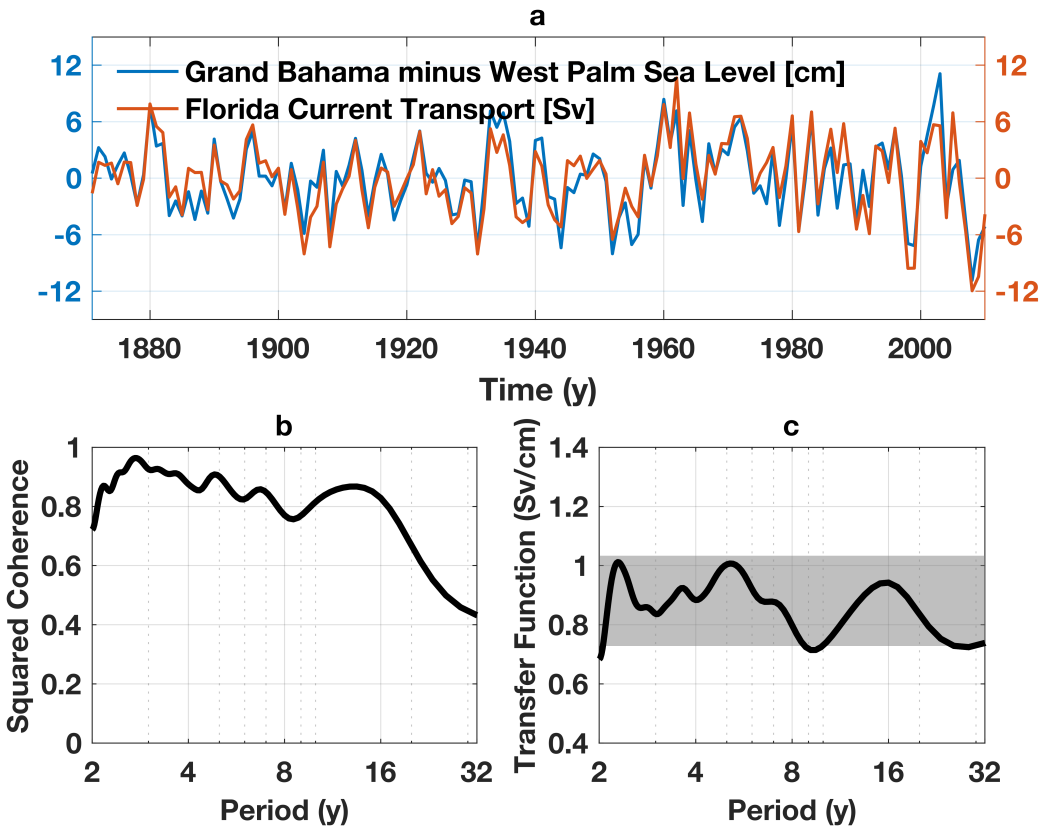

301

302 **Supplementary Figure 6. Frequency-domain analysis of sea level and transport from SODA.**

303 **a,** Blue (orange) is annual sea-level difference across Florida Straits (Florida Current transport)

304 during 1871–2010 from SODA. Both time series have been detrended. **b,** Black line is magnitude-

305 squared coherence between sea-level difference and transport for the first 128 y of the SODA

306 solution (1871–1998). All values are statistically significant at the 95% confidence level based on

307 comparison against synthetic time series. **c,** Black line is amplitude of the transfer function (using

308 sea-level difference as the input and transport as the output). Gray shading is the 95% posterior

309 credible interval on the transfer coefficient ρ from a synthetic data experiment based on SODA (see

310 Methods). Admittance and coherence calculations are based on Welch's method using a window

311 length of 32 and 50% overlap.

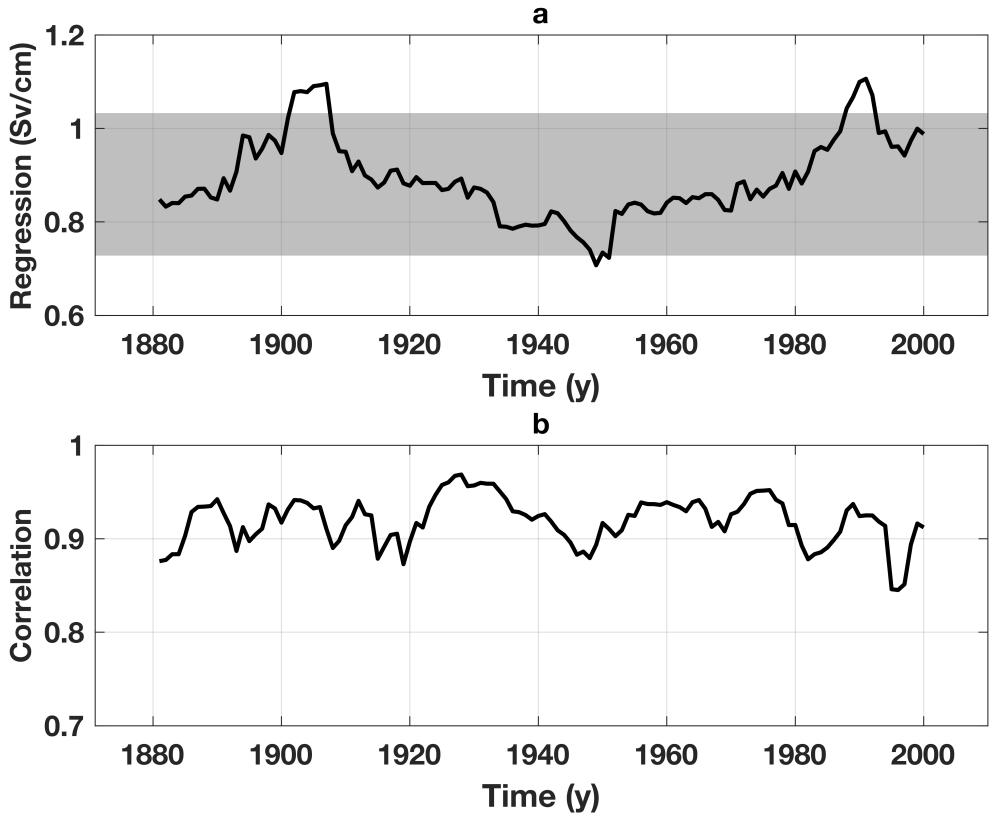

Supplementary Figure 7. Time-domain analysis of sea level and transport from SODA. a, Black line is regression coefficient between annual sea-level difference across Florida Straits and Florida Current transport for sliding 20-y windows during 1871–2010 from SODA. Gray shading is the 95% posterior credible interval on the regression coefficient ρ from a synthetic data experiment based on SODA (see Methods). **b,** Black line is correlation coefficient between annual sea-level difference across Florida Straits and Florida Current transport for sliding 20-y windows during 1871–2010 from SODA.

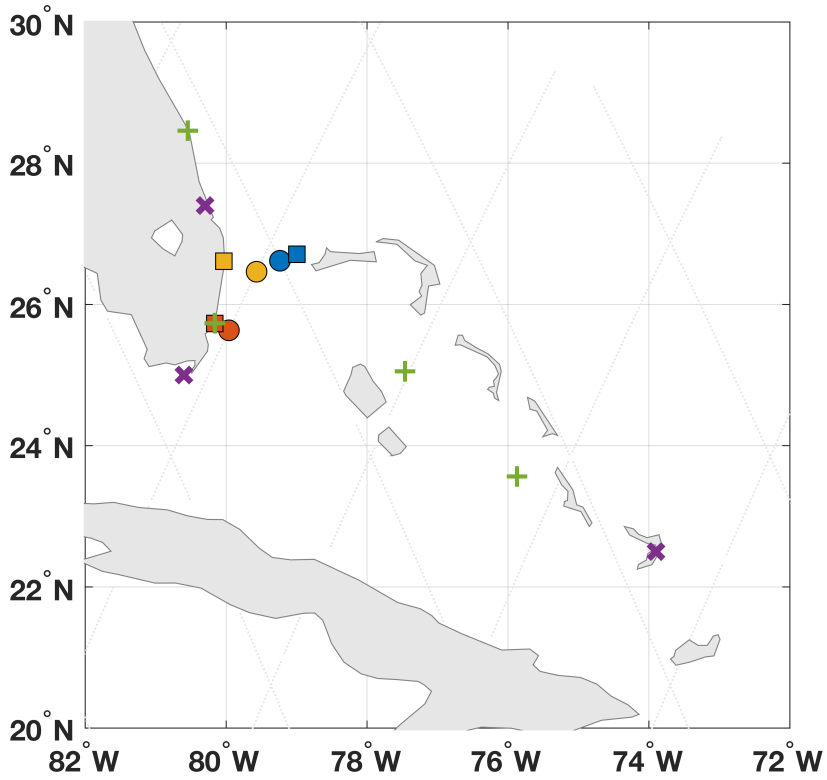

Supplementary Figure 8. Locations of ancillary observational assets. Shaded squares are tide-gauge locations (blue is Settlement Point; orange is Virginia Key; yellow is West Palm Beach). Shaded circles are the along-track satellite-altimeter data points that are nearest the corresponding tide gauge. Light gray criss-crossing marks ascending and descending altimeter tracks. Green + symbols denote locations of GPS stations (cf. Supplementary Table 1). Purple × symbols are the locations of proxy sea-level indicators (cf. Supplementary Table 2).

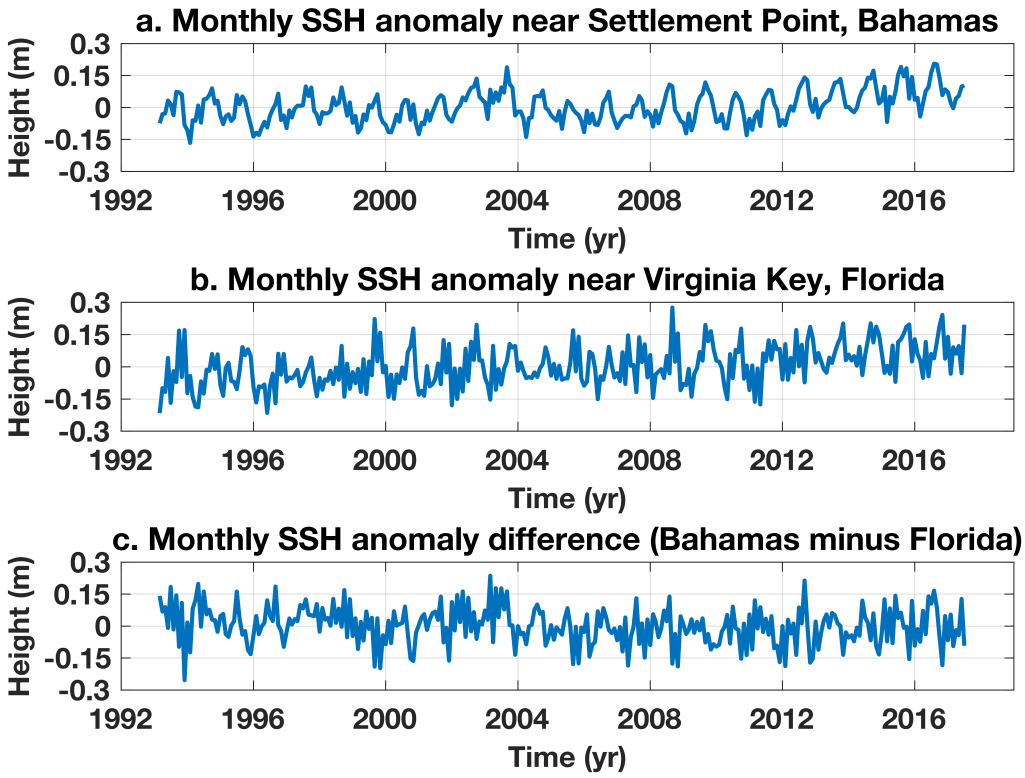

Supplementary Figure 9. Altimetric sea-surface height. Monthly time series of anomalous sea-surface height from satellite altimetry near **a,** Settlement Point, Bahamas, **b,** Virginia Key, Florida, and **c,** the difference between the two time series. Values shown here are calculated by bin averaging the raw 1-Hz data provided by Birol et al.[26] by year and month. See Supplementary Figure 8 for the locations of the time series.

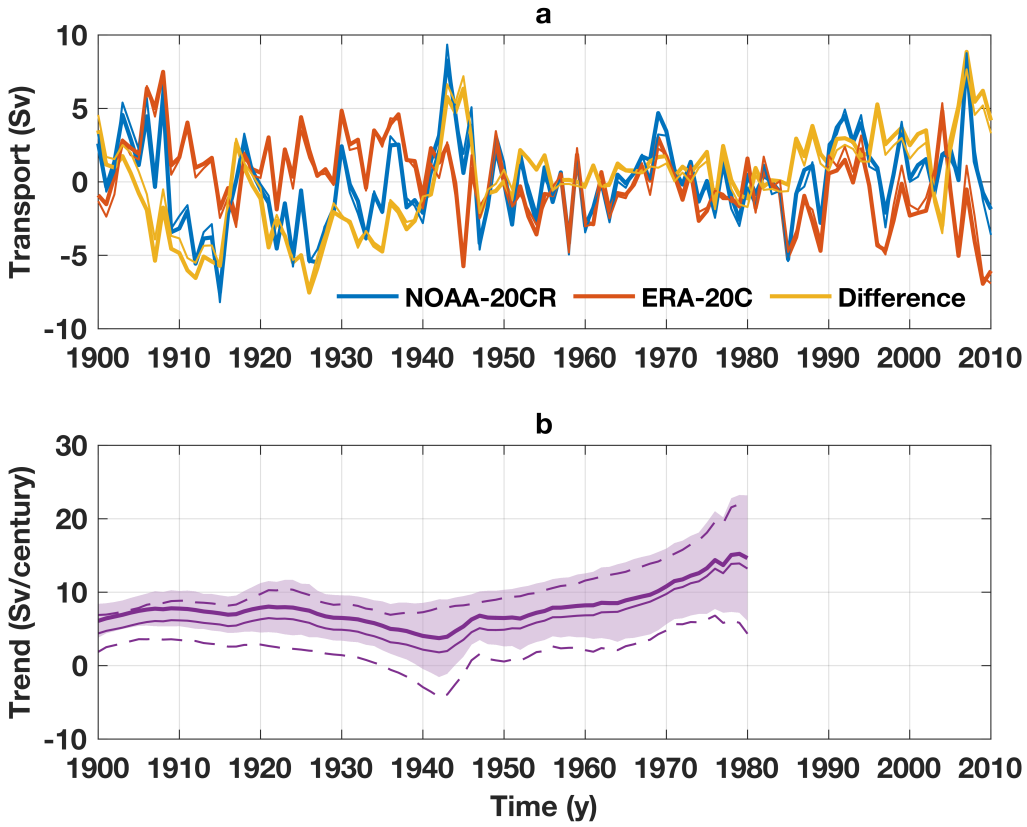

Supplementary Figure 10. Sverdrup and Ekman transport at 27°N from reanalyses. a, Thick blue and orange lines are annual geostrophic Sverdrup transport at 27°N computed from the NOAA-20CR and ERA-20C reanalyses, respectively, while the thick yellow line is the difference between the blue and orange lines. The thin lines are the same as the respective thick lines, only they include the ageostrophic Ekman transport in addition to the geostrophic Sverdrup transport. Time mean values have been removed from all time series. **b,** Thick line and light shading represent the best estimate and 95% confidence interval of the trend in geostrophic Sverdrup transport difference (thick yellow from a) for all periods starting between 1900 and 1980 and all ending in 2010. Thin line and dashed lines are the same, but include the Ekman transport difference in addition to the Sverdrup transport difference (thin yellow from a).

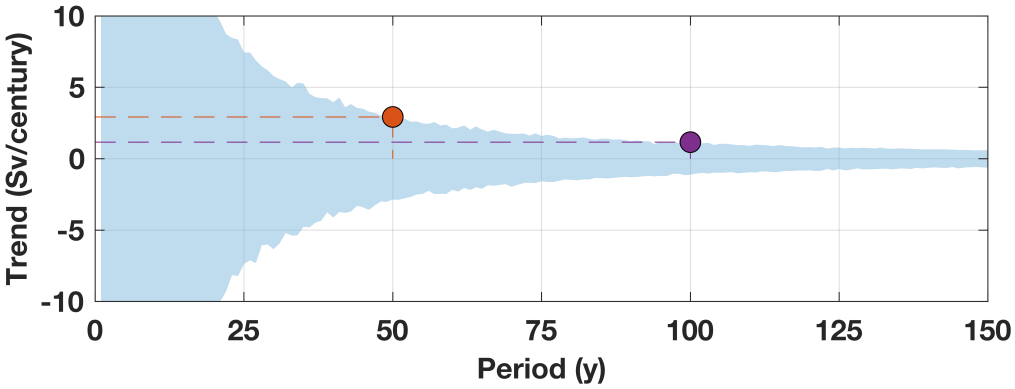

Supplementary Figure 11. Simulated trends in Antilles Current transport. Blue shading bounds the 95% confidence interval on stochastic trends in Antilles Current transport, based on simulations of a stationary red-noise process and an observed integral timescale of 19 days and variance of $(7.5\ \mathrm{Sv})^2$ for the Antilles Current. Orange and purple dots mark the trends for 50- and 100-y periods mentioned in the main text.

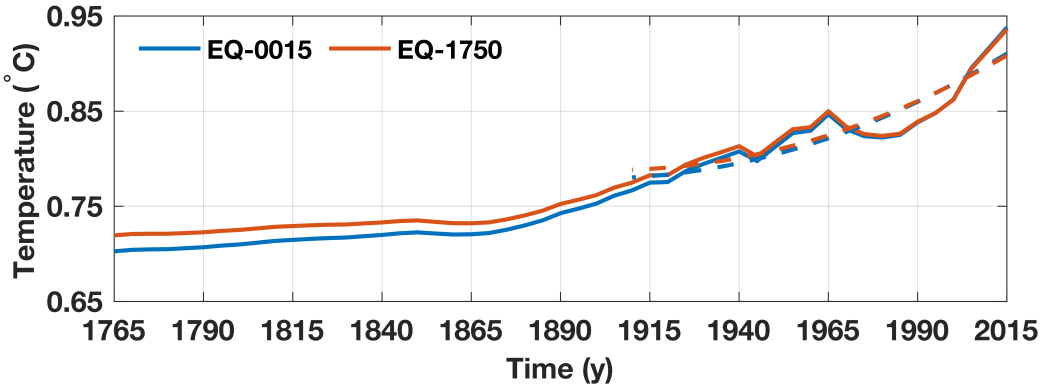

Supplementary Figure 12. Regional ocean warming over the past 250 y. Thick solid blue is the time series of ocean temperature averaged over the full-depth northern North Atlantic and Arctic Oceans, between 27°N and the Bering Strait, from the EQ-0015 empirical ocean circulation model experiment of Gebbie and Huybers[27], where the ocean is in equilibrium with surface conditions in the year 15 CE. Note that the time series of global-ocean mean temperature has been removed. Thick orange line is the same, but from the EQ-1750 experiment, where the ocean is in equilibrium in 1750 CE. Colored dashed lines are second-order polynomials fit to the respective solid lines for the period 1910–2015 CE; both dashed lines indicate an overall regional warming of ~ 0.1°C during that period.

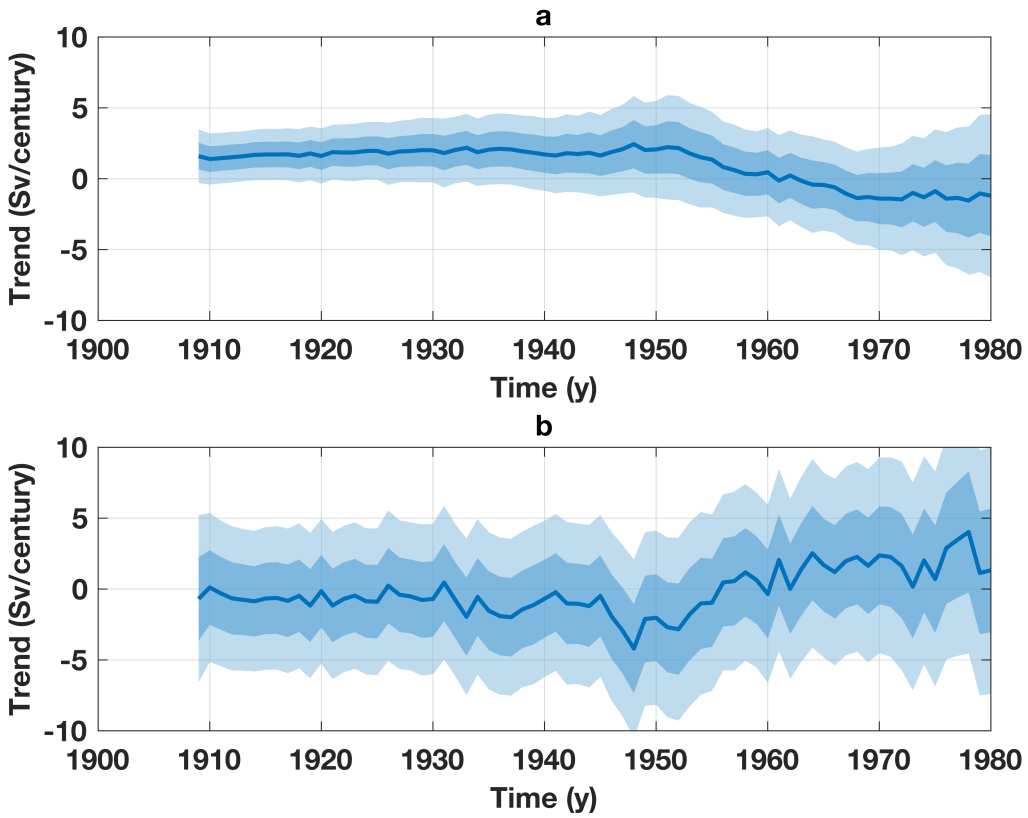

Supplementary Figure 13. Transport trends. a, Estimated trends in transport by the deep return flow of the overturning circulation for all periods starting between 1909 and 1980 and all ending in 2018 (positive northwards). Solid blue line is the best estimate while dark and light shading are respectively the estimated 68% and 95% confidence intervals. See Supplementary Information for more details on the estimates and their caveats. **b,** As in (a) but showing transport trends due to the thermocline recirculation.

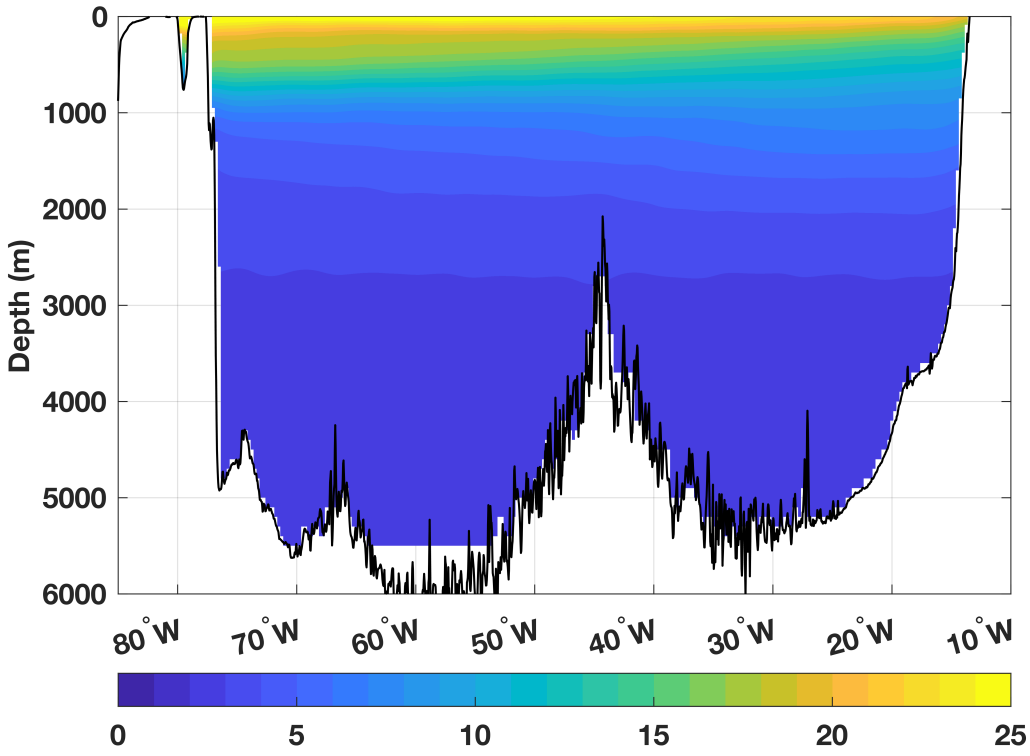

Supplementary Figure 14. Ocean temperatures. Time-mean (climatological) ocean potential temperature along 27°N in the Atlantic from the World Ocean Atlas 2018 as a function of depth and longitude (units °C).

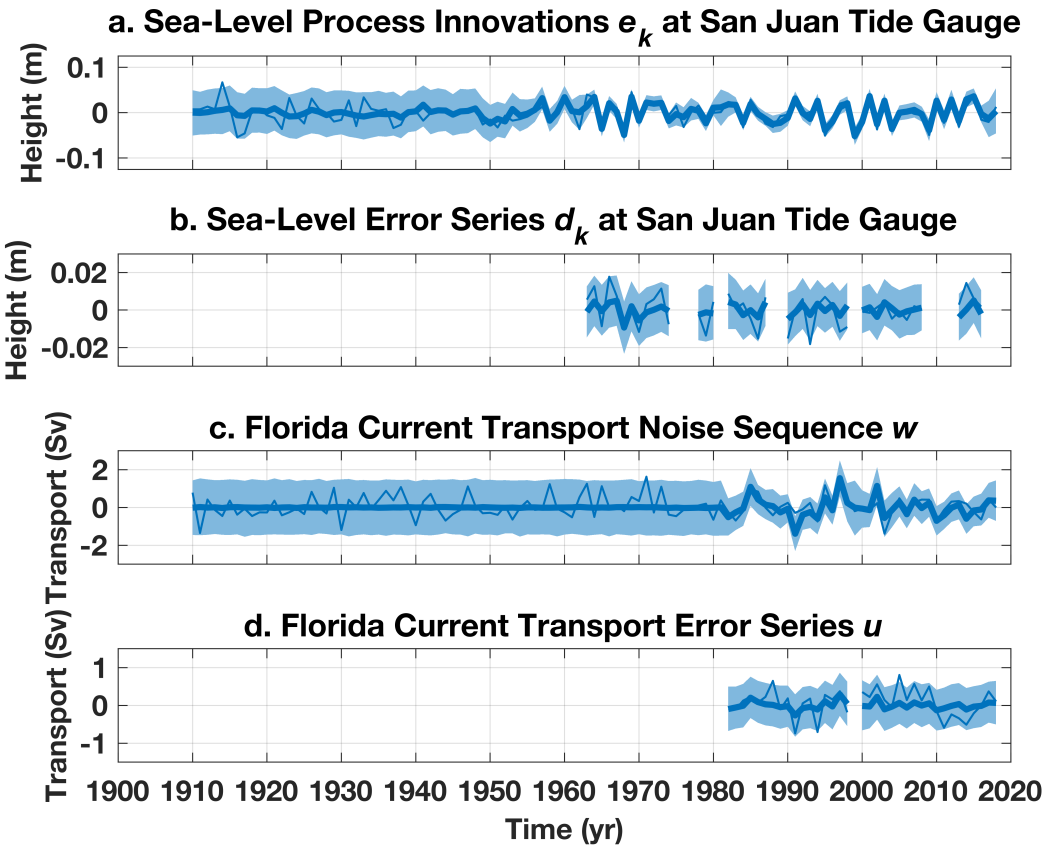

Supplementary Figure 15. Examples of residual time series. Posterior median (solid lines) and pointwise 95% credible intervals (light shading) of the sea-level **a,** process innovations $\boldsymbol{e}_k$ and **b,** data errors $\boldsymbol{d}_k$ at the San Juan (Puerto Rico) tide gauge. Posterior median (solid lines) and pointwise 95% credible intervals (light shading) of the transport **c,** noise sequence w_k and **d,** data errors u_k.

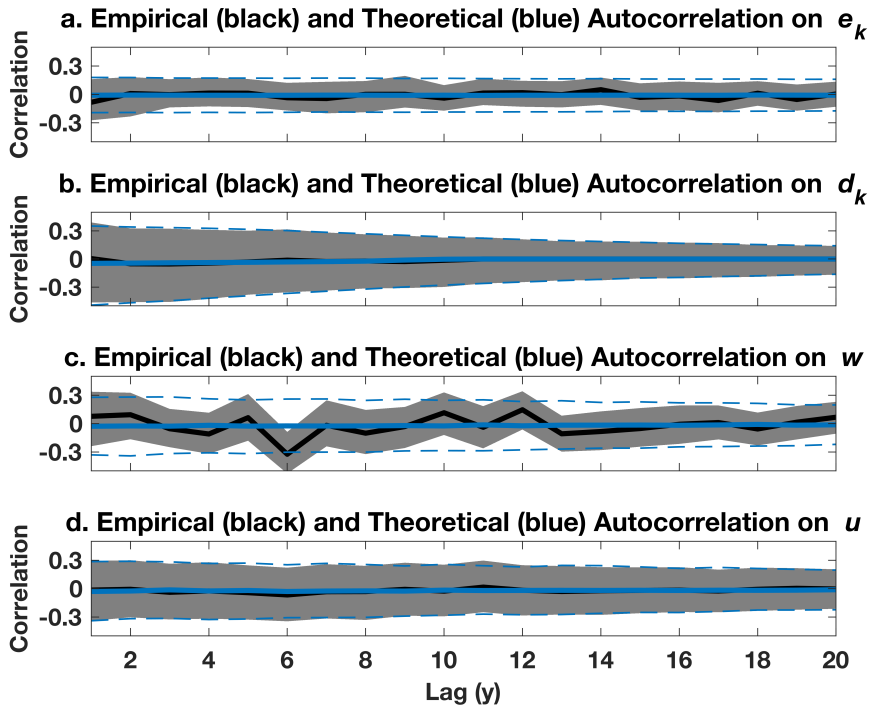

Supplementary Figure 16. Autocorrelation of the residuals. Posterior medians (solid black) and pointwise 95% credible intervals (gray shading) of the sample autocorrelation coefficient computed empirically from posterior solutions for the **a,** sea-level process innovations $\boldsymbol{e}_k$, **b,** sea-level data errors $\boldsymbol{d}_k$, **c,** transport noise sequence w_k, and **d,** transport data errors u_k. Solid and dashed blue lines are the mean $\pm$ twice the standard error on the autocorrelation coefficients expected theoretically from white noise with the same temporal degrees of freedom.

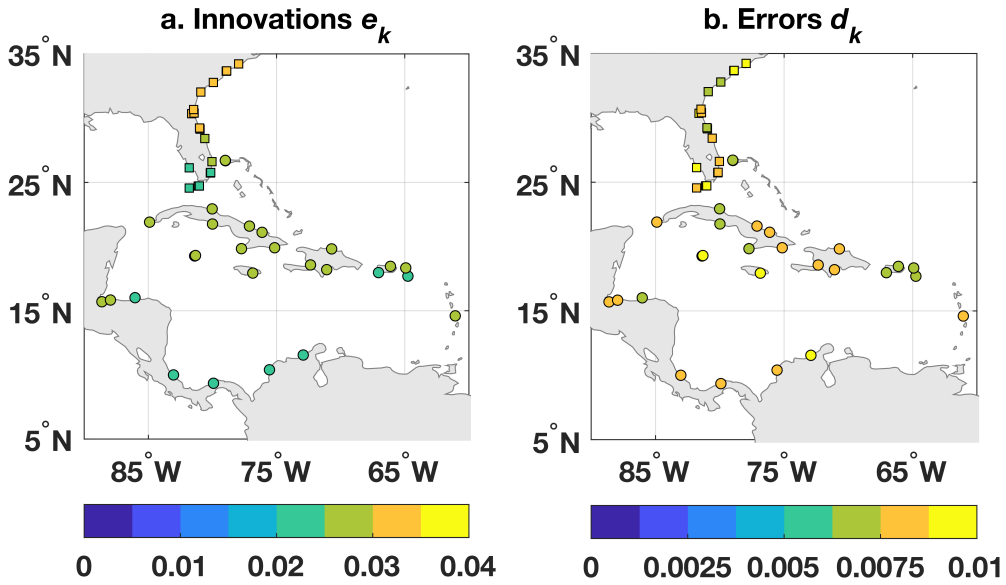

384

385 **Supplementary Figure 17. Amplitude of sea-level residual time series.** Median values of the

386 standard deviation (m) computed from posterior solutions for the sea-level **a,** process innovations

387 $\boldsymbol{e}_k$ and **b,** data errors $\boldsymbol{d}_k$ at all tide-gauge locations.

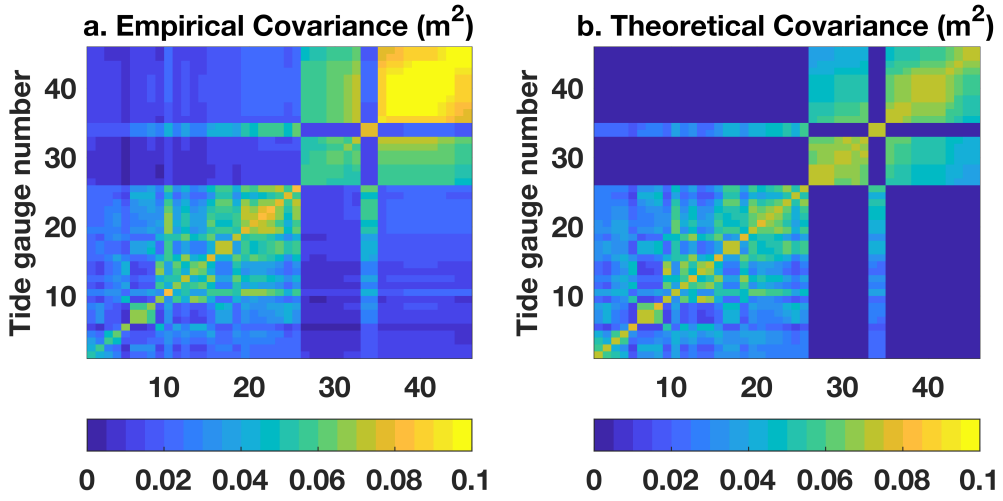

388

389 **Supplementary Figure 18. Spatial covariance of sea-level process innovations.** Covariance
390 (m^2) between all pairs of sea-level process innovations $\boldsymbol{e}_k$ computed **a,** empirically based on poste-
391 rior solutions for $\boldsymbol{e}_k$ and **b,** theoretically using posterior solutions for σ^2 (Supplementary Table 6)
392 and the assumed covariance structure Eq. (2). The "tide-gauge number" along x- and y-axes refer
393 to the values given in the leftmost column in Supplementary Table 3.

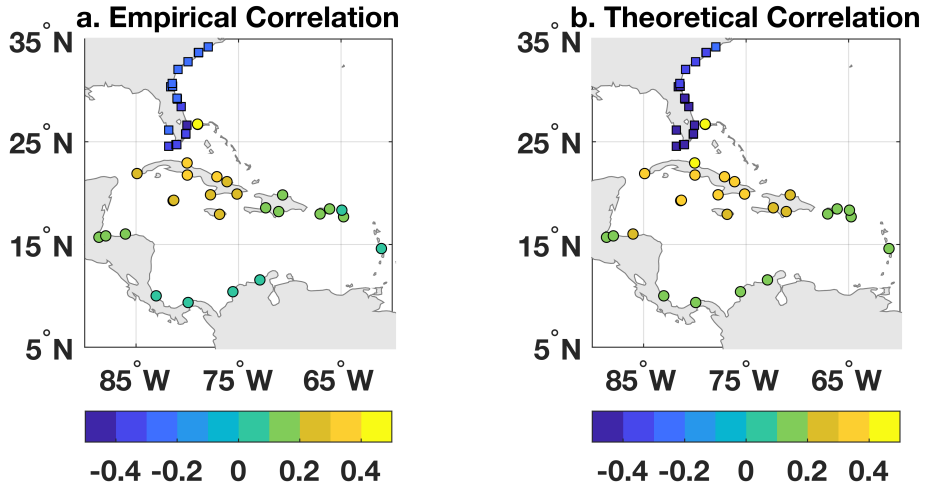

394

395 **Supplementary Figure 19. Correlation between sea level and Florida Current transport. a,**
396 Shading is the median value of the Pearson correlation coefficient computed empirically between
397 posterior Bayesian model solutions for the Florida Current transport and sea level at every location
398 after linear trends are removed. **b,** Shading is the median theoretical value of the Pearson corre-
399 lation coefficient based on the Bayesian model process-level equations and posterior solutions for
400 the model parameters (Supplementary Table 6).

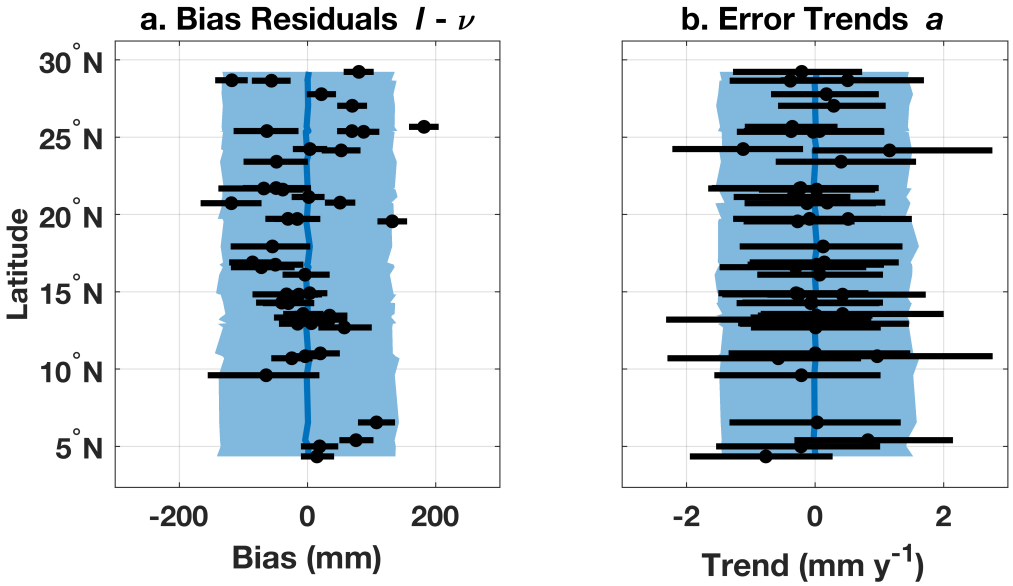

401

402 **Supplementary Figure 20. Spatial structure of tide-gauge residual vectors.** Posterior medians
403 (black dots) and pointwise 95% credible intervals (black lines) for the tide-gauge **a,** data-bias
404 anomalies $\boldsymbol{\ell} - \nu\mathbf{1}$ (m) and **b,** error trends $\boldsymbol{\alpha}$ (mm y^{-1}). Also shown are the means (solid blue) and
405 95% credible intervals on these fields estimated from their assumed functional forms and posterior
406 solutions for the respective variance parameters τ^2 and γ^2 (Supplementary Table 6).

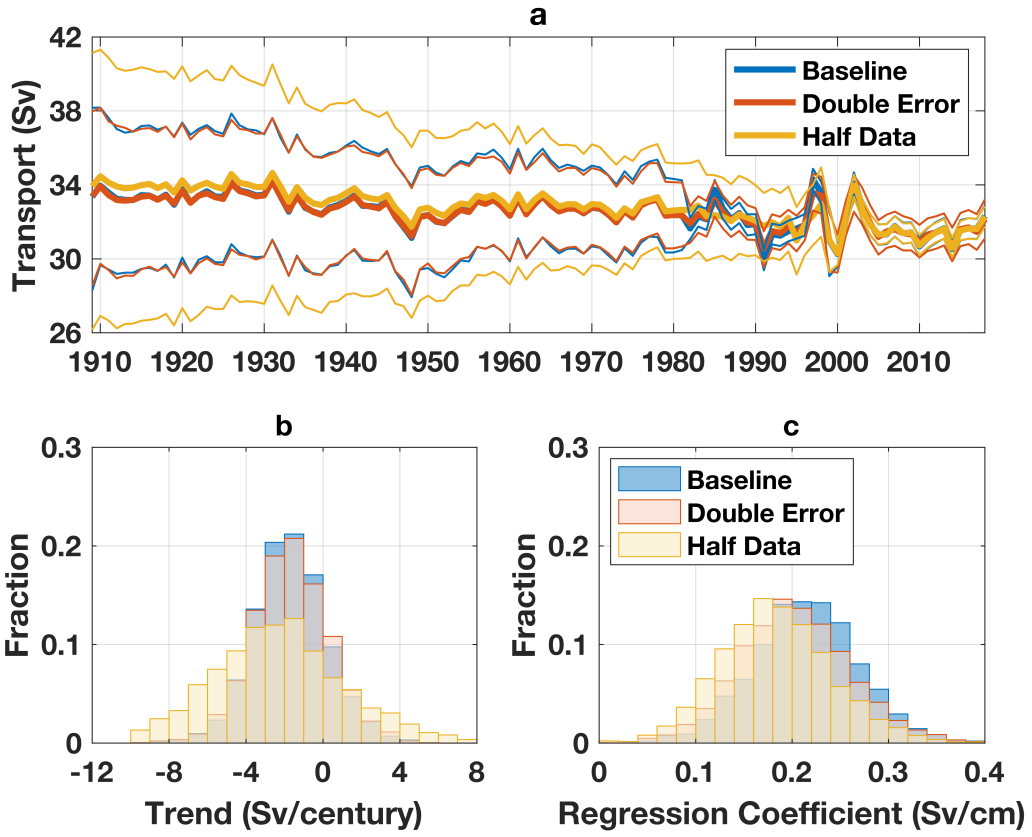

Supplementary Figure 21. Sensitivity of Bayesian model solution to input transport data. Summary of results from sensitivity experiments using different forms of the Florida Cable transport data. **a,** Time series of transport (thick lines are posterior medians; thin lines bound the posterior 95% pointwise credible intervals). **b,** Histograms of the 110-y trend (1909–2018) in Florida Current transport. **c,** Regression coefficient between sea-level difference across Florida Straits and Florida Current transport. Blue values are from the "baseline" model experiment discussed in the main text. Orange values are based on an "double error" experiment wherein the standard errors on the transport data during 1982–2018 are doubled. Yellow values are based on a "half data" experiment where the algorithm is only given the cable data during the period 2000–2018 and the 1982–1998 values are withheld.

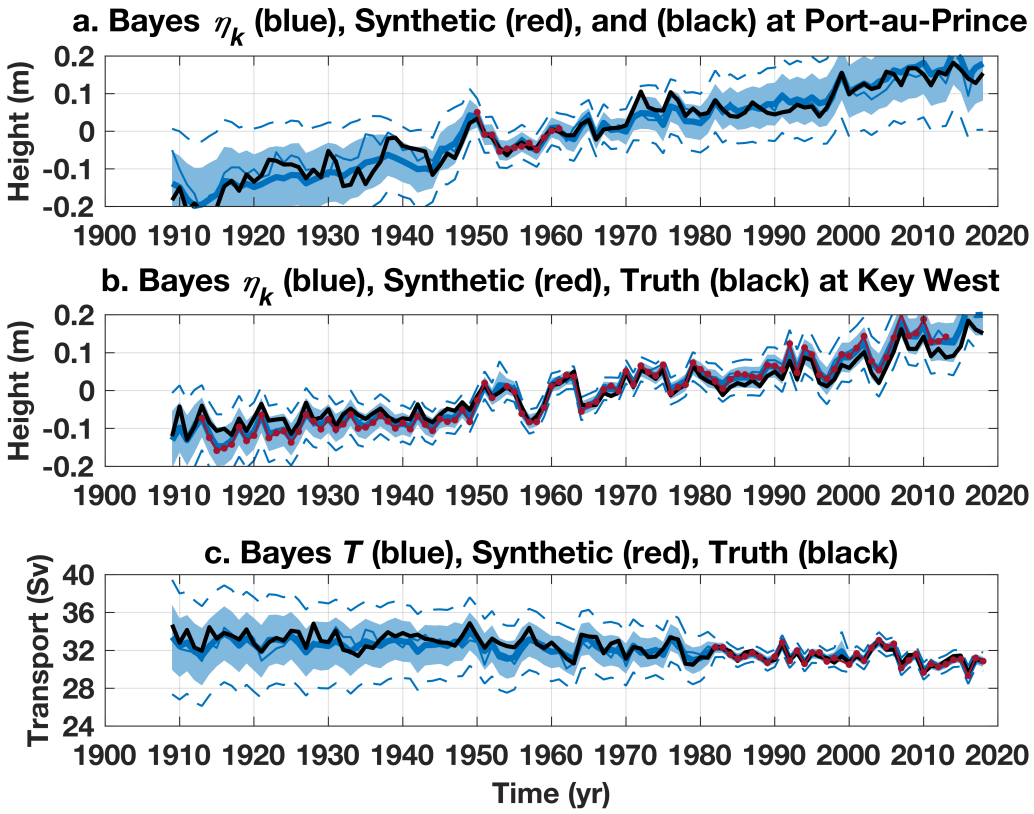

418

419 **Supplementary Figure 22. Examples of results from first synthetic data experiment.** Synthetic
420 observations (red), true values (black), and posterior medians (thick blue), pointwise (blue shading)
421 and pathwise (dashed blue) 95% credible intervals, and an arbitrary ensemble member (thin blue)
422 of **a,** sea level at the Port-au-Prince (Haiti) tide gauge, **a,** sea level at the Key West (USA) tide
423 gauge, and **c,** Florida Current transport.

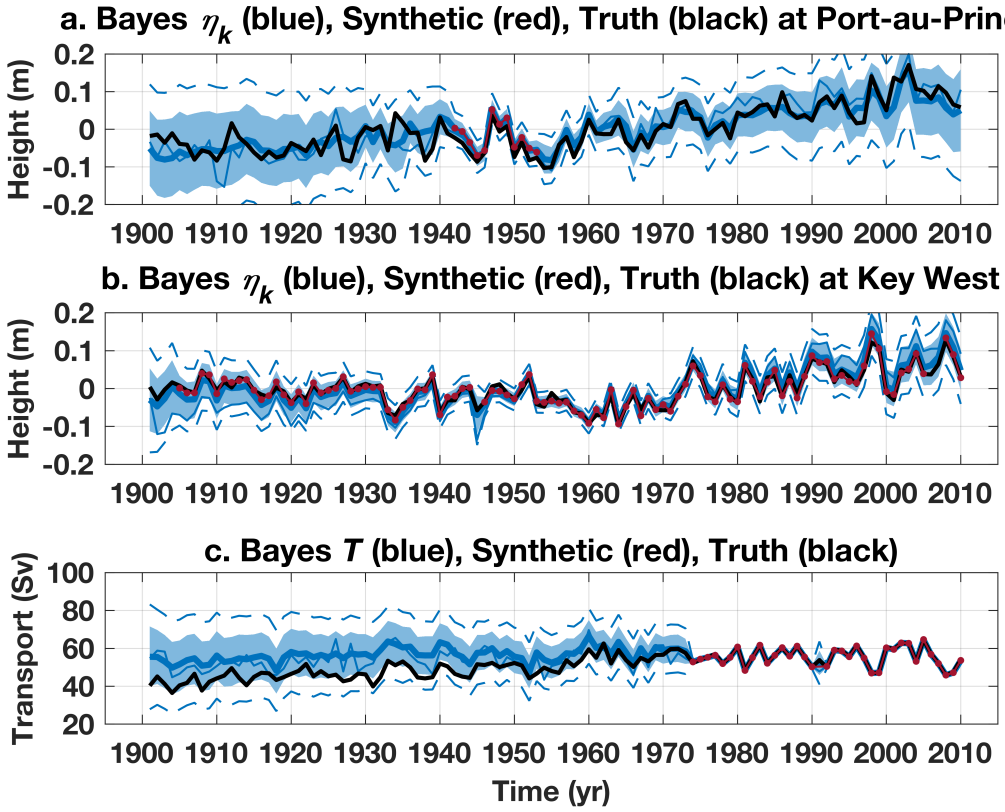

Supplementary Figure 23. Examples of results from second synthetic data experiment. Synthetic observations (red), true values (black), and posterior medians (thick blue), pointwise (blue shading) and pathwise (dashed blue) 95% credible intervals, and an arbitrary ensemble member (thin blue) of **a,** sea level at the Port-au-Prince (Haiti) tide gauge, **a,** sea level at the Key West (USA) tide gauge, and **c,** Florida Current transport.